UNIVERSITY OF BELGRADE
FACULTY OF TECHNOLOGY AND METALLURGY

Hana Ibrahim Elswie

SYNTHESIS AND CHARACTERIZATION OF OPTICAL POLYMER COMPOSITES BASED ON SINGLE CRYSTALS

Doctoral Dissertation

Belgrade, 2017.

UNIVERZITET U BEOGRADU
TEHNOLOŠKO-METALURŠKI FAKULTET

Hana Ibrahim Elswie

SINTEZA I KARAKTERIZACIJA OPTIČKI AKTIVNIH KOMPOZITA SA POLIMERNOM MATRICOM NA BAZI MONOKRISTALA

Doktorska Disertacija

Beograd, 2017.

Supervisors

Dr Vesna Radojević, full professor, University of Belgrade
Faculty of Technology and Metallurgy

Dr Zorica Lazarević, Associate Research Professor, University of Belgrade,
Institute of Physics

Member of Committee

Dr Petar Uskoković, full professor, University of Belgrade
Faculty of Technology and Metallurgy

Dr Radmila Jančić-Hajneman, full professor, University of Belgrade
Faculty of Technology and Metallurgy

Dr Dušica Stojanović, Associate Research Professor, University of Belgrade
Faculty of Technology and Metallurgy

Date:_____

ACKNOWLEDGEMENTS

SINTEZA I KARAKTERIZACIJA POLIMERNIH KOMPOZITA NA BAZI MONOKRISTALA POLUPROVODNIČKIH MATERIJALA

Rezime

Kompoziti sa polimernom matricom na bazi monokristala imaju veliki potencijal u oblasti optičkih komunikacionih sistema gde su aktivni mikro do nano kristali dispergovani u optički transparentnu matricu. Predmet ove doktorske disertacije obuhvata istraživanja u oblasti funkcionalnih optoelektronskih kompozitnih materijala s polimernom matricom za primenu u elektronskim tehnologijama kao i u oblasti komunikacijskih i navigacionih tehnika i mogućnosti razvijanja integralne optike i fotonike. U toku izrade ove disertacije izvedena je sinteza polimernih optoelektronskih kompozitnih materijala kontrolisanih optičkih svojstava. Dobijanje visoko transparentnih kompozita moguće je s jedne strane korišćenjem neorganskih punilaca dimenzija čestica manjih od talasne dužine elektromagnetnog zračenja, da ne bi došlo do rasejavanja. Drugi način je ugradnja materijala sa sličnim vrednostima indeksa refrakcije. U okviru ove disertacije izbor materijala pao je na poli (metil-metakrilat) sa indeksom refrakcije $n_{600}= 1.49$ i kalcijum-fluorid sa $n_{600}= 1.43$.

Istraživanja su išla u dva pravca: a) sinteza monokristalnog CaF_2 kao funkcionalnog nosioca u kompozitu i ugradnja u polimernu matricu; b) sinteza i karakterizacija kompozita sa polimernom matricom ugradnjom kvantnih tačaka CdSe. Na ovako organizovan način istraživanja može se pratiti i uticaj organizacije i dimenzija kristala na optička i mehanička svojstva dobijenog kompozita.

Modifikovanom metodom vertikalni Bridžman u vakumu dobijen je visoko kvalitetni monokristal CaF_2. Dobijeni kristal je ispitivan metodam Raman i IC spektroskopijom. Kristalna struktura je potvrđena rendgensko strukturnom analizom. U skladu sa teorijom grupa primećen je jedan Raman i dva infracrvena optička moda. Niska fotoluminiscencija svedoči o tome da je koncentracija defekata kiseonika u CaF_2 mala. Sva obavljena istraživanja pokazuju da dobijeni monokristal CaF_2 ima dobar optički kvalitet. Nakon

mlevenja čestice monokristala su ugrađene u polimernu matricu poli (metil-metakrilata). Ugradnjom monokristalnog CaF_2 dobijen je kompozit sa očuvanim optičkim svojstvima monokristala, dok su termička i mehanička svojstva poboljšana.

Kvantne tačke (*quantum dots*-QD) predstavljaju poluprovodne monokristalne nanostrukture, čiji su nosioci naelektirisanja prostorno ograničeni u sve tri dimenzije. Materijal od koga su tačke izrađene definiše njihove karakteristične energijske vrednosti, međutim tačne vrednosti energijskog procepa su određene veličinom tačke. Posledica ovoga je činjenica da kvantne tačke izrađene od istog materijala, ali različitih veličina emituju zračenje različitih talasnih dužina. U okviru ovog rada izvedeno je ispitivanje uslova dobijanja tankog filma od poli(metil metakrilat)-a dopiranog kvantnim tačkama CdSe metodom livenja iz rastvora. Termička svojstva kompozita ispitana su metodom DSC. Optička svojstva ispitivana su analizom emisionog spektra pikosekundnim mernim sistemom za merenje vremena života luminescencije. Mehanička svojstva su ispitana primenom metode nanoindentacije. Rezultati DSC Apokazuju da je za kompozitni film PMMA dopiranog s QD dobijena je nešto niža T_g u odnosu na čist PMMA. Razlog za ovo sniženje T_g je interakcija QD sa osnovnim polimernim lancem PMMA. Rezultati ispitivanja nanoindentacijom pokazuju da dodatak QD povećava redukovani modul elestičnosti i tvrdoću. I ovakvo ponašanje kompozitnog filma ukazuje na interakciju nanočestica QD i osnovnog polimernog lanca PMMA. Ove čestice sprečavaju pokretanje polimernog lanca i na taj način poboljšavaju mehanička svojstva kompozita.Rezultujući fluorescentni spektar kompozitnog filma pokazao je da su QD zadržale svoja optička svostva i da odlično reaguju u PMMA matrici na pobudu.

Ključne reči: Kompozitni materijali, monokristal, kvantne tačke, fluoroscencija, nanoindentacija

Naučna oblast: Inženjerstvo materijala

UDK: 66.017:548.55

7

SYNTHESIS AND CHARACTERIZATION OF OPTICAL POLYMER COMPOSITES BASED ON SINGLE CRYSTALS

Abstract

Composites with a polymer matrix based on single crystals have great potential in the field of optical communication systems where active micro to nano crystals dispersed in an optically transparent matrix. The subject of this doctoral thesis includes research in the field of optoelectronic functional composite materials with a polymer matrix for use in electronic technologies, as well as in the field of communications and navigation techniques and possibilities for developing integrated optics and photonics. Polymer optoelectronic composite materials with controlled optical properties were synthesized. One way is use of the inorganic particle size smaller than the wavelength of electromagnetic radiation to avoid scattering, another way is the installation of materials with similar values of the refractive index. Within this selection of theses materials fell on the poly (methyl methacrylate) with an index of refraction $n_{600} = 1.49$, and calcium fluoride with $n_{600} = 1.43$.

Research was organized in two directions: a) synthesis of single-crystal CaF_2 as a functional carrier and embedding in the polymer matrix; b) synthesis and characterization of polymer matrix composites incorporating CdSe quantum dots. In such an organized way research can be traced and influence the organization and size of crystals in the optical and mechanical properties of the resulting composite.

Modified vertical Bridgman method in a vacuum obtained is a high quality single crystal CaF_2. The resulting crystal was investigated by Raman and IR spectroscopy. The crystal structure was confirmed by X-ray structural analysis. In accordance with the theory group spotted one and two infrared Raman optical mode. Low photoluminescence testifies that the concentration of oxygen defects in CaF_2 was small. All completed surveys show that the resulting single crystal CaF_2 has a good optical quality. After grinding, the particles of the single crystal are embedded in a polymer matrix of poly (methyl methacrylate). Incorporating

monocrystalline CaF$_2$ composite was obtained with preserved optical properties of single crystals, whereas the thermal and mechanical properties improved.

Quantum dots (QD) are monocrystalline semiconductor nanostructures, whose head electric charge spatially confined in all three dimensions. The material from which the QD made defines their characteristic energy. However, the exact value of the energy gap are determined by the size of the point. The consequence of this is the fact that quantum dots made of the same material but different sizes emit radiation of different wavelengths. The present work was carried out testing of the conditions for obtaining a QD doped poly (methyl methacrylate) thin film by method of casting from solution. The thermal properties of composites were investigated by the DSC method. Optical properties were investigated by analyzing the emission spectrum of picosecond measurement system for measuring the lifetimes of luminescence. Mechanical properties were tested using the method of nanoindentation. The results of DSC revealed that for composite doped PMMA film have somewhat lower T_g in comparison with pure PMMA. The reason for this decrease in T_g is QD interaction with the main chain of the polymer PMMA. Nanoindentation test results show that the addition QD increases reduced modulus of elasticity and hardness. I kind of behavior of the composite film points to the interaction of nanoparticles QD and the base polymer chain PMMA. These particles prevent the initiation of a polymer chain and thus improve the mechanical properties of the composite. Fluorescence spectrum of the film showed that QD retain their optical properties and respond well in the PMMA matrix to excite.

Content

THEORETICAL PART

Introduction to composite materials

Composite materials formed from two or more material whereby the material formed is characterized by new properties compared to the starting materials [1-9]. Composite materials are consisting of the corresponding reinforcing materials and matrix who connecting the carrier material. These components are typically not solvable one within the other and it is possible to determine the physical boundary between them. With the combination of starting materials can be produced easy, very strong, tough and impact resistant material and the like. One simple scheme for the classification of composite materials is shown in Figure 1 [1].
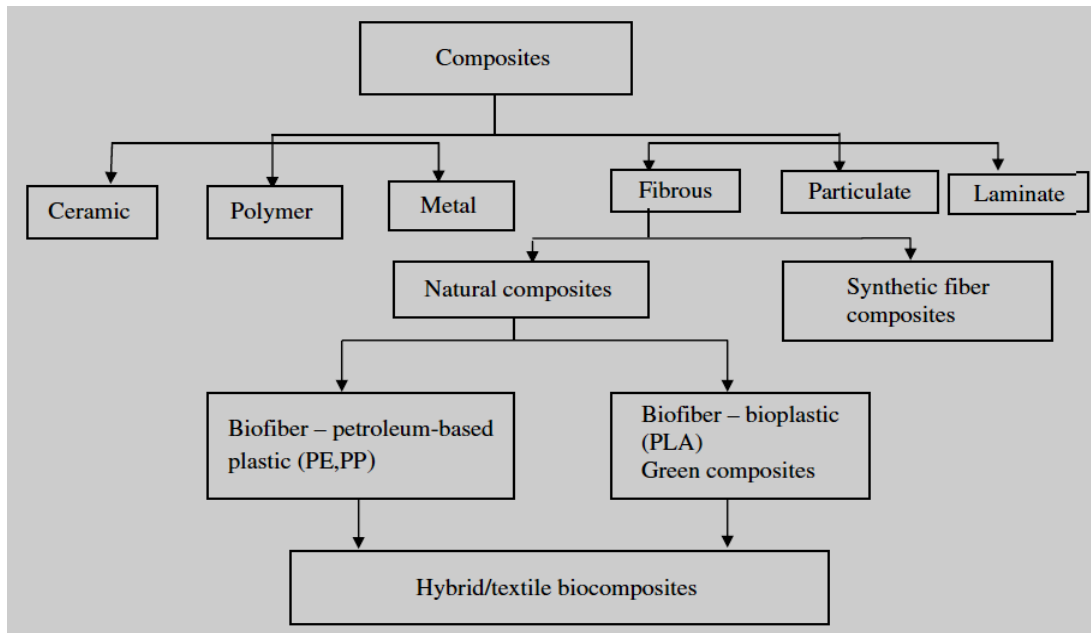
Figure 1. A classification scheme for the various composite type materials [1].

Composites are rightly considered the materials that will be the main direction of innovation in the near and distant future, new material. Thanks to the fact that each composite

combine the properties of two or more materials, composites are increasingly replacing classical materials in engineering. This material poses the specific features that enable their dominant functional application, but these materials are called functional composite materials (Figure 2).

It is important to emphasize that the collection of useful properties of composites can be achieved not only by combining simple materials but also the macroscopic and the microscopic atomic scale.

In search of new composite materials, constantly appearing new combinations: metal-glass; carbon-glass; ceramic-metal, etc. "Installation" simple substances from simple to complex materials achieved by modern methods of synthesis and processing of materials.

This tendency leads matter in a row:

atom → crystal (amorphous) structure → polycrystalline structure → material
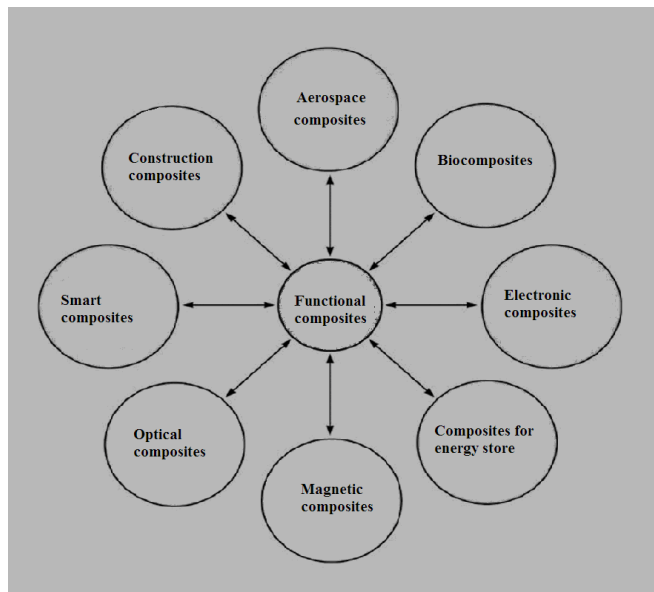
Figure 2. Functional composites.

Structure of composite materials

Composite materials or a composite, are multi-phase multi-component materials whose phases possess physical and mechanical properties which differ significantly, with exposed border area and the surface between them, as shown in Figure 3. The structure of the composite consists of a continuous phase in which is built-in one or more discontinuous phases. The continuous phase is called the matrix; a discontinuous phase is referred to as an active filler or reinforcement, depending on the function performed by the composite. The properties of composite materials themselves depend on the continuous and discontinuous phases of, and formed from the border area between them. Discontinuous phase in addition to the mechanical properties can be modified and some other properties of composites such as, thermal, acoustic, electric, magnetic and optical. Appropriate choice of constituents and their relative mass ratio in the structure of the composite material can be obtained materials with the desired density, strength, hardness, stiffness, corrosion resistance, wear resistance, the ability of thermal and acoustic insulation, etc.
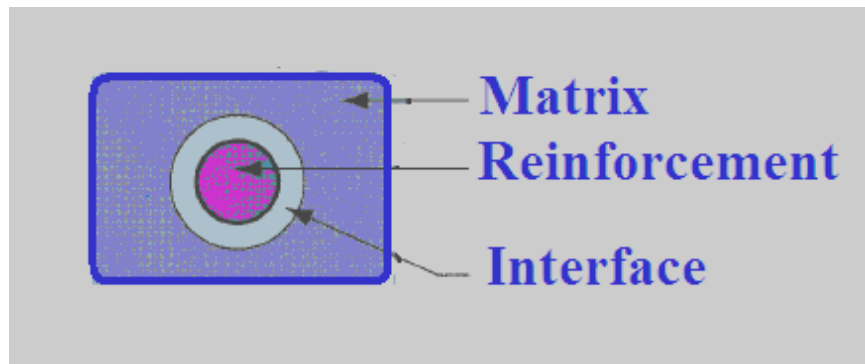
Figure 3. Structure of composite materials.

The border area is the interfacial area that has adequate capacity and limit the interface surfaces that have a very important role in determining the critical properties of composites, for example, the intermediate stages of mechanical stress is transferred from the matrix to gain and vice versa. Also, the intermediate stage plays a decisive role in the long-term stability of the composite.

Development of advanced composite materials to a considerable extent based on the possibility of designing their structure and properties, various methods of synthesis and production. The resulting set of properties of the composite material is achieved not by the combination of materials in a simple and more macroscopic and microscopic in nano-scale.

In search of new composite materials, constantly appearing new combinations between the basic classes of materials: metals, ceramics and polymers. Synthesis of materials from simple to more complex materials shall be appropriate to the specific methods of making changing the structure of the nano to macro dimensions in order to achieve optimum desired properties. This approach enables the development of structurally very complex multifunctional materials in which the design of the structure extends from the nano level - nano materials, microlevel - microcomposites, to macro levels - macrocomposites.

Classification of composite materials

Classification based on the composite matrix

Depending on the matrix composite materials can be classified as synthetic composites: ceramic (CMC) polymer, (PMC), carbon (SS) and metal (MMC) or natural composites: matrix of lignin (wood) or collagen (biocomposites) as shown in Figure 4.
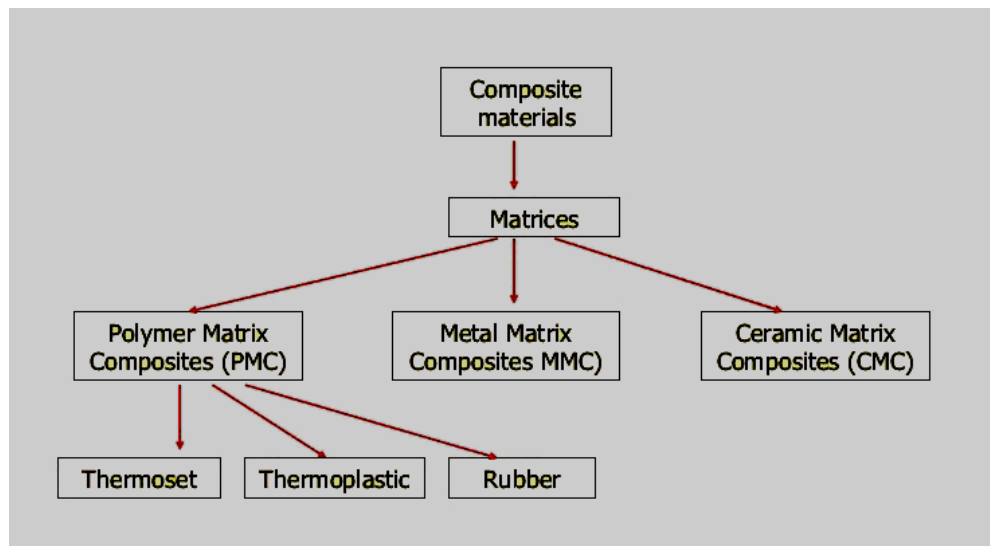
Figure 4. Classification of composites based on matrices [2, 3].

Classification of a composite base on the form of the disperse phase

The largest number of the composite has been developed and is manufactured with the aim to improve their mechanical properties, such as stiffness, strength or toughness high temperature resistance. Based on that, the most commonly used methods of classification of composite according to a joint mechanism to strengthen, as the latter depends on the geometry of the reinforcing composites classified according to the geometry of the characteristic amplification unit. Composite materials can be classified into three main categories: particles reinforced, fiber reinforced composite materials and laminate. The shape of the discontinuous phase can be different and can be approximated by a sphere (particles), cylinder (fiber sticks), plate-layer (laminate), irregular tiles (flakes) or irregular particles

(filler) [4-5]. Only the classification of composite materials according to the form of discrete phase is shown in Figure 5.
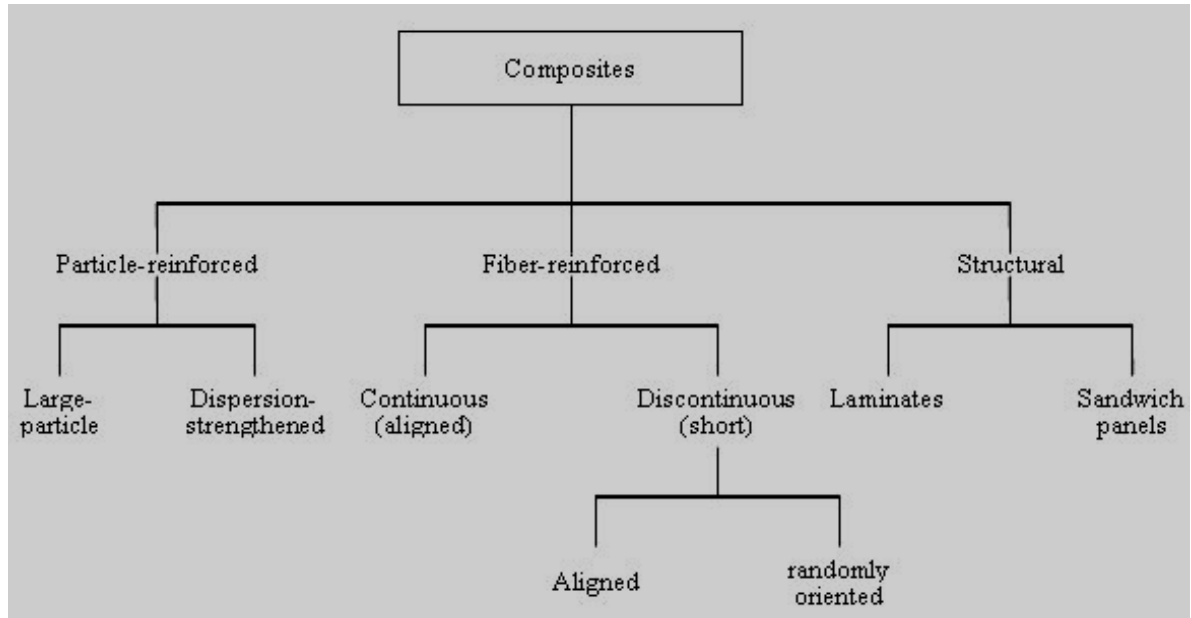
Figure 5. Classification of composite materials [6-10].

Composite materials reinforced with particles

According to this classification, the essential characteristics of the particles are that they are by their nature non fiber. They can be: spherical, cubic, tetragonal, flaked or irregular shape, but they are all approximately equal. Fiber is characterized by a large ratio of length to cross-section. Composites reinforced particles are often called particulate, and with fibers fiber-reinforced composite. Except obvious geometric differences, these two classes of materials also differ in the way the exercise load transfer, and hence in the way it affects the rigidity and strength of the composite material. The concept of load transfer is crucial for understanding the behavior of the composite material to mechanical stress. The composites have properties of strength and toughness because of their synergistic ability to share applied load between the constituents. The efficiency of the composite are strictly determined by the efficiency of the transfer of applied load from the matrix to the reinforcement. And this is on the other hand determined by several aspects such as the quality of the boundary surface, the geometrical orientation, and mechanical properties of the individual components.

Composite materials reinforced with fibers

The use of fiber as a reinforcement in composite materials based on the following: a) the small diameter of the fiber allows to obtain a larger share of the theoretical strength of the material than in a larger piece of the same material, because it is less likely for the occurrence of defects or deficiencies in the structure of materials that contribute to the reduction of strength; b) the optimal ratio of length and diameter of the fibers to a successful transfer the external loads to the fiber matrix of the border area; v) a high degree of flexibility and elasticity of the fiber allows the use of various techniques to create very complex woven structure as a form of reinforcement in composites. The fibers differ according to: a) the type, b) the length, c) the diameter, d) orientation and e) hybridization.

Laminate composite materials

A laminated composite represents a class of very attractive structural materials. Exceptional advantage of these signage materials are their excellent mechanical properties, particularly their specific mechanical properties, as well as the possibility of the introduction of flexibility in the design of structural elements of the composite. The structure and nature of the composite laminate are different than those of conventional polycrystalline structural materials. Similarly, the initiation and propagation of fracture, as well as criteria of destruction and resistance of materials are different than in conventional construction materials.

Organic/inorganic optical composites: basic concept

The organic/inorganic optical composite is defined as a composite which consists of an organic host material - matrix and inorganic optical active inclusions. Those optical inclusions could be in various dimensions meso to micro to nano. One way to obtain highly transparent composites is by using fillers with a particle size smaller than the scattering limit [11]. Another way is to use the so-called ''refractive index matching'' technique, which is often employed in colloid physics [12-16]. Light scattering not only depends on the particle size but also on the difference in refractive index (Δn) between matrix and filler materials. The smaller Δn, the lower is the amount of scattered light. When n_{matrix} equals n_{filler}, the composite appears transparent independently of the size of the filler.

Wafer-based single-crystalline inorganic semiconductors currently enable the most efficient solar cells. However, their rigidity precludes the use of inexpensive processing schemes such as roll-to-roll manufacturing and/or their installation in flexible forms. While amorphous and polycrystalline films of inorganic semiconductors can be grown on flexible substrates such as stainless steel or polymeric sheets, solar cells processed from these disordered absorber materials exhibit lower solar photovoltaic conversion efficiency than single crystal. Organic and hybrid organic/inorganic solar cells offer flexibility and processability, but suffer from low efficiency and instability of the organic light-absorbing and/or charge-conducting material under prolonged illumination. We describe in this dissertation the fabrication of arrays of highly oriented, single-crystalline CaF_2 embedded in a polymeric film. This composite material combines the photo stability and solar-energy conversion potential of high quality single-crystalline semiconductors with the processability and flexibility of polymers.

Organic/inorganic optical nanocomposites

Photonic nanocomposite materials are generally constructed by embedding an optically functional nanosized guest material (e.g. nanoparticles, nanocrystals and molecules) into an optically transparent host matrix such as organics (e.g. (photo)polymers, polymer

blends, liquid crystals) or inorganic solids (e.g. glasses and ceramics). The addition of the guest material to the host matrix can yield significant improvement and modification in their mechanical, thermal, transport and optical properties over bulk materials. As a result, high-performance photonic functionalities, with environmentally stable optical characteristics, can be achieved. In addition, nanocomposite materials can be tailor-made via the control of their linear optical properties, such as the refractive index and absorption as well as their laser, electro-optic, and nonlinear optical properties. For example, the incorporation of liquid crystalline droplets in polymers gives electrically controllable light scattering characteristics, ideally suited for display and optical switching applications. Dispersing inorganic or organic nanoparticles in optical materials leads to a strong response to incident light. Indeed, ferroelectric nanoparticles in cholesteric liquid crystals enhance the electro-optic response of the mixture. In photopolymers, nanoparticles make the formation of a high-contrast holographic grating possible, which should prove useful for applications such as optical elements and data storage. Moreover, nanoparticles dispersed in photopolymer can be assembled by light, providing the realization of multi-dimensionally structured materials, highly relevant for photonic and electronic applications. The local-field effects in nanostructured materials can provide a large enhancement of the nonlinear optical response and the improvement of the light amplifying properties. These areas are represented in this special issue, along with contributions to modelling of photonic crystal structures and holographic grating formation in polymers. Because nanocomposite materials provide a new method to improve the environmental stability of materials, as well as interesting optical properties, they should open new routes for applications in photonics.

Polymeric nanocomposites consisting of inorganic nanoparticles and organic polymers represent a new class of materials that exhibit improved performance compared to their microparticle counterparts. It is therefore expected that they will advance the field of engineering applications. Incorporation of inorganic nanoparticles into a polymer matrix can significantly affect the properties of the matrix. The resulting composite might exhibit improved thermal, mechanical, rheological, electrical, catalytic, fire retardancy and optical properties. The properties of polymer composites depend on the type of nanoparticles that are incorporated, their size and shape. There are two important factors that should be discussed

about optical nanocomposites: one is the scattering problem, and the other is the dielectricity. Although 1D nanostructures such as carbon nanotubes [10-14], CdS nanoparticles [15], Mo nanowires [16] and ZnO nanorods [17] have been embedded in polymers, the process described herein uniquely combines flexibility, atomic-scale crystallinity, and long-range order in a single material [18].

The essence of the subject can be concisely described as follows: The important prerequisite is that the inorganic nano-inclusions are randomly dispersed in the organic host material without aggregation to form a heterogeneous composite structure as schematically drawn in Figure 6.
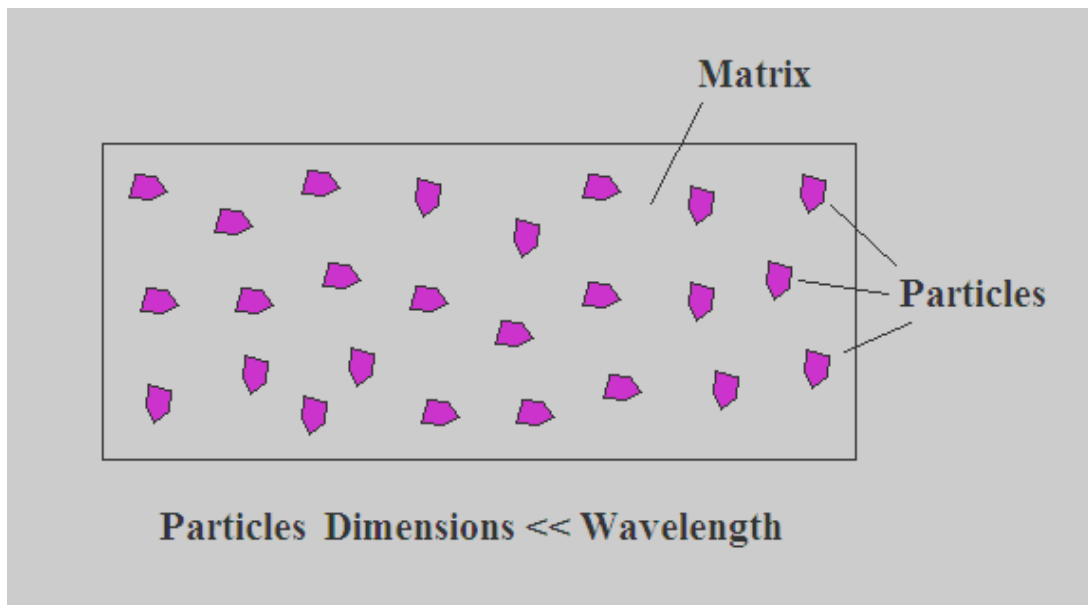
Figure 6. Scheme of optical nanocomposite.

When the nano-inclusions are randomly dispersed, the scattering arisen from the interaction between propagating light and nano-inclusions is substantially expressed by the Rayleigh scattering theory [19]. For this reason, high transparency could be maintained when the diameter of the nano-inclusion is optimized by taking into account the ratio of the refractive index of the nano-inclusion to that of the host material. There does not seem to be a universal definition on the terminology "nanocomposites". According to Komarneni [20], the word "nanocomposites" was first used during the period 1982-1983 to describe the major

conceptual re-direction of the sol-gel process, in which the solution of sol gel process is used to create maximally heterogeneous rather than homogeneous materials.

According to Prasad [21], nanocomposites are random media containing domains or inclusions that are of nanometer size scale. Prasad classifies two types of nanocomposites. One is that the size and domains of inclusions are significantly smaller than the wavelength of light. The other is that nanocomposite contains domains/inclusions comparable to or larger than the wavelength of light.

Aside from whether sol-gel technology is used, the key of the nanocomposite is "heterogeneity". As was mentioned above there are two structural members in a nanocomposite; one is inclusion and the other is host/matrix material. Our central concern research is to study heterogeneous materials whose inclusions are far smaller than the wavelength, which is the first type that Prasad classified, as schematically depicted by Fig. 6.

Nanocomposite polymer films doped with QD have many commercial or potential applications in biological labeling and diagnostics, LED's, electro-luminescent devices, photovoltaic devices, lasers and single electrode transistors [22-26]. High performance in polymer blends and composites can be achieved by addition of a nano size filler component into a polymer matrix. In this regard polymer nanocomposites present a promising alternative of conventional composites. Recently, studies on blends of immiscible polymers containing nanoparticles have attracted the attention of several research groups [27-30]. These studies suggest that under certain conditions the polymer molecules and the nanoparticles should not be regarded as individual entities within the blend, but instead as complex aggregates.

Polymeric nanocomposites consisting of inorganic nanoparticles and organic polymers represent a new class of materials that exhibit different performance compared to their microparticle counterparts. The properties of polymer composites depend on the type of nanoparticles that are incorporated, their size and shape.

Poly-methyl-methacrylate (PMMA), a transparent thermoplastic polymer, has been widely used in many commercial applications due to his high impact-resistance, ease of fabrication, low density, and cost-effective technologies [31]. For example, PMMA has been one of the most popular substrate materials in making polymer-based micro fluidic devices to

perform chemical and biological assays due to its excellent chemical, physical, biological, mechanical, optical and thermal properties [32-35].

Semiconductor nanoparticles are notable for their wide fundamental research and industrial applications [36, 37]. Their defining characteristic is their size which is in the range of 1-100nm and excellent chemical processibility. The strong confinement of excited electrons and holes leads to dramatically different optical and electronic properties compared to the bulk semiconductor [38]. Many studies have been made on III–V and II–VI semiconductor quantum dots (QDs) all over the world. For II-VI QDs, CdSe QDs prepared by chemical methods are the most popular [39]. Many studies have been focused on CdSe QDs because of its high luminescence quantum yield, narrow band gap and a variety of optoelectronic conversion properties compared to bulk CdSe [40].

Polymer nanocomposites with QDs have a wide range of applications in optoelectronics and biosensing as solar cells, light emitting diodes and bio-labeling [41, 42]. Those nanocomposites are usually used in film form in which the distance between QDs in polymer matrix is fixed. Inter-particle distance between QDs in film plays a crucial role in determining the quantum yield of fluorescence. QDs in polymer matrix usually aggregates in clusters and reduced quantum yield, so it is important to control both dispersion and film production process to retain its initial quantum yield [43-47].

Scattering phenomena was discussed circumstantially and quantitatively by Rayleigh and Mie [48-51]. First, the scattering problem was formulated as that the scattered electromagnetic waves can effectively be dipole radiations in origin. In the Mie theory, the scattered spherical electromagnetic wave will interfere with the incident light expressed as the expansion of vector spherical harmonics to form an electromagnetic wave which is to be actually observed.

Maxwell-Garnett proposed the concept of the effective dielectric property for the first time [50-52]. Dielectric property of a homogeneous material in terms of the relation between the microscopic property (the molecular polarizability α) and the macroscopic property (the dielectric constant ε) was derived by Clausius and Mosotti, which is equivalent to the formula derived by Lorentz and Lorenz later with respect to the refractive index n.

Optical nanoparticles-quantum dots (QD)

Nanoscale reinforcements have found extensive interests in the polymer field, because reinforced materials (composites) display better structural mechanical properties compared to the pure polymers. Semiconducting nanoparticles (quantum dots) have been material of interest when it comes to polymer reinforcement due to their exciting properties especially their unusual size-dependent optical properties [53, 54].

Quantization of energy states, or spatial limitation of charge carriers is performed by forming a potential barrier. Depending on the choice of the potential barrier confinement can be performed in one or more directions, so as to obtain a thin film, or the pit (quantum well, QW), the wire (quantum wire, QWR), or point (quantum dot, QD) or box. If you need to obtain a semiconductor film spatial limitation is performed in one direction (one-dimensional quantum confinement). The wire is a two-dimensional quantum-confined structure, while the point of quantum effect occurs in all three directions. In Figure 7 shows a schematic representation of these structures, as well as the massive semiconductor in which there is this effect.
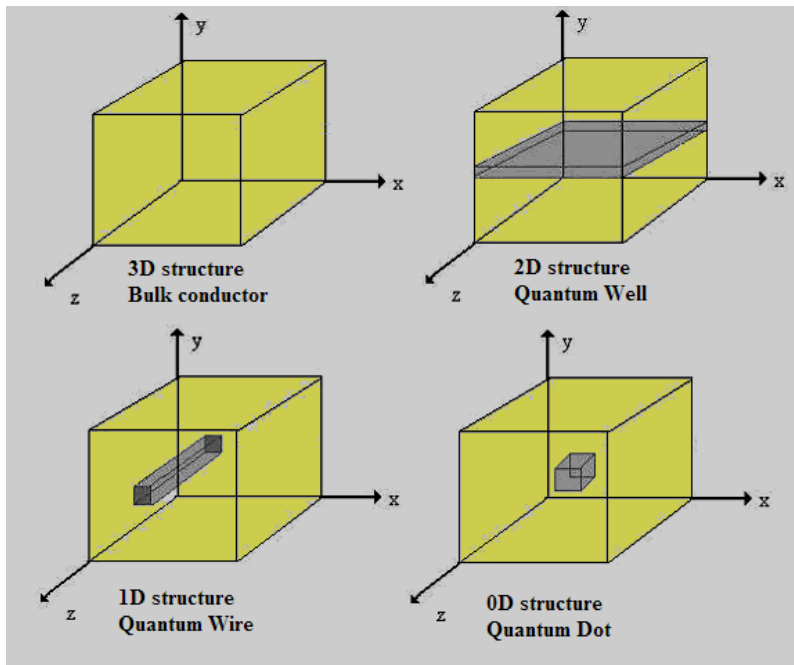
Figure 7. A schematic representation of the quantum-confined structures - bulk, quantum well, quantum wire and quantum dot.

In the direction free from the quantum confinement of charge-free to move, so as to form so-called electric or gas oscular. In quantum electronic or oscular gas occurs in two dimensions, so that one's called 2D structures. Quantum wires are 1D and 0D quantum dots-structure. Existence of gas in quantum well wires and causes the formation of energy subarea, while the quantum dots arise discrete states, an analog energy states of an atom, and the structures referred to as artificial atoms.

Quantum dots are semiconductor nanostructures whose charge carriers spatially confined in all three dimensions. As a result, characteristics of these systems are quite different from macroscopic properties of semiconductors. One of the more interesting properties of quantum dots is their coloration. The material from which are made the point defined by their characteristic values of the energy, however, the exact value of the band gap are determined by the size of points, or to the strength of the quantum confinement. The consequence of this is the fact that points are made of the same material but different sizes emit radiation of different wavelengths. Larger point emit radiation at longer wavelengths fluorescence spectra as a result of the size of their energy gaps.

Recent researches in nanotechnology suggest that the spot size may have shown some influence on its coloration or Technical characteristics of its spectrum. It is shown that the size of the point directly affects the fluorescence lifetime. Electron-hole pairs in larger counts are living longer because they need less energy to excite.

By studying excitation and quantum dots in semiconductors led to the conclusion that the interaction of longitudinal optical phonons and excitons can be strong or weak depending on the used energy. Variability of this interaction comes from the discrete energy levels of quantum dots, or the capabilities of their changing size or chemical composition of quantum dots.

If the difference between the primary and the first excited energy levels of quantum dots is comparable with the energy of phonons occurs very strong coupling of excitons and longitudinal optical phonons. The result of this regime is the creation of polarons. Excitation photoluminescent spectra are obtained on which clearly can be observed the formation of these particles in the form of Stoks lines. The energy difference between this line and the excitation line of the laser corresponds to the energy of binding to the polaron.

By recording the spectra of shallow photoluminescent quantum dots found that characterize polaron excited states, whose energy difference corresponds to the energy of longitudinal optical phonons. An important feature of polarons is their stability at ambient temperatures and relatively long lifetime.

Poor excitation-phonon interaction occurs when the energy difference between the base and the first excited state is significantly higher than the energy of longitudinal optical phonons. In this case, the excitation is formed-phonon complex that can be observed as a broad emission line of the photo luminescent and resonantly excited photo luminescent spectra. Since the excitation laser line is shared energy value corresponding to the multiple phonon energies.

Production of semiconductor nanostructures structure rapidly was developed from seventies of the last century when it enabled the application of thin layers of semiconductor material with a precision deposition to the dimensions of individual atoms. Technologies that they were derived are thin layers of epitaxial, molecular beam (*Molecular Beam Epitaxy -* MBA), and metal-organic chemical vapor deposition (*Metal - Organic Chemical Vapor Deposition* MOCVD).

Single crystal in optical active polymer composites

Crystal growth

Crystal growth involves the controlled deposition of atoms onto a single-crystal seed by making use of a phase change: liquid to solid, vapor to solid, or even solid (in a metastable form, for example) to solid. The pure metal solidification takes place at a constant temperature that is characteristic of a given metal – temperature of solidification-crystallization. Since the internal energy of the disordered liquid is higher than the ordered crystalline state, the transition from the liquid phase to the crystalline state is accompanied by release of heat. Latent heat that develops during curing is sufficient to maintain the liquid at a constant temperature for the remainder of the cure. Applying elementary thermodynamics of the solidification process can be considered the relationship between temperature and the latent heat of solidification. The curing temperature is defined as the temperature at which the free energy of the liquid and the solid phase equal to:

$$G_L = G_S \tag{1}$$

where is G_L- Gibbs free energy of the melt, G_S- Gibbs free energy of the solid .

Free energy can be expressed in the following equation:

$$G = E - TS + PV \tag{2}$$

where is : E - internal energy phase, T - absolute temperature, S - entropy is a measure of order phase, P- the pressure, V - volume.

At the curing temperature (T_0) of the free energy of both phases are equal:

$$H_L - T_0 S_L = H_S - T_0 S_S \tag{3}$$

where: H_L - enthalpy of the liquid phase, H_S - enthalpy of solids.

Latent heat that is released during the transformation can now be expressed as:

$$L = H_L - H_S = \Delta H = T_0 \Delta S \tag{4}$$

Values for the latent heat ranging from about 2 kJ mol^{-1} for metals with weak

cohesive forces, such as alkali metals, up to 20 kJ mol^{-1} for metals with strong cohesive forces between the carbon atoms, such as the tungsten and other transition metals [57, 58].

ΔS, as a measure of the change of order of atoms during the transformation of the liquid-solid can be determined from Eq. (4) as the ratio of the latent heat and the equilibrium temperature of solidification

$$\Delta S = \frac{L}{T_0} \qquad (5)$$

ΔS is relatively independent of the structure of the solid phase, i.e. arrangement of atoms changes during the transition from one phase to another is small.

This shows that when the metal solidifies, the change in entropy during solidification of metals is relatively small.

Supercooling

Due to the continuous and rapid cooling of the liquid phase it could be happened that melt go to super cooling. In real systems, and usually takes a final subcooling as the driving force to begin crystallization. Cooling curve has a different shape depending on the conditions of cooling of the melt, temperature, specific heat, thermal conductivity, the material of the court and melt latent heat. If there are enough metal in the system, due to the released latent heat, the temperature of the melt is rapidly raised until reaching the equilibrium temperature of solidification, and hence the hardening process stops. If there is a smaller amount of metal released latent heat is not sufficient to increase the temperature of the melt to equilibrium, but only reduced supercooling, i.e. reduces the growth of the solid phase. When crystallization of alloys is causes supercooling due to changes in the composition of the liquid phase along the border area, it is so-called constitutional supercooling.

Nucleation

The process of nucleation describes the beginning of the formation of one phase in the other where necessary to overcome barriers in the free energy required for the formation of a new phase. Nucleation plays an important role in the initial formation of crystals from the vapor and liquid phases. During the curing process the transformation of a new phase begins with the appearance a few very small particles of a new phase. The growth of a new phase of relations depends on the surface to the volume, but small particles tend to dissolve, a big to grow. In fact, there is a critical particle size that divides those that tend to be dissolved, called embryos, of those that grow, called nuclei.

Nucleation develops in several stages: 1) the collection of appropriate kind of atom diffusion or some other kind of movement; 2) structural changes in one or more unstable intermediate structure; 3) forming the nucleus of a new phase. This is followed by a new phase of growth also in several stages: 1) transport of materials by diffusion through the old stage; 2) transport across the interface into a new phase; 3) transfer of the interior of a new phase diffusion. All these stages are thermally activated processes, which means that the barriers to overcome thermal energy.

Depending on whether the emergence of a new phase particles coming spontaneously or due to the presence of foreign particles as centers of formation of the new phase are different homogeneous and heterogeneous nucleation.

Homogenous nucleation

It is assumed that a small area of a new,stable phases occurs in the middle of an old, unstable materials. We consider the growth of the solid from the liquid phase thus eliminating the problem of stress. It is also assumed spherical shape of the nucleus. If the temperature suddenly drops below the melting point, the change of free energy per unit volume of solidified phase, ΔG_v will be negative. The total free energy changes for the particle radius r will be:

$$\Delta G = 4\pi r^2 \gamma - 4/3 \ \pi r^3 \Delta G_v \qquad\qquad (6)$$

where γ is surface tension. Each member of this equation is shown in Figure 8.

Since the particles increases, and its free energy increases until it reaches a radius r^*. Particles smaller than the radius r^* will be dissolved, thus lowering the free energy. These are embryos. Particles larger than the radius r^* lower free energy face growth, and are called nuclei [59]. For a nucleus formation, energy must be added ΔG^* and it is thermal activation of process. From Figure 8, it is clear that ΔG^* and r^* can be calculated from the maximum determining the Equation (6). By equating the first derivative to zero:

$$r^* = -\frac{2\gamma}{\Delta G_V} \tag{7}$$

$$\Delta G^* = \frac{16\pi\,\gamma^3}{3(\Delta G_V)^2} \tag{8}$$

In this way, it is possible to determine the critical size of the nucleus and the energy for its formation in order to begin growth of a new phase.
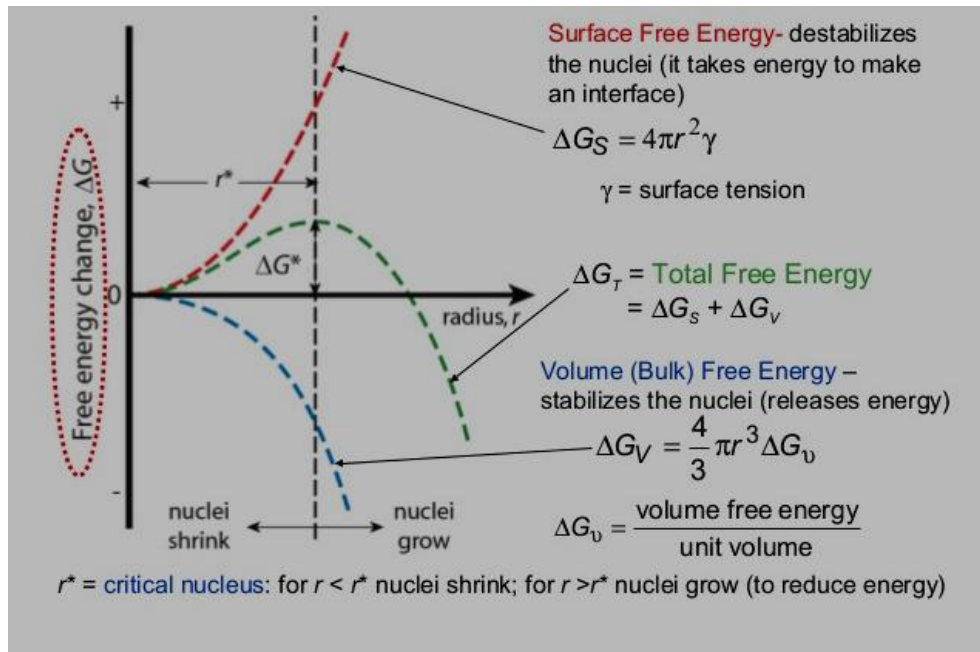
Figure 8. Gibbs free energy dependence on nucleus diameter [59].

Temperature dependence of ΔG^* could be obtained if it is assumed that ΔH_v and ΔS_v have slow temperature dependence. On melting point, T_0, is $\Delta G_v = 0$,:

$$\Delta S_V(T_0) = \frac{\Delta H_v(T_0)}{T_0} \qquad (9)$$

where T_0 - equilibrium melting temperature , ΔH_V - specific volume enthalpy, ΔS_V - volume entropy change:

$$\Delta G_V(T) \cong \Delta H_v(T_0) - T\Delta S_V(T_0) \cong \Delta H_v(T_0)\left[1 - \frac{T}{T_0}\right] \qquad (10)$$

From tnhis equation could be obtained supercooling for starting solidification:

$$\Delta T = T_0 - T = T_0 \frac{\Delta G_V}{\Delta H_V}$$

$$(10a)$$

It takes subcooling in real systems is of the order $\Delta T = 0.2 \times T_0$ [57]. For crystal growth from the melt expression for subcooling for homogeneous nucleation is approximated by the equation (11) [60] with:

$$\frac{\Delta T}{T_0} = \frac{a}{r^*} \qquad (11)$$

where a is atomic diameter.

If the total number of particles of a new phase N_0, the number of nuclei of critical size, N^*, can be calculated from equation:

$$N^* = N_0\, e^{\frac{-\Delta G^*}{kT}} \qquad (12)$$

where k –Boltzman constant.

$$N^* = N_0 \, e^{\dfrac{-16\pi\gamma^3}{3(\Delta G_V)^2 kT}}$$

(13)

This equation relates the probability of nucleation of solid phase with the probability of the existence of the critical nucleus size. N^* is very low until a critical value ΔG_v is acheived when growing rapidly in a very small interval. This has the effect of increasing the saturation, subcooling, whereby no nucleation occurs until a critical condition.

Then suddenly begins to form a large number of nuclei. Further development of the term leads to the equation for the velocity of nucleaton [60]:

$$N^* = B_1 \frac{D_L}{D_{LM}} e^{\left[-\dfrac{16\pi\gamma^3 T_0^2 V_S^2}{3\Delta H^2 \Delta T^2 kT} \right]}$$

(14)

where are: B_1 - a constant that depends on the particle size and the surface energy, D_L - difussion coeficient, D_{LM} - melt difussion coeficient on T_0, V_S - molar volume of solid phase

The shape of the curve is nearly vertical, which means that an increase of a few percent saturation increases the rate of nucleation and up to a hundred times [60]. The explanation for this should be sought in the exponential dependence of the free energy relationships created nucleus and kT, the thermal energy of the individual atoms. For the heterogeneously nucleating critical droplet, the radius is exactly the same as for the homogeneous case (Figure 9).
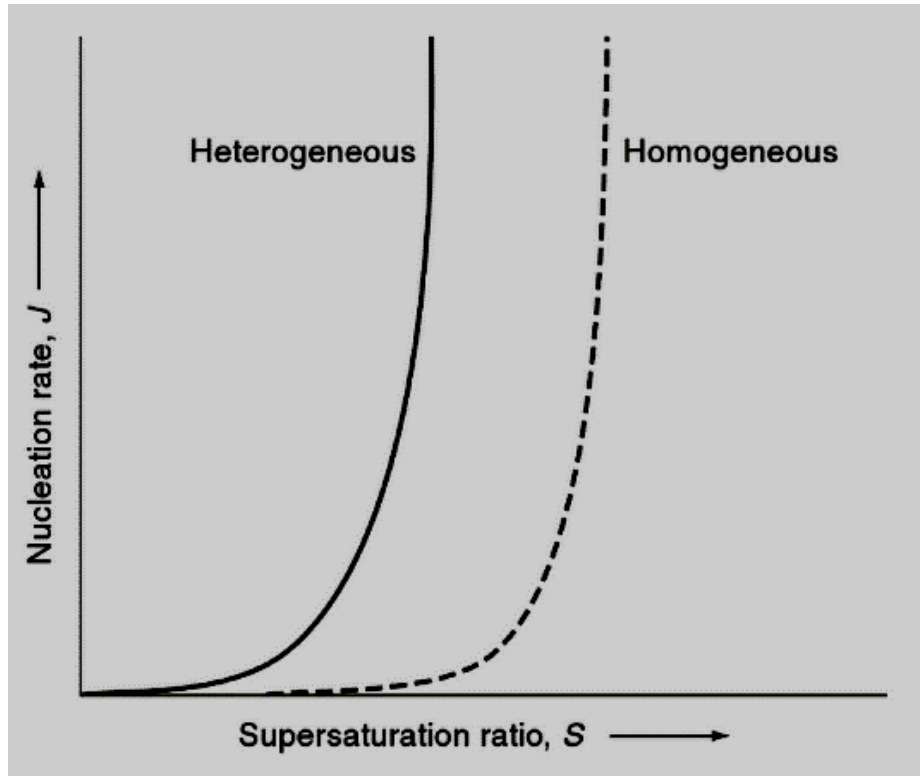
Figure 9. The rate of nucleation depending on the difference of free energy undrcooled melt and crystalline phases: a – homogenous nucleation, b - heterogeneous nucleation curve.

Heterogenous nucleation

Heterogeneous nucleation occurs due to the presence of foreign particles in the melt serving as a substrate on which it appears a new phase. Theory of heterogeneous nucleation treated the nucleus as a drop on a flat surface substrata - nucleus agent (Figure 10). Give nucleus also has the critical size at homogeneous nucleation when the spherical shape. In this case introduces a new notion, θ - contact angle.
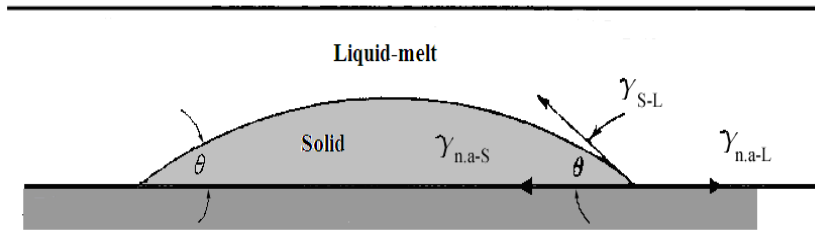
Figure 10. Heterogeneous nucleation [57].

At the intersection of three surfaces equilibrium forces will be:

$$\gamma_{n.a-S} = \gamma_{n.a-L} - \gamma_{S-L}\cos\theta \tag{15}$$

where is $\gamma_{n.a-S}$ - the surface tension of the contact surface nucleation agent - solid phase; $\gamma_{n.a-L}$ - the surface tension of the contact surface nucleation agent-liquid phase; γ_{S-L} - the surface tension of the contact surface of the solid-liquid phase.

It is obvious that the surface "n.a-S" will replace one equivalent size "n.a-L"surface and that $\gamma_{n.a-S} < \gamma_{n.a-L}$. Because of this phenomenon, "n.a-S" surface reduces the energy associated with that area. It is thus possible to reach the surface energy of the heterogeneous nucleation if the total surface energy of the subtracted said amount of energy that decreases the occurrence of "n.a-S" area. It is obvious that the surface energy of heterogeneous nucleation surface energy lower than the homogeneous nucleation and will do it much easier to reach.

When performing expressions for the free energy for formation of the nucleus should take into account the contact angle while coming to the fore:

$$\Delta G^* = \frac{16\pi\gamma^3}{3\Delta G_V^2} \cdot \frac{(2+\cos\theta)(1-\cos\theta)^2}{4} \tag{16}$$

Surface agents for formation of a nucleus can be described value of contact angle θ. Better are those agents with low values of the angle θ, or those that allow solid phase "wets" soluble component. By developing the expression of heterogeneous nucleation rate [60]:

$$N^* = B_1 \frac{D_L}{D_{LM}} e^{\left[-\frac{16\pi\gamma^3 T_0^2 V_S^2}{3\Delta H^2 \Delta T^2 kT} \cdot f(\theta) \right]}$$ (17)

It can be seen that it is from the homogeneous nucleation rate varies by a factor of $f(\theta)$:

$$f(\theta) = \frac{(2+\cos\theta)(1-\cos\theta)^2}{4}$$ (18)

Dependence rate of homogeneous and heterogeneous nucleation is shown in Figure 9 [61] where curve a) corresponds to a homogeneous, and curve b) the rate of heterogeneous nucleation. It is obvious that for heterogeneous nucleation takes much less than the subcooling for homogeneous nucleation.

Growth of new phase

When it formed the nucleus of the further growth of a new phase depends on the surface structure of the solid phase and the possibility of further growth by forming new level. Although the importance of forming a new level has long been recognized, the complexity of the problem makes it difficult mathematical treatment. Therefore introduced a large number of approximations that shed light on the problem and allow the execution of mathematical solutions. Thus, Jackson [62], using the Bragg-Williams-term statistics are given for the change of surface energy of new phase:

$$\frac{\Delta G^S}{N k T_0} = \alpha(1-x)x + x\ln x + (1-x)\ln(1-x)$$ (19)

where: N - total number of seats on the surface, k - Boltzmann's constant, T_0 - equilibrium temperature, x - the share of occupied places on the surface, α - is given by the equation:

$$\alpha = \frac{L}{kT_0}\xi \qquad\qquad (20)$$

where are: L - latent heat, ξ - factor which depends on the structure of the solid phase and the orientation of the boundary surface.

For values $\alpha < 2$ free energy surface has a minimum for x = 1/2, which means half of the city when completed. For $\alpha > 2$ area has a minimum free energy, or when very few places are filled or when there are very few vacancies. For large values of α minimum of ΔG^S for a fraction of the city filled $e^{-\alpha}$ and for a fraction of vacancies $e^{-\alpha}$.

Factor α according to Equation (20) consists of two baths: ξ, which as has been said, depends on the structure and orientation of the border area, and of Lk/T_0 represents the change in entropy of the system during the phase transformation. Term ξ is always less than 1, and the closest to the value of 1 for the most densely packed levels in the structure of the solid phase, while its value decreases progressively less densely packed levels. The change in entropy of the system is close to the value of 1 for the growth of melt metal, some ionic and organic compounds. Something more value from 2 to 4, for some transition metals, semiconductors and ionic materials in the growth from the melt. During the growth from the vapor phase value Lk / T_0 is about 10. For the growth of the value of this solution baths are moving in a wide range of values close to that of the growth of the melt during the growth of the stock solution to high levels of growth from dilute solutions. For high molecular weight materials, such as organic molecules and polymers values of the baths can be very high.

If the interface between the solid and liquid phases defined as the boundary that divides all those atoms occupying the position in grid nodes than those who are not in that position observed two basic structures of border areas: rough and flat [63].

Crystallographic level low α - factor (materials with low entropy change such as metals) were "roughened" at the atomic level. In this case, there are whole layers levels that are parallel to the interface and the atoms of the solid phase and liquid phase atoms. Growth of the crystal in this case is relatively fast.

When crystallographic level with high α-factor, such as densely packed with high levels of material change in entropy, there are difficulties in initiating new levels of growth.

These are flat crystallographic plane at the atomic level. Growth is possible with surface dislocation nucleation or much slower than the growth of the "roughened" surface.

The classification of materials on faceted and nefacetirane types based on their morphology growth. Atomic flat boundaries to maximize the bonding of atoms in the crystal and those at the border. Consequently, such a limit shows a small number of connections to the atoms that come by diffusion through the liquid phase. This crystal has a tendency to close any gap at the interface in atomic scale leading education faceted crystals. High entropy creation increases the difference in growth rates between low and high index level. In faceted materials such as intermetallic components high index level easily accept atoms and growing fast. As a result of that level disappear and crystal remains limited slowgrowing planes (low index level).

On the other hand, the atomic rough boundaries still owns many suitable sites for installation of atoms from the liquid phase. Atoms can be added to almost any point of the surface and formed nonfaceted growth. In nonfaceted materials, such as metals, crystal shape is mainly determined by the shape field of heat transfer and diffusion of soluble components.

It should also be emphasized that the border nonfaceted material growth at a temperature close to the melting point, so it takes a little subcooling, while the borders faceted material can have a very high subcooling.

Growth with little change in entropy is isotropic and for a given atomic mobility is relatively fast and at low hypothermia. Materials with large entropy change of slower growth and growth is anisotropic. The greater the change in entropy, the greater the anisotropy and slower growth.

From all we can conclude that the characteristics of crystal growth depends on the entropy of the system changes during growth, crystallographic orientation and mobility of the boundary surface atoms, and not on whether the material is metal, organic compound, or molecular ion.

Shape of crystallization front

The temperature of the boundary surface is different from the temperature and the solid liquid interface due to the latent heat which is released or added, or depending on which process is carried out. The hatch systems still need a final subcooling to hardening process started:

$$\Delta T = \frac{2\gamma T_0}{r L} \qquad (21)$$

where: ΔT - subcooling necessary to begin the process of curing γ - surface tension, L - latent heat.

It takes subcooling in real systems is of the order $\Delta T = 0.2 \times T_0$ [57].

If the temperature of the boundary surface is lower than the equilibrium and leads to solidification, latent heat is generated, and subcooling which leads to solidification is decreased. The solidification slows down and stops at the end of the process. So, to continue the process of promotion of border areas, i.e. solidification, be conveyed free of latent heat. In doing so, we can say that the velocity of conveyed latent heat controls the velocity of progression of the crystallization front (boundary surface), while the direction of the removal of latent heat defines the shape of the boundary surface.

There are two cases that could be describe the direction of the removal of latent heat: a) in the direction of crystal and b)in direction of melt.

a) It is assumed that the boundary surface is initially flat, that the crystal is isotropic and that there is a heat sink in the form of a plane which is parallel to the boundary surface and to maintain the temperature lower than the temperature at the interface. Stability of plane boundary surface can be explained as follows: if the disorder appeared in one region (A) in the direction of the liquid phase, the temperature gradient at A will be less than that the rest region of interface, because part A it is farther from the heat sink. In accordance with the ratio of growth rate and under cooling, but also because of lower velocity of the removal of latent heat, this part will grow more slowly than Part B, so the phase boundary is re-treated. So, if the under cooling is sufficient for

crystallization ensures removal of latent heat in the direction of the crystal, the boundary surface is moving uniformly and tends to be flat without the presence of the disorder.

b) In case of contact of the solid phase with under cooled liquid leads to dendritic growth. The temperature profile in the case of heat dissipation in the direction of the liquid phase. In case of a disturbance-protrusions, the under cooling in the section A is higher than in the part B in relation to the temperature of the boundary surface, so that the section A will have faster growth than section B.

The constitutional subcooling

In cases insufficiently pure elements or alloy, with liquid phase along boundary surface has a different composition relative to the bulk of the melt. Changing the composition causes a change in liquidus temperature along the border area. This phenomenon is called "constitutional under cooling" and is often used to explain many problems during the curing process. Realistically, there is no hypothermia, a new front boundary surface, but only up to a temperature of solidification. Therefore, some authors believe that it is much more effective to talk about constitutional or compositional reduce subcooling [57].

Consider the solidification of binary alloy phase diagram as shown in Figure 11 where equilibrium coefficient, k_0 lower from 1.

The equilibrium distribution coefficient, k_0, is defined as the ratio of the concentration of soluble components in the solid phase (CS) and the concentration of solute in the liquid phase (C_L) which is at equilibrium with a given solid phase:

$$k_0 = \frac{C_S}{C_L} \qquad (22)$$
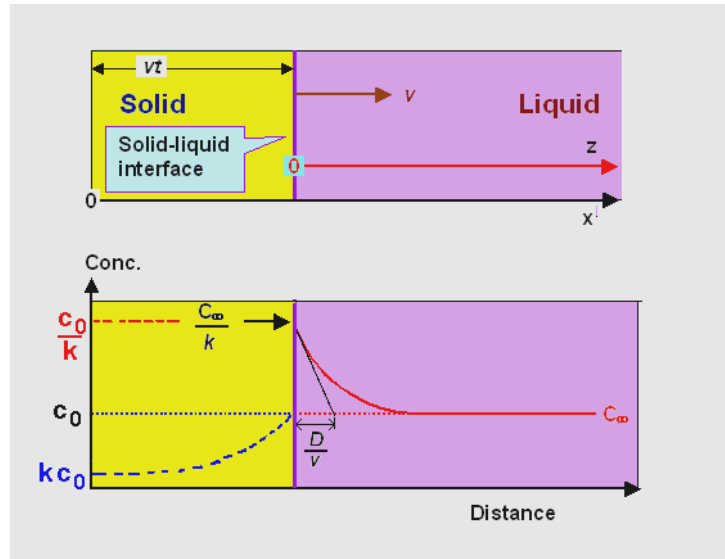
Figure 11. Temperature and concentration distribution.

When the liquid concentration of the soluble components C_0 cooled to a temperature T the first particles of the solid phase have a concentration of the soluble components k_0C_0. Excess soluble components $C_0(1-k_0)$ is secreted outside of the boundary surface, into the melt. Since there is not enough time for the soluble component diffuses into the mass of liquid will cause its accumulation along the boundary surface, and therefore comes to lowering the temperature of that part of fluid.

The actual temperature in the liquid phase in front of the boundary surface and the corresponding equilibrium liquidus temperature for the case of the absence of (a) and presence (b) accumulation of the soluble components. Initial thermal subcooling will be reduced due to the lowering of the equilibrium liquidus temperature, which is the result of changes in the composition of the liquid phase along the border area. Hence will slow down the growth of the solid phase.

The build-up (segregation) soluble components with the boundary surface is not uniformly, as is shown schematically in Figure 12. The local parts of the boundary surface (A) where the concentration of the soluble components of the lowest (and the reduction of subcooling), the faster it will grow and be allocated as bulges on the boundary surface.
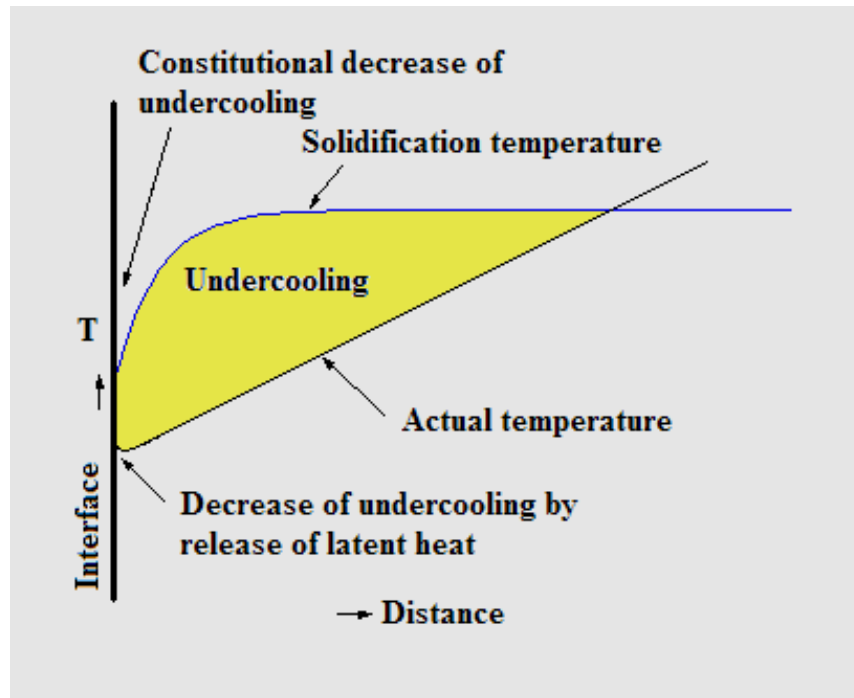
Figure 12. Distribution of real and liquidus temperature.

As previously mentioned, a decrease in hypothermia, in addition to constitutional, is also a result of the latent heat released, would chart the distribution of actual and liquidus temperature should be realistic that looks like Figure 12 [64].

As a result of constitutional downdraft occurs instability flat crystallization front by disturbances that occurred at the surface does not disappear but continue to grow in the direction of downdraft. That part of growing as a bulge until it reaches the part where balance is achieved due to a combination of gradient downdraft and develop their own latent heat, sufficient to provide a driving force for the cure. A convex shape of the projections ensures a stable temperature, which is above that of the plane front of crystallization and hence to lower the concentration of soluble components in the solid phase. Secreted soluble component accumulates on the sides and limits the growth projections in the lateral direction. In a similar manner the growth of the other surrounding the projections and their merged into densely packed cellular structure [63, 65-70].

It was noted that during the solidification of a binary alloy in the presence of a temperature gradient stop surface liquid-tight cell structure weight when growth parameters:

growth rate (R), a temperature gradient in the melt (G_L) and the initial concentration of the soluble components (C_0) in a controlled framework.

The first systematic study gave Chalmers et al [71, 72]. Dependence of morphology of the boundary surface of the liquid-solid growth parameters was tested using alloys based on lead. It was noted that a flat interface becomes unstable above the critical rate given by the expression:

$$R_{PC} = \frac{G_L D_L k_0}{m(1-k_0)C_0} \tag{23}$$

where D_L is the diffusion coefficient in the liquid phase, k_0 the equilibrium coefficient and m slope of the liquidus line at the appropriate equilibrium diagram.

With further increase of the growth rate comes to crossing structures in the dendritic cell. The exact transition when it becomes dendritic cell structure is not precisely defined. Some authors believe that this is the moment when the cell begins growth in the crystallographic directions, while some consider a transition into the dendritic structure only when it is clearly observed secondary branching. Although there is a large volume study of the growth of dendritic transition of one structure to another is not sufficiently understood. Development of microstructure depending on growth conditions (R, C_0) is shown in Figure 13.
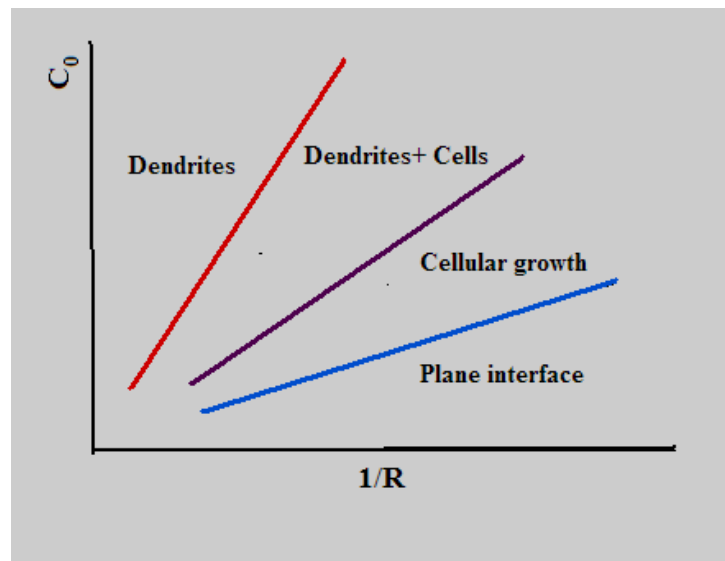
Figure 13. Dependence of the shape of the boundary surface of the conditions of growth.

Solute segregation during crystal growth

During crystal growth it is very important to predict the distribution of the concentration of soluble components deliberately add-dopant to achieve satisfactory mechanical, electronic or optical characteristics. Analysis of the distribution of the solute in the melt is relatively easily accessible while the connection with the distribution of components soluble in a solid phase (crystal) is used coefficient.

Distribution coefficient is defined as the ratio of the concentration of solute in the solid and liquid phase. At the interface, liquid-tight it is possible to define three distribution coefficients (Figure 14):
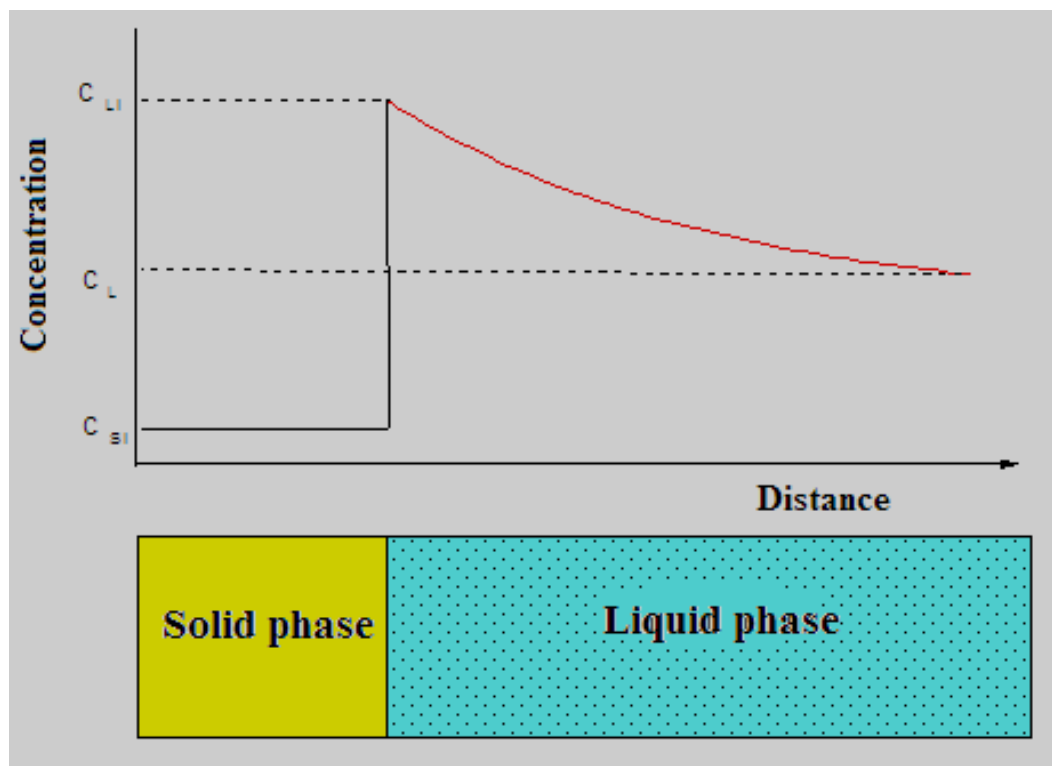
Figure 14. Solute distribution near interface.

where: C_{Si} - the concentration of solute in the solid phase with the boundary surface, and with the assumption of neglected diffusion in the solid phase, (as is justified because of the very small value of the diffusion coefficient), to minimize the concentration of soluble components in the whole of the solid phase; C_L - the concentration of solute in the weight of the melt; C_{Li} - concentration of solute in the melt with the boundary surface.

- The equilibrium coefficient - k_0 - in steady-state conditions (very slow growth rate)

$$k_0 = \frac{C_S}{C_L} \qquad (24)$$

The equilibrium distribution coefficient can be calculated from the equilibrium diagram for the solid solution as the ratio of the concentration of soluble components in the solid and the liquid phase which is in equilibrium with it. If there are areas of low concentration of the soluble components of the liquid solution slightly can be seen as an ideal solutions in which the change of the thermodynamic properties the same as in the case of ideal gases. In this case, the liquidus and solidus lines can be seen as the right. In the area of low concentration may be taken as a ratio of C_S/C_L constant, while at higher concentrations k_0 depends on the concentration.

In a case where the $k_0 < 1$ during solidification there is a build-up of soluble components in the liquid phase to the boundary surface; in the case where the $k_0 > 1$ comes to the impoverishment of the soluble component in the liquid phase with the boundary surface. Equilibrium value of the distribution coefficient can be taken into account for the reading and analysis of the curing process only at very low rates where the growth of the multiply assume that prevailing equilibrium conditions.

- The interphase coefficient - k_i:

$$k_i = \frac{C_{Si}}{C_{Li}} \qquad (25)$$

Since it is in practice very difficult to determine the concentration of soluble components in the solid phase with a boundary surface to define the real system;

- Effective distribution coefficient - k_e:

$$k_e = \frac{C_{Si}}{C_L} \qquad (26)$$

During solidification of the melt of the binary compound of the initial concentration C_0 composition originally resultant solid phase would be $k_0 C_0$ at equilibrium. Excess soluble

components are excreted in the melt continues to diffuse into the mass melt. During further cooling the solid phase and melt enriched soluble component. In actual cases, the crystal growth is present in the convection, because a low value of diffusion coefficient in the solid phase, it can be ignored. Temporal and spatial changes in the composition of the melt can be described by differential equation for conservation of mass:

$$\frac{\partial C}{\partial t} + R \nabla C = D_L \nabla^2 C \tag{27}$$

where: C - concentration of soluble components in the liquid phase, the growth rate - R, D_L - diffusion coefficient of the soluble components in the melt.

Burton, Prim and Slichter (BPS) [73] are performed the solution of this differential equation model, the so-called boundary diffusion layer. The effect of convective transport of the soluble components in the melt are solved dividing the melt into two parts: a part with a boundary surface where the thickness δ is assumed pure diffusion mass transport and part outside δ in the mass of the melt where it is assumed the complete homogenization of the liquid phase by convection (Figure 15). With the boundary conditions:

$$C = C_{Li} \qquad \text{for} \qquad x = 0$$

$$C = C_0 \qquad \text{for} \qquad x \geq \delta$$

$$C = C_{Si} \qquad \text{for} \qquad x < 0 \tag{28}$$

get solution:

$$\frac{C_{Li} - C_{Si}}{C_L - C_{Si}} = e^{\frac{-R\delta}{D_L}} \tag{29}$$

46

In addition to the foregoing definition of coefficients performed by the distribution of the effective dependency of the distribution coefficient of the growth conditions of the solid phase (so-called BPS-criteria):

$$k_e = \frac{k_i}{k_i + (1 - k_i)\, e^{\frac{-R\delta}{D_L}}} \qquad (30)$$

At low growth rate it is $k_0 = k_i$ [74] and after that:

$$k_e = \frac{k_0}{k_0 + (1 - k_0)\, e^{\frac{-R\delta}{D_L}}} \qquad (31)$$

In this way, it is possible to monitor the dependence of the distribution of the soluble components in the solid phase of the growth conditions of the solid phase- crystals.
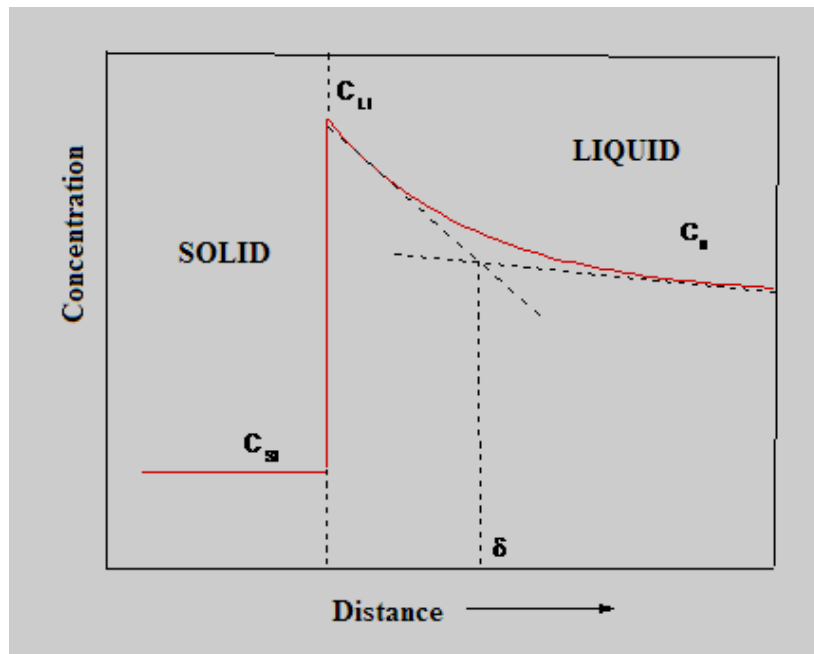
Figure 15. Solute distribution near interface.

During long-term tests of the process of crystal growth of the question arose of how the process parameters such as growth rate, temperature gradient, the initial composition of the alloy, the method and the intensity of stirring of the melt affect both the shape of the boundary surface [73] and the distribution of the soluble components. Namely, in recent years in the development and engineering requirements of the material observed dependence of material properties on the distribution of the soluble components (e.g., the mechanical properties of superalloys are dependent on the distribution of alloying elements).

When a distribution of the solute is considered, there are two different types-microsegregation (distribution of components soluble in the context of the dendrites or cell) and macrosegregation (distribution of components soluble long-range order).

As was previously said, the distribution of the solute may be monitored through the values of the effective coefficients of the distribution points, and hence, the influence of the conditions of crystal growth (growth rate, the initial concentration of the melt, convection) may be examined on the basis of the expression of BPS in dependence k_e of the conditions growth:

$$k_e = \frac{k_0}{k_0 + (1 - k_0) \ e^{\frac{-R\delta}{D_L}}}$$ (32)

With the increase in the growth rate changes and the value of k_e and k_0 value to 1, when practically no segregation soluble components. In case macrosegregation, this is the case for dendritic growth [72] while microsegregation within dendrites still present. The way to avoid microsegregation the growth of crystals with a flat abutment surface. For the dependence of the rate of growth will carried out several theoretical models that predict an abrupt change of the value of k_e in the vicinity of the rate D/a_0, where a_0 is the lattice parameter. If the rate of change will increase the rate is not great, the criterion for the instability of the border area to look for the CS criterion, the equation (32). In the area where the growth rate is large and sudden change points with the rate of orbital theory predicts the instability of the boundary surface.

From the foregoing, it is evident that the shape of the boundary surface and the distribution of the soluble components are closely linked and interdependent and should not

be considered as separate phenomena. On the one hand forms the boundary surface affects macrosegregation in the crystal, on the other hand itself segregation at the interface dictates the form and progress of border areas. In accordance with the characteristic attitude parameters of growth of crystal G/RC_0 it can be said that the increase of growth rate and the initial concentration of the melt, as well as reducing the temperature gradient leads to instabilities of the boundary surface to the dendritic structure, and the distribution of water-soluble components of the crystal growing without macrosegregation.

Melt crystal growth methods

For growing single crystals, many kinds of crystal growth methods have been developed for various materials such as metals, oxides and semiconductors. These various methods have been reviewed by several authors [75-93]. For most compound semiconductor materials, melt growth methods are the main methods of industrial manufacture. This is because they are appropriate to grow large single crystals quickly. In the case of solution growth methods and vapor phase growth methods, growth rates are rather lower compared to melt growth methods and they are in general limited to growing compound semiconductor materials which are difficult to grow by the melt growth method from the viewpoint of physical properties such as high melting temperature and/or high decomposition vapor pressure. In this section, melt growth methods which applied to compound semiconductor materials are reviewed.

The simplest method of forming crystals by melt–solid equilibrium is by uncontrolled freezing of a melt. In this process, the initial nucleation is random, and the resultant product is generally a fine-grained polycrystalline ingot.

Sometimes, however, single crystal grains of appreciable sizes can be identified in the solid matrix. When such large-sized grains are seen, one can infer that single crystal growth of that material can be achieved with relative ease.

In all the melt–solid growth techniques, the main effort is directed toward controlling nucleation so that a single nucleus (or at worst a few) will be formed first and act as a seed on which the growth will proceed. This is achieved by a process that is commonly known as directional solidification. Of course, use of a seed crystal simplifies the nucleation control.

All materials can be grown in single crystal form from the melt provided they melt congruently without decomposition at the melting point and do not undergo any phase transformation between the melting point and room temperature. Depending on the thermal characteristics, the following techniques are employed: 1. Bridgman technique; 2. Czochralski technique; 3. Zone melting technique; 4. Floating zone and 5. Verneuil technique.

Bridgman techniques

This technique was originally developed by Bridgman in 1925 to grow Single crystals of certain metals such as tungsten, antimony, and bismuth [87], and later the method was exploited by Stockbarger to grow large crystals of lithium fluoride [88, 89] and hence the name. However, in recent years, it is mainly called by the name of its original inventor. As with all the growth techniques, since the design of the growth apparatus is material specific, the basic technique has been modified by various workers depending on the specific conditions required to grow the chosen crystals.

The Bridgman technique (also referred to as the Bridgman-Stockbarger method) is one of the oldest techniques used for growing crystals [93]. Bridgman is used for single element growth and purification, and for binary (or ternary) semiconductor crystal growth of two (or three) group III/V elements. The crystal growth can be implemented in either a vertical (vertical Bridgman technique) or horizontal system configuration (horizontal Bridgman technique). Schematics of the two configurations are shown in Figures 16a) and16b). The growth systems typically consist of a single- or multi zone furnace. A single-zone furnace has a parabolic temperature profile with the highest temperature being at the center along the length of the furnace. On both sides of the hottest section, a temperature gradient exists that is used during the crystal growth. For a multizone furnace, specific temperature gradients between different zones can be established.

The principle of crystal growth using Bridgman technique is based on directional solidification by translating a molten charge (melt) from the hot to the cold zone of the furnace.

Due to the special geometry of the court after only one crystallization crystal continues to grow. Boundary surface liquid-tight is completely surrounded and in contact with the court so that the released latent heat must be discharged by conduction through the walls of the court or through the crystal. The advantage of this method is its simplicity and the possibility of variation. It is also easy to control the vapor pressure of volatile components; it is possible to carry out growth in vacuum and sealed container. Easily gets hungry shape and size of the crystals. In addition, growth can be performed using relatively

well stabilized by the temperature gradient which at the same time stabilizes the convective mixing and segregation. The limitations of this method lie primarily in growing crystals expand during crystallization, since the generation of defects in the crystal. In addition, it is impossible to predict not get the desired crystal orientation.

a)

b)
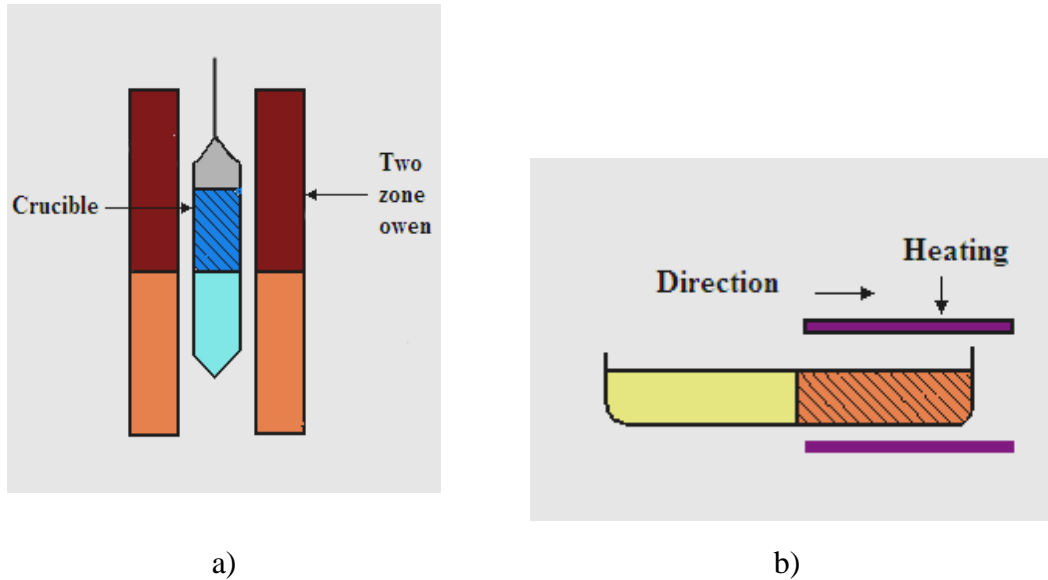
Figure 16. Schematic diagram of b) vertical Bridgman (VB) in a two-zone furnace and b) horizontal Bridgman (HB) crystal growth process in a single-zone furnace.

The presence of a seed at the end of the crucible (container) ensures single-crystal growth in specific crystallographic orientation. Using the single crystal seed; the entire growth process takes place in the following sequence. At the beginning of the experiment, the crucible with the polycrystalline charge and seed is placed inside the growth chamber.

Czochralski method

In this method of crystal growth [94] also the entire batch is melted in a vessel (Figure 17). Seed crystal descends vertical support (with the possibility of rotation) to the surface of the melt and the time of contact, and then is allowed to reach thermal equilibrium. The temperature of the melt is adjusted so that the part of the seed crystal melts, then the

temperature is slowly reduced until the call begins to crystallize. Then begins slowly drawing calls. Crystal diameter is controlled by adjusting the feed rate, the rate of rotation and temperature control of the melt. The characteristic of this method is that, although the court is used for crystal growth, no contact boundary surface of the liquid-tight with the court. In it lies one of the major advantages of this method, namely the possibility of crystal growth with an increase in volume, as well as semiconductors [95]. It is also possible to obtain crystals of good quality (no dislocation), large diameter and with high-rate growth. In addition, this method is suitable for the respective control of doping and chemical analysis of the components. Finally, it allows for control and good atmosphere during crystal growth. A limitation of this method lies in the difficulty in the growth of crystals with the components that have a high vapor pressure at the melting temperature. It is necessary to maintain constant pressure, which complicates the system configuration. In addition, this method is not sufficiently adapted for continuous growth. Also there is the problem of choice vessel to melt and the possibility of contamination of the melt.
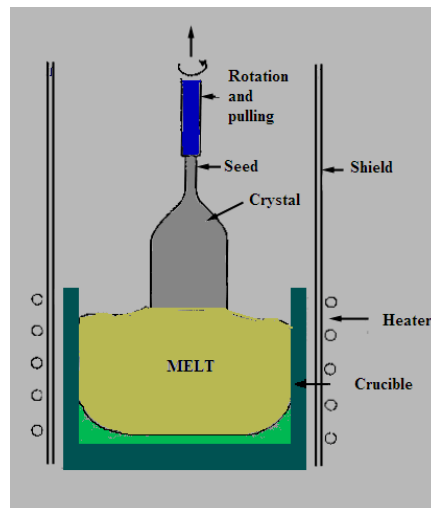
Figure 17. Czochralski crystal growth.

Zone melting – refining

The molten zone (Figure 18) of finite thickness (which is a lot less than the length of the crystal) moves from one end of the batch to another. This method is often used for the treatment of materials, a better effect is achieved by multiple passes through the charge zone. You may exercise control incorporating soluble components.

53

a)   b)
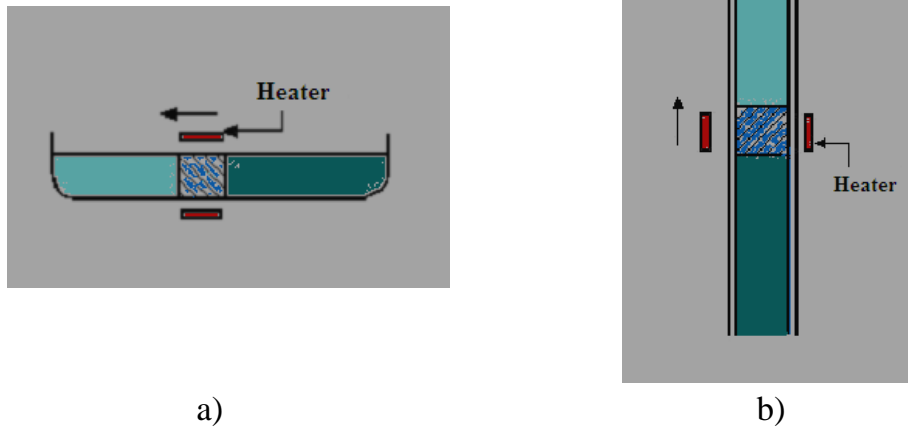
Figure 18. a) Horizontal and b) vertical configuration of zonal melting - rafining.

Floating zone method

In a vertical configuration avoids the use of the court and only a part (zone) melted and maintained on the basis of surface tension. It is suitable for materials with high surface tension of the melt and low density (Figure 19). Utilized the advantage zonal melting - treatment and control of the incorporation of soluble components, and avoided the contamination of the melt court [89, 90]. A limitation of this method is that it can not be used for materials with low surface tension, and for those with volatile components. This method also has several modifications of laser melting zone, use calls, etc.
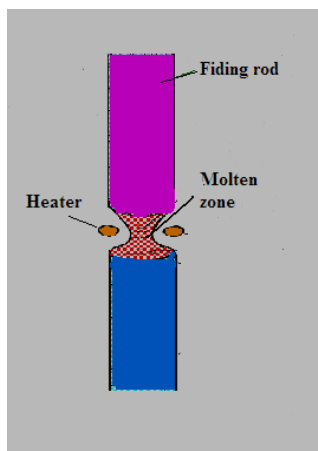
Figure 19. Floating zone method.

Verneuil method

The methods of crystal growth without crucible should also be mention is Verneuil method. From dozer dust material that hardens falling through the flames and molten arrives on the surface of crystal growth (Figure 20). As the crystal grows, it drops down proportional to the rate of arrival of the melt. Rotation of the crystal used for homogenization. Due to the difficulty in controlling the parameters of this method is rarely used, despite the benefits of the growing crystal without trial.
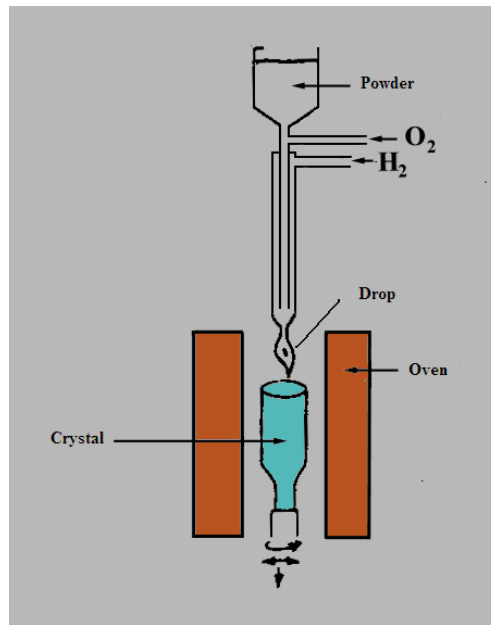
Figure 20. Verneuil method.

Vertical Bridgman method - features and benefits

For a long time the Bridgman technique used only for the growth of crystals in the laboratory. In fact, many problems such as contamination and contact with the court and fluid flow problems have limited its use. Methods of crystal growth by the Czochralski (CZ) is definitely have an advantage in the preparation of large diameter crystals in the industrial production. With the advent of large demands regarding the use of semiconductor materials, the perfection of the crystals must be controlled at the submicron level. CZ method has an inherent constraints such as the rotational asymmetry of the thermal field which affects the occurrence of rotating stretch marks, and a high temperature gradient in the crystal may cause thermal stresses and occurrence of dislocations. Regardless in mind the application of magnetic fields, encapsulation techniques and the application of "hot wall", there was a need to consider other methods, such as Bridgman, to overcome these problems [96]. Excellent results have been achieved in obtaining the crystals of GaAs and InP large diameter, the vertical Bridgman method [97] have shown great potential of this technique. Therefore, it is necessary to analyze and optimize the process parameters of crystal growth in a Bridgman configuration. As a first task there was a need to examine the influence of growth conditions on the quality of the resulting crystals.

The interface shape and the solute distribution in vertical Bridgman method

There are many variations in the design of the apparatus Bridgman method [98, 99], but the basic design is the same. The heat supply and the melting of the charge takes place in the part of the furnace for heating, then the vessel containing molten move at a constant rate through the field of furnaces of a certain temperature gradient, wherein there is less heat loss in a radial direction, while the main part of the released heat is removed in the axial direction.

Therefore, there is a cooling of the melt and at one point the melt temperature reaches a curing temperature and comes to the boundary surface of the forming liquid-tight. It is usually assumed that the stop surface remains stationary in relation to the furnace in the vicinity of the point that corresponds to the curing temperature. This means that the sample

moves at a certain rate R, which is generally assumed to be equal to the rate of movement of the court. However, there is a possibility that these two different rates and in the quasi-steady-state border area migrate within the furnace. This phenomenon is also studied, but was not observed a clear regularity, which would describe a deviation from expected rates under given conditions.

As for the shape of the boundary surface, it is, in accordance with the general criteria, at low rates the growth of a flat and perpendicular to the axial axis of the furnace. With an increase in the growth rate there is a disturbance of the boundary surface and the transition to the cell, and then dendritic growth. The influence of the initial concentration of soluble components, C_0, is reflected in the fact that an increase in the areas of critical C_0 moving rate change of the form of the boundary surface towards lower temperature. The influence of growth conditions on the shape of the boundary surface still best describes the parameter $GL\,/\,RC_0$ whose reduction below a critical value leads to a disruption of border areas, cellular and dendritic growth.

The simplest description, depending on the distribution of the soluble components of the conditions for crystal growth based on a model of the equilibrium solidification, where it is assumed that the process is very low rate and the presence of and diffusion in the liquid and in the solid phase. In practice, it is more applicable description based on nonequilibrium lever rule, so-called. Scheil's model [100] that describes the concentration of soluble components in the solid phase as a function of the work hardened fractions according to the equation:

$$C_S^* = k_0 C_0 (1-g)^{k_0 - 1} \tag{33}$$

where: C_S^* concentration of the soluble components which is consistent with the volume fraction (fraction) of the solid phase relative to the total volume of the charge - g, C_0 is the initial concentration of the soluble components in the melt, k_0 equilibrium distribution coefficient.

Calcium fuoride single crystal

Fluorides have attracted considerable research interest because they exhibit many unique properties that may increase their applications in optics and electronics. Among them, alkaline-earth fluorides are dielectric and have a wide transmission range, and therefore they are widely used in optical components, microelectronic and optoelectronic devices [101-103]. CaF_2 is a kind of typical alkaline-earth fluorides. It has a well-known fluorite structure, in which Ca^{2+} ions lie at the nodes in a face-centered lattice, while F^- ions lie at the centers of the octants [104]. Furthermore, with an optically isotropic fluorite structure, the CaF_2 crystal is suitable as a phosphor host because it exhibits outstanding transmission characteristics for a wide range of wavelength (0.3-8 mm) [105]. When CaF_2 is doped with rare-earth (RE), some interesting luminescence properties can be expected. As a result, general attention has been drawn on this field recently. CaF_2 doped with RE could be used as laser [106, 107] and fluorescent labeling material in biological applications [108-110].

Also, CaF_2 crystals exhibit some excellent properties such as high transmittance in the far UV to mid IR range, low refractive index, high chemical resistance and high laser damage threshold. These properties make this crystal an important optical medium material and have been used as an important lens material for photolithographic applications [111, 112].

Generally CaF_2 single crystals are grown by Bridgman method and the applications require large diameter CaF_2 single crystals [113, 114]. But growing large size single crystals have been very tough because of the grain boundaries during the growth and the cracks during the cooling process [115]. Recently ceramic laser technology are found to exhibit - more advantages over the single crystal growth processes and in particular, the ceramics can be produced in large volumes and with the homogeneous doping of laser active ions in the host materials [116]. Polycrystalline CaF_2 has been synthesized for the first time with dysprosium as an active ion [117]. Recently, thermal conductivity of the natural calcium fluoride ceramics has been investigated and compared with single crystals of CaF_2 and are found to exhibit better mechanical properties over single crystals [118]. Also, it was confirmed that the grain boundaries are transparent to phonons as well as to photons in synthetic optical ceramics of CaF_2.

Calcium fluoride or fluorite is a well-known face-centered cubic mineral [119]. The fluorite structure is shared with a wide variety of other compounds, for which CaF_2 is considered the type compound. The structure of fluorite has eight fluorine atoms arranged in a cube around the calcium atom, with the cubes of fluorine edge-connected in a face-centered cubic array. Conversely, the fluorine atom is surrounded by four calcium atoms arranged in an ideal tetrahedron, with the tetrahedra also edge-connected. Fluorite has a very simple structure (Figure 21).
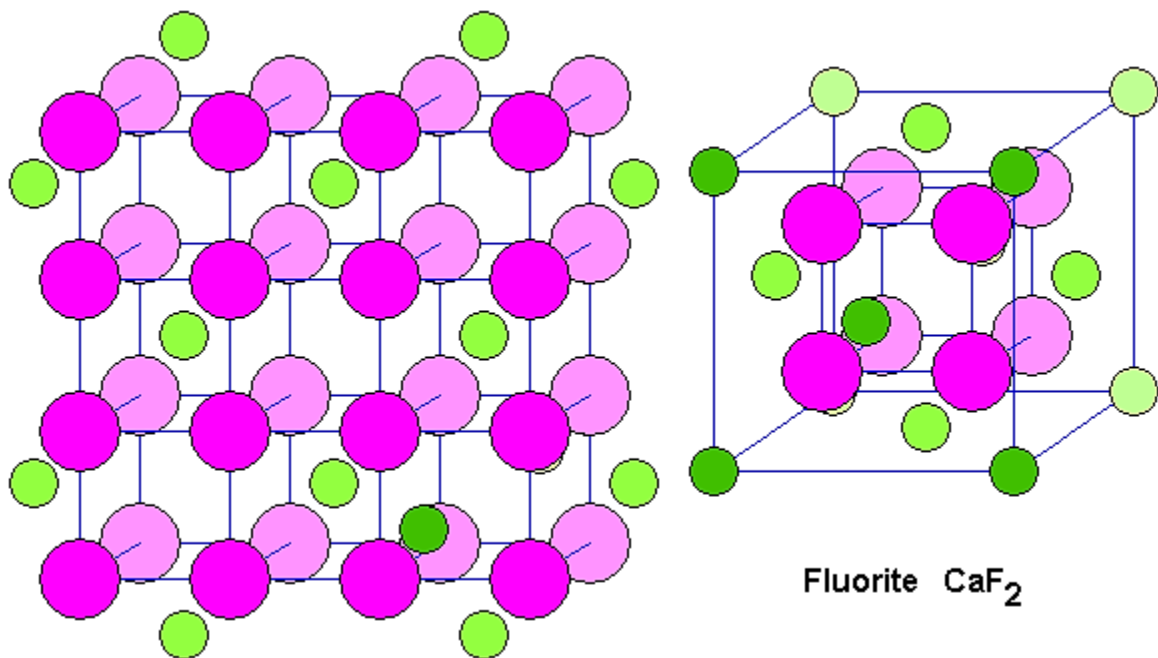
Figure 21. Calcium fuoride crystal structure.

Calcium (green) atoms in a face-centered pattern contain a cube of fluorine atoms (purple). Darker shades are used to portray calcium atoms toward the rear of the unit cell. We can also view the structure as a simple cubic array of fluorine atoms with a calcium atom in the center of alternate cubes. Considered that way, there are obviously diagonal planes of cubes containing no cations. These planes will obviously be planes of weakness, accounting for fluorite's excellent octahedral cleavage.

Polymer composites with single crystals

Recently, polymers are finding an important place in different research laboratories for the study of their various properties. Many polymers have been proved suitable matrices in the development of composite structures due to their ease production and processing, good adhesion with reinforcing elements, resistance to corrosive environment, light weight, and in some cases ductile mechanical performance. Single crystals have been widely studied due to their unique structural, electronic and spectroscopic properties, which may be exploited for their diverse applications in chemistry, biology, and nanoscience. Lately interest of researchers engaged in different fields of knowledge is seen to be focused on determination of the action of single crystal particles addition,on properties of polymers and their compositions. Incorporation of single crystal particles into chemical composition of polymers gives one more opportunities for their study and application as composite materials, films, and fibers serving different purposes [120]. Also, the research of polymer material has been directed to blend or copolymer of different polymers to obtain new products having some of the desired properties of each component.

PMMA (polymethyl methacrylate) (Figure 22) and its derivatives are known for their optical applications [121-125]. The aim of this dissertation concerns on studying the change in the optical absorption, the optical parameters and photoluminescence spectra for the samples of single crystal particles polymer composites which are recorded at room temperature. In addition, X-ray diffraction (XRD) and scanning electron microscope (SEM) are used to characterize the these nanocomposites.

Hybrid polymer composites, both organic-organic and organic-inorganic are candidate materials for high density storage. The essential elements for a polymer to be photorefractive are − sensitizer, photoconductor, chromophore and plasticizer. These agents are incorporated into the polymers by adopting various approaches to engineer the desired functionality. One of the important compositions for photorefractive applications is 40-60 wt% of photoconductor or semiconductors (like PVK, PSX, BSO, BGO, CaF_2), 25-35 wt% of chromophore (like dyes, liquid crystals) 15-30 wt% of a plasticizer (like ECZ, BBP) and about 1 % of sensitizer. Among the organic-inorganics, about 1% of gold nanoparticles added to PVK, DCVDEA and TNF, and other similar compositions are of interest in data storage. In

photopolymers the monomers are polymerized on exposure to light resulting in local change in density. This causes a diffusion of the binder, a chemically inactive component with specific optical properties, to regions of low intensity. These density variations in polymer matrix result into a refractive index grating and the information is stored and retrieved through the processes mentioned earlier. In organic-inorganic nanoparticle photopolymer composites, the inhomogeneous illumination results in an index grating due to a difference in refractive indices of periodically distributed inorganic nanoparticles and uniformly distributed polymerized monomers.
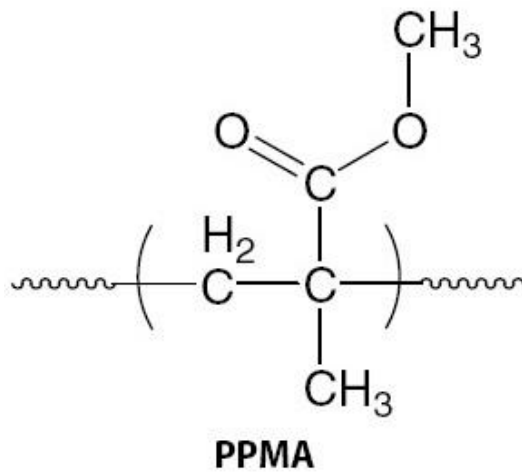
Figure 22. Structural formula of polymethyl methacrylate (PMMA).

Characterization of single crystal and polymer nanocomposites

Various experimental techniques have been utilized to characterize single crystal and polymer nanocomposites behavior.

X-ray diffraction (XRD)

XRD is an important analytical technique for the characterization of intercalation and exfoliation in composites comprising polymer and layered materials. XRD can accurately measure the interlayer or basal plane d-spacing of single crystals and its composites. X-ray diffraction is a nondestructive technique, and is one of the widely used for determining lattice parameters, preferred orientation of the crystal, phase composition (qualitatively and quantitatively), grain sizes, lattice strain, residual stress etc. XRD can provide the information from a relative lager area of the specimen compared to TEM.

When a monochromatic X-ray beam incident onto a crystal sample, the constructive diffractions (or interference) from parallel planes of atoms with inter-planar spacing, d occur if Bragg's law is satisfied (Figure 23) [131]:

$$2d\sin\theta = n\lambda \qquad (34)$$

where n is integer that indicates the order of the reflection, θ is Bragg angle, and λ is the wave length of the X-ray beam. By measuring the Bragg angle θ, the interplanar distant d can be obtained if the wavelength of the X-ray beam is known.
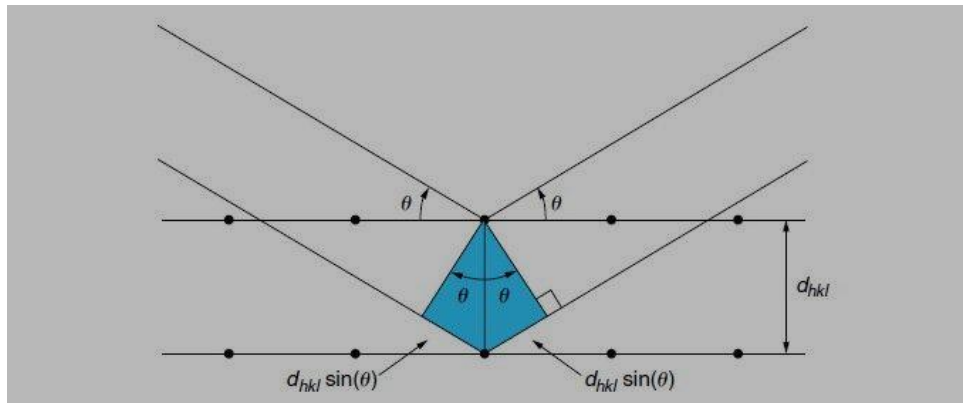
Figure 23. Schematic diagram of Brag′s diffraction from a set of parallel planes.

When X-ray light reflects on any crystal, it leads to form many diffraction patterns and the patterns reflect the physico-chemical characteristics of the crystal structures. In powder specimen, diffracted beams are typically come from the sample that reflects its structural physico-chemical features. Thus XRD technique can analyze structural features with other ambiguities of a wide range of materials such as inorganic catalysts, superconductors, biomolecules, glasses, polymers and so on.

On the other hand, the first treatment of particle size broadening was done by Scherrer. By making some simplifications, e.g., taking a powder sample of a small cubic crystal, and assuming they are free from strains and faulting, so that the peak broadening is due only to the small size, the following Scherer's equation [132]

$$D = K\lambda \ / \ Bcos\theta \qquad (35)$$

where D is the particle diameter, θ is the diffraction angle, and B is the full width at the half high maximum (FWHM). The factor K involves different instrumental aspects, such as geometry, penetration of X-Ray in the sample, etc. From the width of the diffraction peak using the Scherrer's equation, one can calculate the average particle size. However, the width of diffraction peaks is broadening due to presence of defects or strain in the crystal lattice. The extreme case corresponds to amorphous materials, for which the peaks disappear totally. In nanostructured materials, the Scherrer's equation provides an estimated value of the crystal size.

Nanoindentation

Nanoindentation was used as another approach to gather comparative elastic modulus and hardness data for the six systems. The basic concept of indentation testing involves touching a material whose mechanical properties are of interest with a material whose properties are known. Nanoindentation is a specialized indentation test in which the penetration distance is measured in nanometers. Because the sample surface area and depth requirements are so small, thin film samples are appropriate for this type of testing. One of the key factors in analyzing indentation data is the contact area between the indenter and specimen. In typical indentation testing the area of contact is simply calculated from measurements of the residual impression left on the specimen. With nanoindentation,

however, the area is on the order of microns and is too small to measure accurately [133-135]. Instead, the depth of penetration into the specimen surface is measured and combined with the known geometry of the indenter to calculate the contact area. The load displacement data gathered during the indentation process, shown in Figure 24, provides the means to calculate modulus and hardness. For each loading /hold /unloading cycle, the applied load value was plotted with respect to the corresponding position of the indenter. The resulting load/displacement curves provide data specific to the mechanical nature of the material under examination.

The maximum indenter depth achieved for a particular load and the slope of the unloading curve measured at the tangent to the data point at maximum load is used to calculate hardness and modulus following the method developed by Oliver and Pharr [126]. Under indentation loading, creep within a specimen can occur and results in a change of indentation depth with a constant test force applied. It is indistinguishable from thermal drift so one must interpret results accordingly. Several studies performing nanoindentation on polymers, including specifically PS and PMMA, have shown larger modulus values than reported by tensile testing or DMA on the same materials [129].

The values of modulus tend to increase with indentation depth. Although the values might be larger than other characterization techniques, this study assumes nanoindentation can provide sound comparative data as all six systems in this study were analyzed using the same parameters. Unlike DMA and nanoindentation is generally considered a non-destructive technique [129]. The American Society for Testing and Materials (ASTM) Task Group E28.06.11 is developing a standard test method for indentation testing.
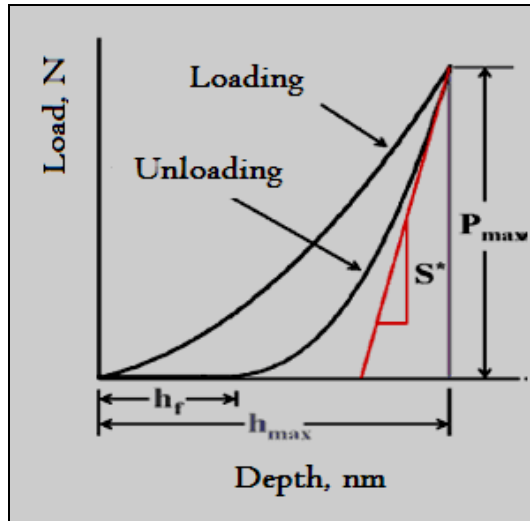
Figure 24. Typical loading-unloading curve of a nano-indentation test. P_{max} and h_{max} are the maximum load and displacement, respectively. S^* is the slope of the tangent to the maximum load on the unloading curve [129].

Fourier transform infrared spectroscopy

Fourier transform infrared spectroscopy (FT-IR) was used to analyze the bonding between the polymer matrix and nanoparticles. FT-IR measures the absorption of infrared radiation by the sample material with respect to the wavelength of the radiation. Using absorption data, one may identify molecular components and structures. The signal detected is analyzed using Fourier transforms to provide infrared absorption spectra, usually presented as plots of intensity versus wavenumber in cm^{-1}. Infrared wavelengths absorbed by a material identify its molecular structure. The absorption spectrum is most often compared against a spectrum from a known material for identification. Absorption bands in the range of 4000-1500 wavenumbers are typically due to functional groups such as –OH, C==O, N—H, and –CH$_2$. The range from 1500-400 is referred to as the fingerprint region and generally caused by intra-molecular phenomena very specific to each material [132, 133].

Koenig et al. have extensively researched polymer dissolution with FT-IR imaging [134-143]. By coupling a step-scan interferometer with an FT-IR spectrometer and a focal

plane array (FPA) detector, spatial and spectral information may be collected simultaneously (Figure 25). The ability of FT-IR to measure the behavior of multiple components within a system simultaneously, when coupled with the spatial resolution of an FPA provides a unique opportunity for observing the dissolution process. With this experimental setup, the behavior of multiple components diffusing into a polymer matrix may be observed.
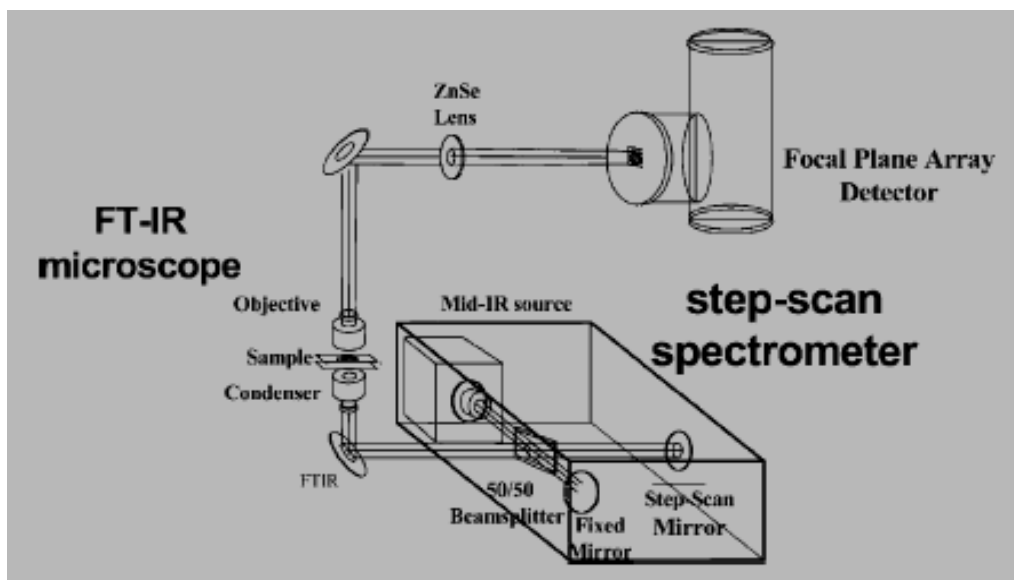
Figure 25. Schematic of FT-IR imaging set-up.

The behavior of binary solutions diffusing into a polymer has been characterized [135-138, 140-142]. A single experiment yields data on all components in the system, allowing for real-time analysis of both the dissolution process and the behavior of each component within the system. To measure dissolution, a spectral profile may be taken across the sample, noting the intensity of polymer- or solvent-specific bands across the interface. From these profiles, the behavior of the system may be characterized quickly and easily. The spatial resolution of these images is about 6 mm. Because no apertures are used, the diffraction effects that usually affect resolution do not come into play using this method.

Raman spectroscopy

When light is scattered from a molecule or crystal, most photons are elastically scattered. The scattered photons have the same energy (frequency) and, therefore, wavelength, as the incident photons. Raman scattering can occur with a change in vibration, rotational or electronic energy of a molecule. If the scattering is elastic, the process is called Rayleigh scattering. If it's not elastic, the process is called Raman scattering [143]. In quantum mechanics the scattering is described as an excitation to a virtual state lower in energy than a real electronic transition with nearly coincident de-excitation and a change in vibration energy.
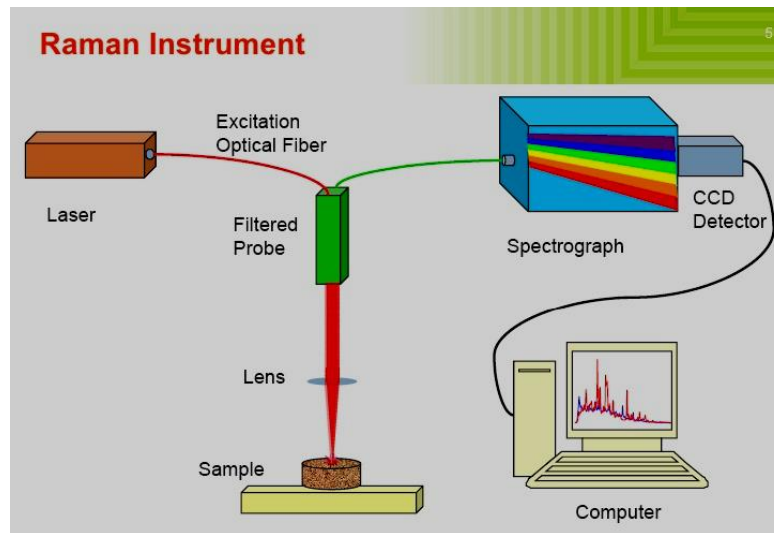
Figure 26. Schematic of Raman experiments.

Differential scaning calorimetry - DSC

Differential scanning calorimetry is a method of testing each thermal properties of substances based on differences heat flow to the sample and to the standard of during their simultaneous warming. As for the data on the temperatures at which begin and end the processes followed by a change of enthalpy, DTA and DSC methods are equivalent. However DSC method is much more convenient and accurate for quantitative determination of enthalpy changes because of its technical solutions tailored primarily to the task.

The essential parts of the device for the DSC are two cells with the identical slots for the sample and standard with appropriate thermocouples attached in opposition, oven with the stove controller, amplifier EMS thermocouple and recorder of the DSC curves (Figure 27).

The temperature difference between the sample and the standard obtained when the sample process begins by changes in enthalpy. Lagging temperature of the sample compared to the standard (due to the endothermic process) increases the heat flux to the sample; precedence (due to the exothermic process) is reduced. In Figure 27 sis presented the DSC curve in general. Change of heat capacity during heating to maintain the drift of the base line, and the exothermic and endothermic processes as peaks at corresponding side of the base line.
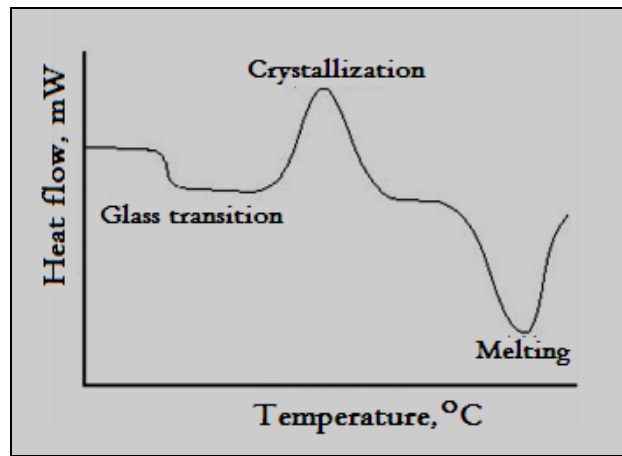
Figure 27. DSC curve.

Scanning electron microscopy (SEM)

Scanning electron microscope (SEM) is a very important instrument that gives a high resolution image of the sample surface. Schematic of a typical SEM is shown in Figure 28. The electrons are emitted from thermal cathodes of tungsten and accelerate toward the anode. Tungsten has the highest melting point and the lowest vapor pressure of all the metals and therefore can be heated sufficiently to emit electrons. Electron beam carries a power ranging from a few hundred up to 100 keV. Beam is focused with the condensing lens in the two one site of 1 to 5 nm. Beam passes through the pairs of scanning lens in the lens of the thread which causes it to be cleared for the stack horizontally and vertically in order to scan more

quickly formed in the shape of a rectangle on the surface of the sample. When the primary electron beam contact with the sample, electrons lose energy due to scattering and absorption of the constant in a certain volume of the sample (the so-called volume of interaction) that extends less than 100 nm and up to about 5 μm from the surface of the sample. The energy exchange between the electron beam and the sample causes the emission of secondary electrons, electromagnetic radiation that can be detected, carried forward and used to obtain images. Black and white image of the sample is obtained by combining sample scans with the received signal.
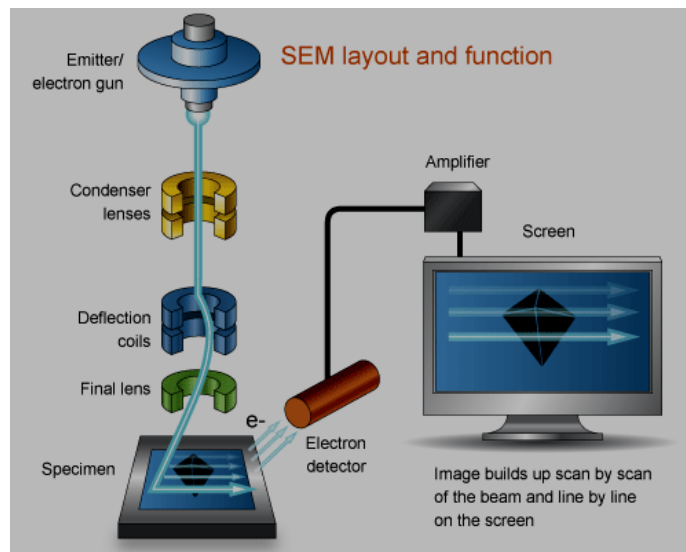
Figure 248. SEM layout and function [144].

Time resolved laser induced fluorescence measurements

Time resolved laser induced fluorescence measurements (TRLIF) is a very sensitive and selective method for ultra trace analysis in the different fields of nuclear, environmental, and medical science. This technique is based on laser excitation followed by temporal resolution of the fluorescence signal. The other great advantage of TRLIF is its triple resolution: (1) excitation resolution by the proper choice of the laser wavelength (N2, tripled or quadrupled Nd:YAG, dye, (2) emission fluorescence, which gives characteristic spectra of the fluorescent cation (free or complexed); and (3) fluorescence lifetime, which is characteristic of its environment (complexation, quenching). These two latter types of data

provide useful information on the chemical species present in solution as well as for complexation studies. For example, this technique used as a fluorescent titration method' has allowed the determination of complex formation at a low level between trivalent elements [145]. Excitation part of the system is based on nanosecond Nd:YAG laser and Optical Parametric Oscillator (OPO). The fluorescence detection part of our system is based on picoseconds streak camera. The laser is more than powerful enough (365 mJ at 1064 nm, variable OPO output >5 mJ) for LIBS, but somehow slow (the length of fundamental laser harmonic output pulse is about 5 ns) for fluorescence measurements in our present area of interest, namely plants and food products. Fortunately, the pulse length of tunable OPO output (320-475 nm) is less than 1 ns, so by means of a correct deconvolution procedure it is possible to measure the fluorescence lifetimes in the range as small as a few nanoseconds [146].
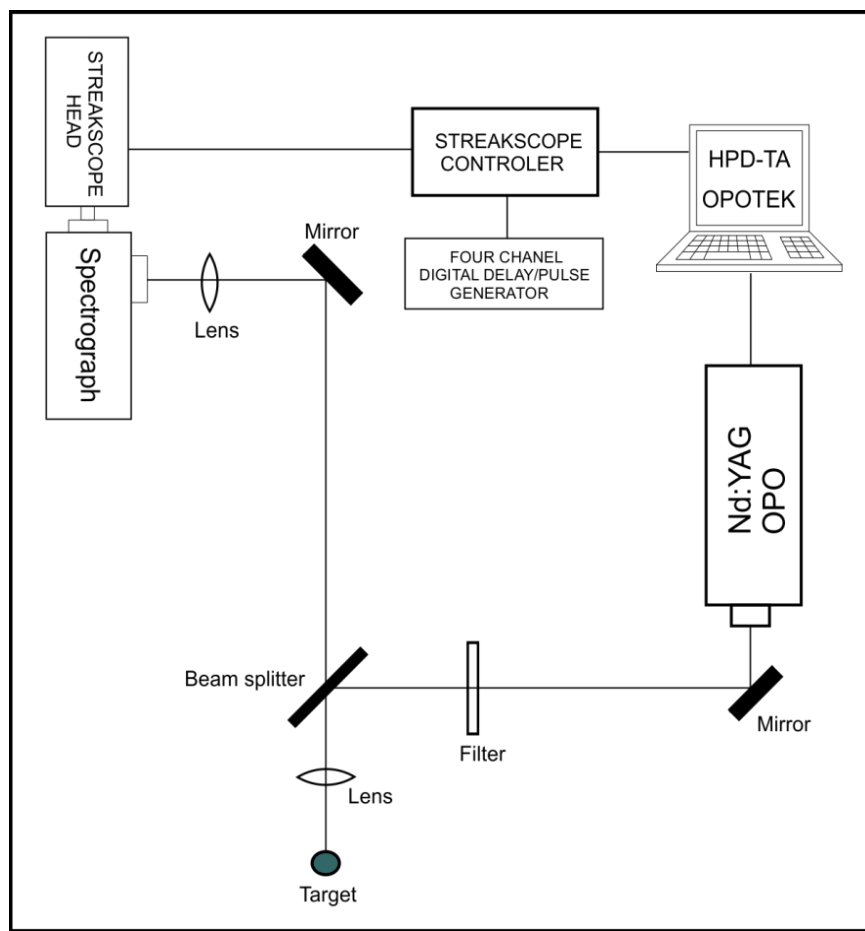
Figure 29. Schematic illustration of experimental setup for TR-LIF spectroscopy [146].

The experimental set-up consists of excitation and detection part (Figure 29). Pulsed excitation was provided by a tunable Nd-YAG laser system (Vibrant model 266 made by Opotek, Inc.). This system incorporates the Optical Parametric Oscillator (OPO) that is pumped by the fourth harmonics of the laser at 266 nm. The laser induced fluorescence in the samples is recorded using streak scope (Hamamatsu model C4334-01) with integrated video streak camera.

EXPERIMENTAL PART

Materials

Powder CaF_2 (*Rare Earth Products Limited*) purity of 99.99% was used in the single crystal growth. Commercially available PMMA Acryrex® CM205 (Chi Mei Corp. Korea, (Mw≈90400 g/mol, n = 1.49, λ = 633 nm) pellets were used as a polymer matrix for preparing composite films. The quantum dots of cadmium selenide (CdSe) nanoparticles, were supplied from QD particles, Future Chemistry, Netherland, 610nm, a solution in toluene. Dimethylformamide (DMF, anhydrous, 99.8%, Sigma-Aldrich) and acetone (Zorka Pharma, Serbia) were used as solvent for preparation of composite films by solution casting.

Experimental procedures

Crystal growth

The Bridgman method of crystal growth is relatively simple and allows operation in a vacuum, and also in an inert atmosphere. In this method, the crucible uses a cylindrical shape with a conical bottom. The procedure consisted of the following: the crucible cylindrical shape with melted batch CaF_2 down from the upper hot chamber of the furnace in the cooler lower chamber of the same furnace. The bottom of the crucible was in the shape of a cone and that in the formation of germs and begins the process of crystallization. The crucible was from spectroscopically pure graphite [147-153]. One of the main drawback of this method is that in the course of growth can be seen the process of crystal growth, so that if it comes to the appearance of polycrystalline, this can be concluded only after the completion of the process of growth and cooling crystals.

To obtain single crystals of CaF_2 by the Bridgman method in a vacuum has been used device BCG 356. Initial samples of single crystals were mostly transparent, but some were cracked. Because of the small temperature gradient there were a sudden crystallization process and the appearance of dendrites in the lower part of the crucible, and therefore made changes to the structure of the crucible. Therefore, we had to make some changes in conditions of growth and construction of crucible. With this change we have achieved that

cone of the lower part of the crucible is in the form of a tube. Therefore we have achieved that by the sudden crystallization takes an extended part of the crucible, thus avoiding the occurrence of dendrites. The crystals that were obtained on the crucible constructed in this way were of better quality. However, when grinding the upper surface of the crystal, because the dirt that clung to that, there have been cracks crystal along a plane of cleavage.

Experiments have been performed with CaF_2 in the form of a powder. Since this device works in a vacuum, there was a danger that the air contained in the powder CaF_2, when you turn on the vacuum pump, disperses the powder throughout the apparatus. Therefore, the CaF_2 powder was compacted and sintered in the form of pills. With such obtained pills could easily and quickly be filled crucible. Powder CaF_2 (*Rare Earth Products Limited*) purity of 99.99% was used in the experiment. CaF_2 powder was compacted under a pressure of 3500 kg cm^{-2}, and the sintering of the obtained tablet was carried out at 900 °C under an inert atmosphere of argon. We tried out combinations of various growth rates and generator powers with the aim to define the optimal growth conditions.

Power generator was initially $P_{gen} = 3.8$ kW, and was later increased to $P_{gen} = 3.94$ kW. The crystal growth rates were 6 mm h^{-1}, 12 mm h^{-1}, 24 mm h^{-1} and 48 mm h^{-1}.

Crucible with the charge placed on the holder in the upper chamber furnace. Then the apparatus is sealed, and then put into operation a vacuum apparatus and cooling water. By establishing a vacuum inaugurated generator that is done gradually warming to melt the batch. The power generator is a maximum of 30 kW. When melting the batch used power generators of 3.64 kW. Since the charge melted, the crucible is dissolved slowly by hand down to the bottom (cold) chamber furnace. At the top of the cone, which comes first in a cooler area, creates a germ that begins with the crystallization. Continued further lowering the crucible, and the power supply generators have been gradually decreasing.

When lowered muffle up to 30 mm in length, the descent rate was $R = 6.8$ mm h^{-1}. In a further descent we increased the speed at $R = 12.7$ mm h^{-1}. In subsequent experiments, we used only the rate of descent crucible of $R = 6.8$ mm h^{-1} over the entire length of the crucible. In growing single crystals used a modified holder when casting. With him are the cooling fins slightly higher at the upper end than the lower, while in normal bracket when casting the

cooling fins of the same size. In Figure 30 shows a schematic representation of the apparatus, and Figure 31 gives the look and dimensions of crucible that was used during the experiment.
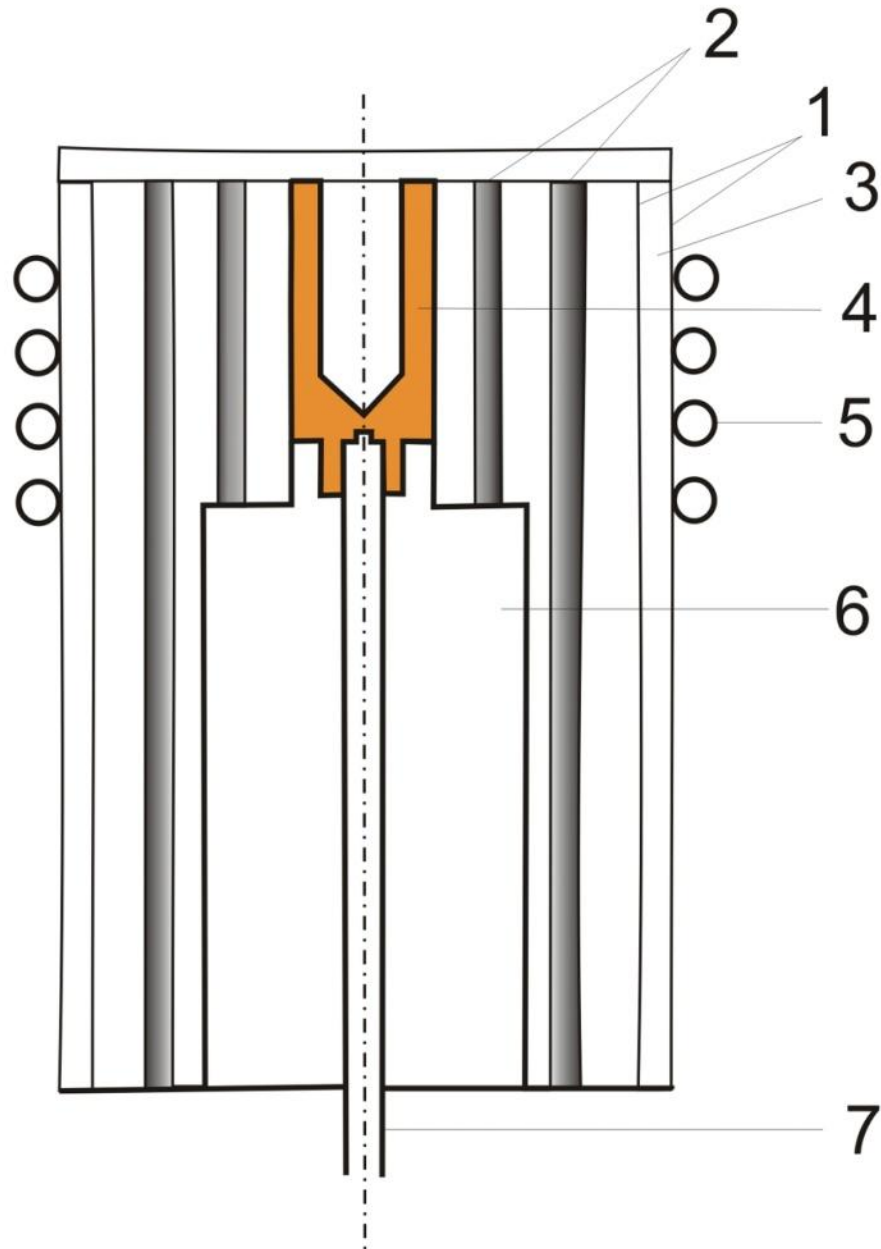
Figure 30. A schematic view of an apparatus for Bridgman-grown CaF$_2$ single crystals: 1) quartz tube; 2) ceramics; 3) line for cooling; 4) graphite crucible; 5) spiral for heating; 6) graphite crucible carrier and 7) spindle.
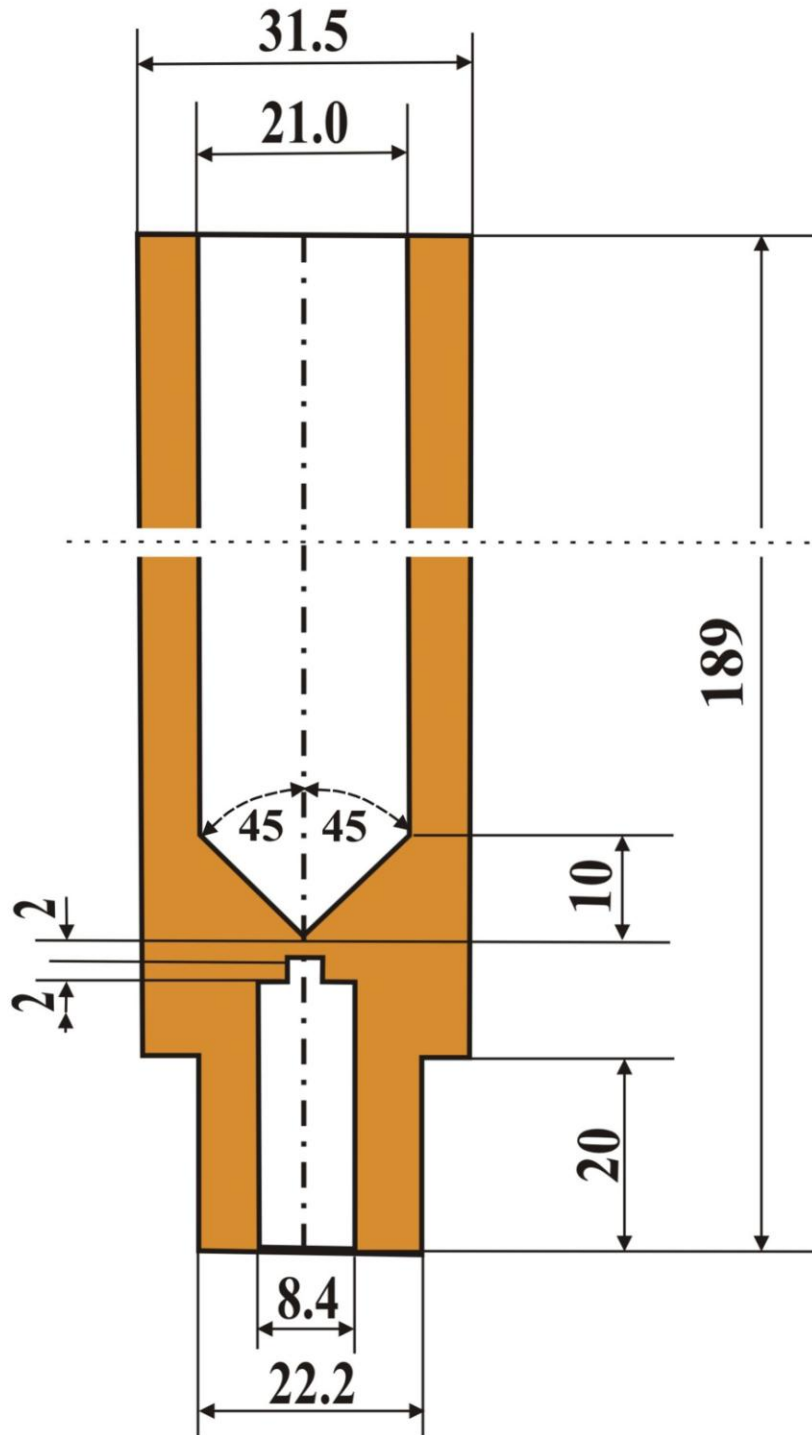
Figure 31. Schematic view - layout and dimensions of the crucibles used in the experiment for Bridgman-grown CaF$_2$ single crystals.

Preparation of PMMA, PMMA-CaF$_2$ and PMMA- CdSe films

In order to obtain the composite, CaF$_2$ in PMMA, it was first necessary to do several operations. First, it was necessary to get a CaF$_2$ powder of nanometer dimensions. CaF$_2$ single crystal plate was milled in air atmosphere in planetary ball mill Fritsch Pulverisette 5 (Figure 32). Then the mixture of PMMA and the previously obtained powder of CaF$_2$ further milled in the same vessel. Balls-to-powder mass ratio was 20:1. The angular velocity of the supporting disc and vial was 32 and 40 rad s^{-1}, respectively.
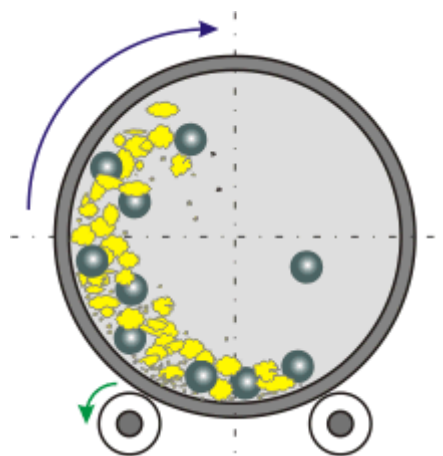
a)   b)

Figure 32. a) A planetary ball mill (Fritsch Pulverisette 5). b) Working principle of planetary ball mill. Schematic view of motion of the ball and powder mixture.

For the preparation of precursor solutions, acetone was used as the solvent for the PMMA. Homogenous solution of polymer with respect to the amount of composite films was prepared by dissolving the polymeric granules (PMMA, m = 10.65g) in 40 ml of acetone

under magnet stirring for 48 h at room temperature on the mixture. PMMA was therefore produced in form of film by solvent casting method, i.e. casting the resulting PMMA solution which we previously prepared on Petri dish in horizontal position. The solution was air dried for 24 h at room temperature and the obtained film was kept for further 24h in dryer under 60 ºC in order to eliminate residual solvent. For the preparation of composite film PMMA-CaF$_2$ the procedure was the same, and the appropriate content of CaF$_2$ for preparing 1% wt composite films was added. The mixture was stirred for 24 h. The casting solution method on Petri dish was performed by placed it on Petri dish, and then the spacemen was dried for 24 h at room temperature and further drier for 24 h in dryer oven under 60 ºC.

For the composite film PMMA-CdSe DMF was used as the solvent for the PMMA. In a typical process, homogenous solution of polymer with respect to the amount of composite films was prepared by dissolving the polymeric granules (PMMA, m = 10.65 g) in 40 ml of DMF under magnet stirring for 48 h at room temperature on the mixture. The concentration of PMMA in DMF solution was 22 %wt. PMMA was therefore produced in form of film by solvent casting method, i.e. casting the resulting PMMA solution which we previously prepared on Petri dish in horizontal position. The solution was air dried for 24 h at room temperature and the obtained film was kept for further 24h in dryer under 60 ºC in order to eliminate residual solvent.

For the synthesis of polymer/quantum dots (PMMA/ CdSe) composite films the procedure for solutions was similar. The concentration of PMMA in DMF solution was 22 % wt. The concentration of CdSe particles in films was 0.06 % wt. which prepared by dispersed CdSe particles in toluene, being the powder. The resulting suspension was directly added to PMMA solution previously prepared. The mixture was stirred for 24 h. The same procedure we did with CdSe-PMMA solution, i.e. casting CdSe-PMMA solution on Petri dish by placed it on Petri dish, and then the spacemen was dried for 24 h at room temperature and further drier for 24 h in dryer oven under 60 ºC.

The observations relating to the dislocation were recorded by observing an etched surface of CaF$_2$ crystal, using a Metaval of Carl Zeiss Java metallographic microscope with magnification of 270x. To test the dislocations were used CaF$_2$ samples that are obtained by cleaving the crystals CaF$_2$ per plane splitting <111>. The samples were etched with

concentrated sulfuric acid from 10 to 30 min. It has been shown that the best results are obtained on the sample crystal is etched for 15 min.

The crystal structure of CaF_2 single crystal was approved using the X-ray diffractometer (XRD, Model Philips PW 1050 diffractometer equipped with a PW 1730 generator, 40 kV x 20 mA, and using CuKα radiation of 1.540598 Å at the room temperature. Measurements were done in 2θ range of 10-90° with scanning step width of 0.05° and 10 s scanning time per step.

The micro-Raman spectra were taken in the backscattering configuration and analyzed by Jobin Yvon T64000 spectrometer, equipped with nitrogen cooled charged coupled device detector (Figure 33). As an excitation source we used the 532 nm line of Ti: Sapphire laser, with laser power 20 mW. The measurements were performed in the spectrum range 100 cm^{-1} to 800 cm^{-1}.
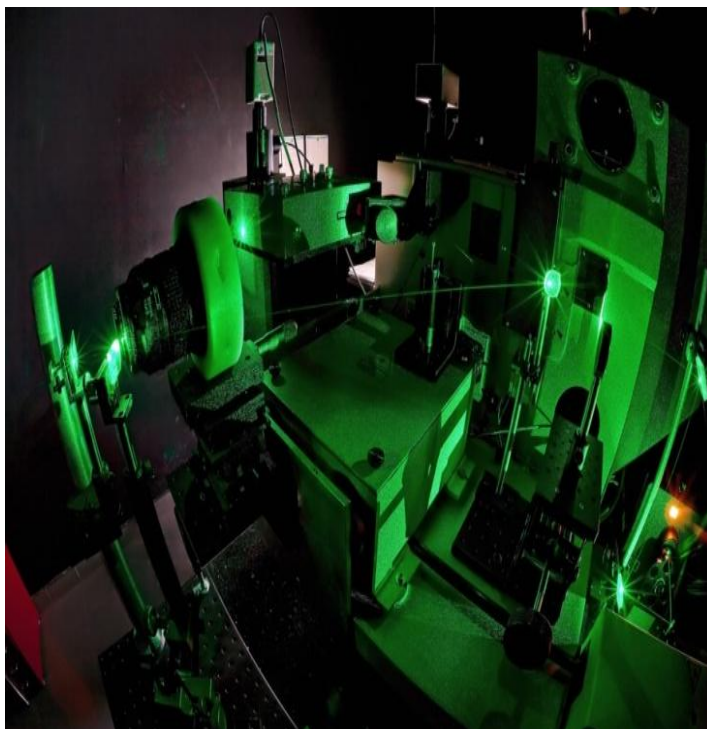
Figure 33. Raman spectrometer Jobin-Yvon T64000.

The room temperature far-infrared measurements were carried out with a BOMEM DA-8 FIR spectrometer (Figure 34). A DTGS pyroelectric detector was used to cover the wave number range from 40 to 500 cm^{-1}.

Figure 34. BOMEM DA-8 FIR spectrometer.

The transmission spectrum of PMMA, CaF_2 sample and composites (powdered and pressed in the disc with KBr) was obtained by transmission Fourier transforms infrared (FTIR) Hartmann&Braun spectrometer, MB-series. The FTIR spectrum was recorded between 4000 and 400 cm^{-1} with a resolution of 4 cm^{-1}.

Photoluminescence (PL) studies reported in this work were performed at room temperature using Optical Parametric Oscillator (Vibrant OPO) tuned at 350 nm as excitation source. The experimental setup used in this study consists of excitation and detection part. Pulsed excitation was provided by a tunable Nd:YAG laser system with pulse duration of about 5 ns and repetition rate of 10 Hz. Time resolved streak images of the emission spectrum excited by OPO system are collected by using a spectrograph (SpectraPro 2300i) and recorded with a Hamamatsu streak camera (model C4334). All streak camera operations are controlled by the HPD-TA (High Performance Digital Temporal Analyzer) software. The fundamental advantage of the streak camera is its two dimensional nature, enabling the acquiring of the temporal evolution of laser induced phenomena. The camera is equipped with image intensifier so single photons can be detected and counted, enabling the detection of even very small photoluminescence response of excited sample. The excitation and

detection optical axes were aligned using the beam splitter, so it was possible to tune the angle of excitation beam regarding the surface of sample and to maintain the high sensitivity of detection.

In order to study the electrical and dielectric properties of synthesized CaF_2 single crystal, the plan-parallel plate with dimensions of 11x11x 2 mm^3 was coated with high purity silver paste on adjacent faces as electrodes. AC (alternating current) parameters were measured using an impedance analyzer (Hewlett-Packard 4194A) at various temperatures between 25°C and 175°C in the frequency range 100 Hz to 1 MHz. For more details see Ref.[154] and Figure 35.

Impedance Analyzer HP–4194A   Data acquisition computer

Hewlett–Packard
Interface Bus (HP–IB)

sample   equivalent circuit

Cp   Rp
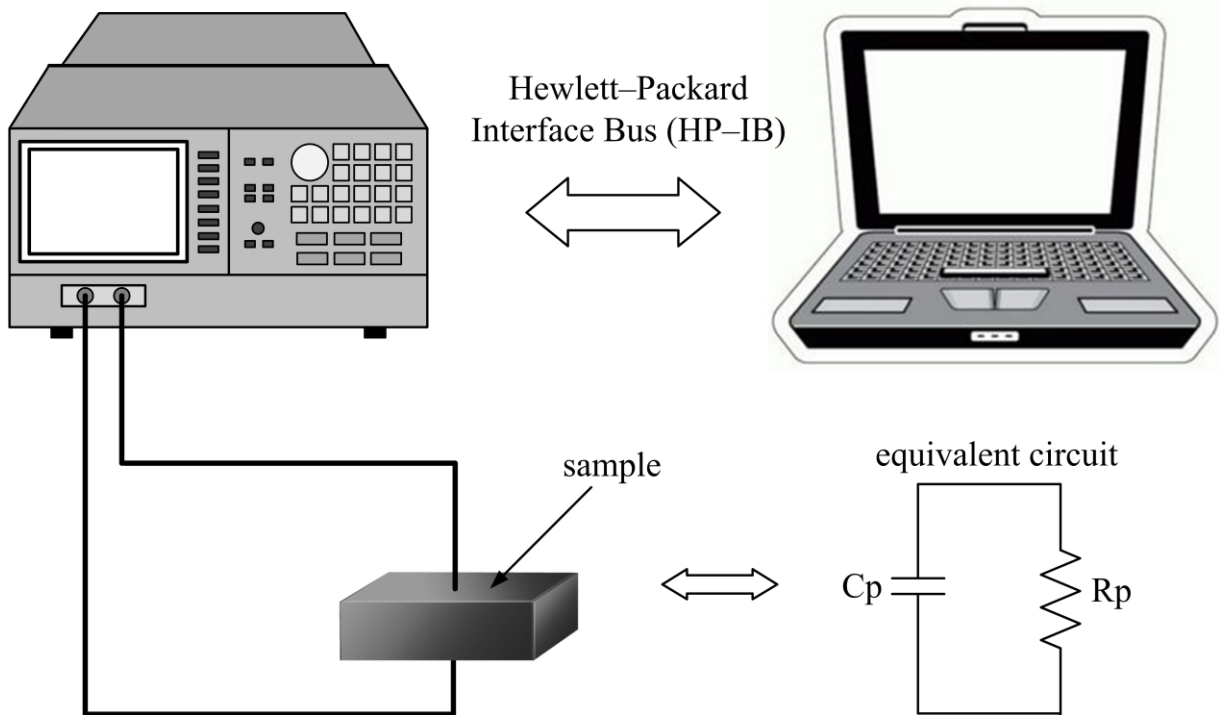
Figure 35. Schematic representation of prepared CaF$_2$ and its equivalent electric circuit.

RESULTS AND DISCUSSION

Results and discussion

Single crystal

CaF$_2$ single crystals are obtained by the vertical Bridgman method in vacuum. Experiments were carried out with the crystal growth rate of 6-48 mm h^{-1}. The best result was obtained with a crystal growth rate of 6 mm h^{-1}. If the growth rate of the single crystal CaF$_2$ larger, experiments showed that these crystals contain more stress and that in this case it is more likely to obtain polycrystals. Stresses in single crystals we have tried to eliminate annealing of crystals. The process of annealing was carried out on the plate and bulk crystal CaF$_2$. The temperature of annealing of the plate was at 1000 °C for 3 h, and the temperature of annealing of the bulk crystal was at 1000 °C and 1080 °C for 1 - 3 h. Annealing is carried out under an inert atmosphere of argon. It was noticed that after annealing, plate CaF$_2$ did not have enough stress. Annealing bulk single crystal CaF$_2$ had less stress than non-annealing. The obtained single crysta of CaF$_2$ was 20 mm in diameter and 90 mm in length (Figure 36). A polished plate of CaF$_2$ with a diameter of 20 mm is displayed in Figure 37.

Figure 36. Photographs of Bridgman-grown CaF$_2$ single crystal.
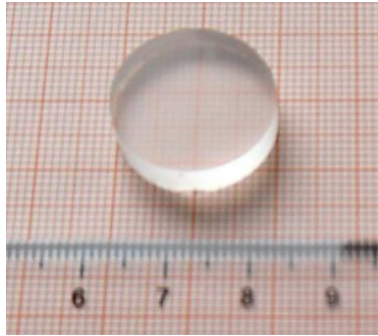
Figure 37. A polished plate of CaF$_2$.

The general conclusion is that in all samples was observed relatively high dislocation density (ranging from 60000 to 140000) as a consequence of greater internal stresses, which have emerged in the process of cooling. From the Figure 38 it can be observed dislocations on CaF$_2$ single crystal. Etch pits have the shape of a three-sided pyramid. Number of dislocations in CaF$_2$ crystals which were made by the method of Bridgman was $5 \cdot 10^4$ - $2 \cdot 10^5$ per cm^2 (Figure 38). Earlier we pointed out that it would eliminate the stress exerted we annealing process. During the annealing process is concluded that there is a movement of dislocations. The leads to the formation of sub-boundaries, and as a result, the internal stress in the crystal partially disappear. During the movement of dislocations their stress fields are partially reversed, but the dislocation density is practically not changed.
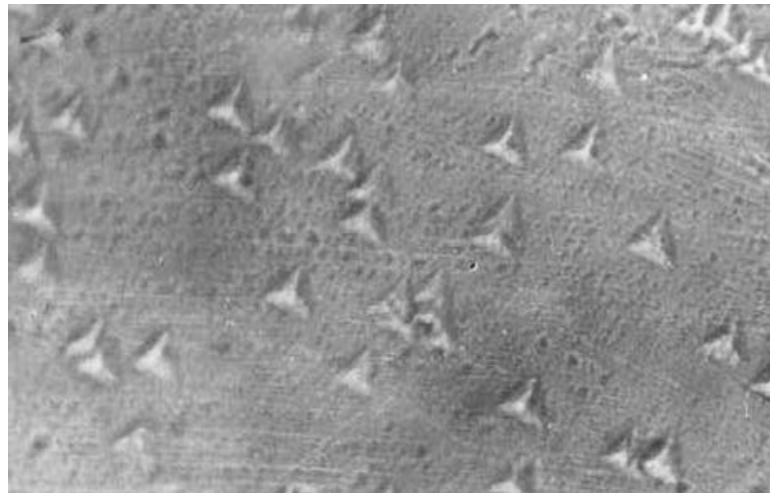
Figure 38. The microscopic image of the surface CaF$_2$ crystal plate in the direction <111>. Magnification of 270x.

The sample of CaF$_2$ single crystal was of cubic structure with the *Fm3m* space group [155]. XRD pattern (Figure 39) was indexed by using JCPDS database (card no. 87-0971). The XRD pattern was found to match exactly with those reported in the literature [103, 156,157]. The displayed peaks correspond to (*h k l*) values of (1 1 1), (2 2 0), (3 1 1), (4 0 0), (3 3 1) and (4 2 2). Using the (*h k l*) values of different peaks, the lattice constant (*a*) of the sample was calculated. Their lattice parameter was calculated from the equation of plane spacing for cubic crystal system and Bragg's law for diffraction [158]. The lattice parameter was 5.452±0.011 Å, calculated from the obtained XRD diagram, which was in good agreement with the literature [159].
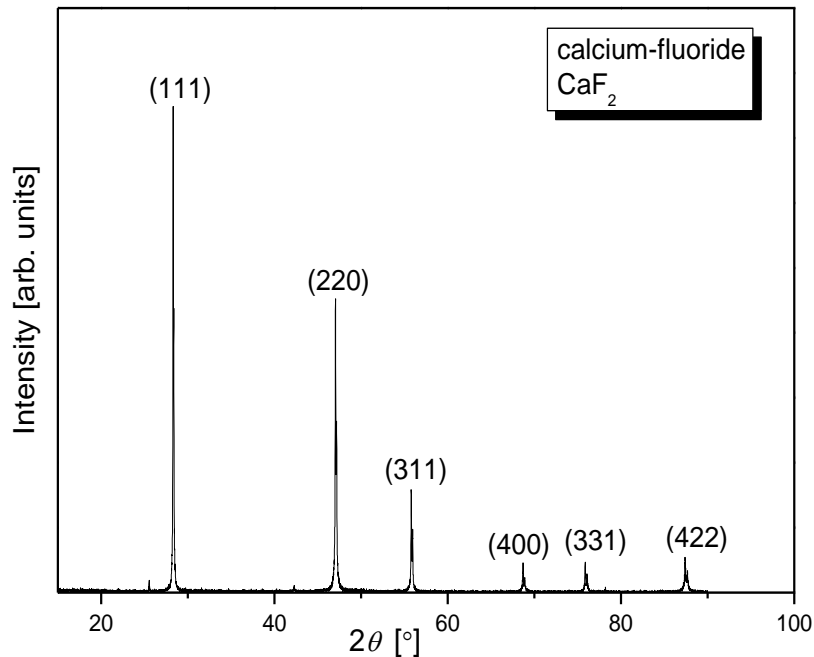
Figure 39. X-ray diffraction pattern of the CaF$_2$.

The primitive cell of a fluorite structure contains three nonequivalent atoms, corresponding to nine phonon modes in the dispersion relations, with three of them being the acoustic modes [160]. At the Γ point, there are three distinct optic phonon modes based on group theory analysis, and their representations are a doubly degenerate infrared-active TO T_{1u}, a triply degenerate Raman-active mode T_{2g}, and an infrared-active nondegenerate LO T_{1u} in the order of increasing phonon frequency. From the Γ to the X point along the <100> direction, the T_{1u} (TO) mode is correlated to a doubly degenerate dispersion following the

85

notation of Schmalzl et al., the T_{2g} mode is split into a doubly degenerate dispersion and a nondegenerate dispersion; and the T_{1u} (LO) mode is correlated to a nondegenerate dispersion [161].

Three atoms in cubic O_h^5 (*Fm3m*) primitive cell of the CaF_2 crystal are given nine fundamental vibrations, described by the following O_h-irreducible representations (at $k = 0$): $\Gamma = 2T_{1u} + T_{2g}$. According to several comprehensive work (see, e.g. [162-167]), their distribution among optical and acoustical are: the triply degenerate T_{2g} optical phonon is Raman active and IR inactive; one of the T_{1u} representations (triply degenerate as well) corresponds to the zero frequency acoustic mode, while the other T_{1u} species is actually split into a double degenerate transverse optical mode and a nondegenerate longitudinal optical mode, all the above are IR active. The room-temperature first order T_{2g} one-band spontaneous Raman scattering spectra of CaF_2 crystal is shown in Figure 40. In this single allowed SRS-promoting optical mode with frequency $\omega_{SRS} = 319.7$ cm^{-1} Ca^{2+} cation remains stationary and the neighboring substitutional fluoride F^{-1} ions vibrate against each other [169, 170].
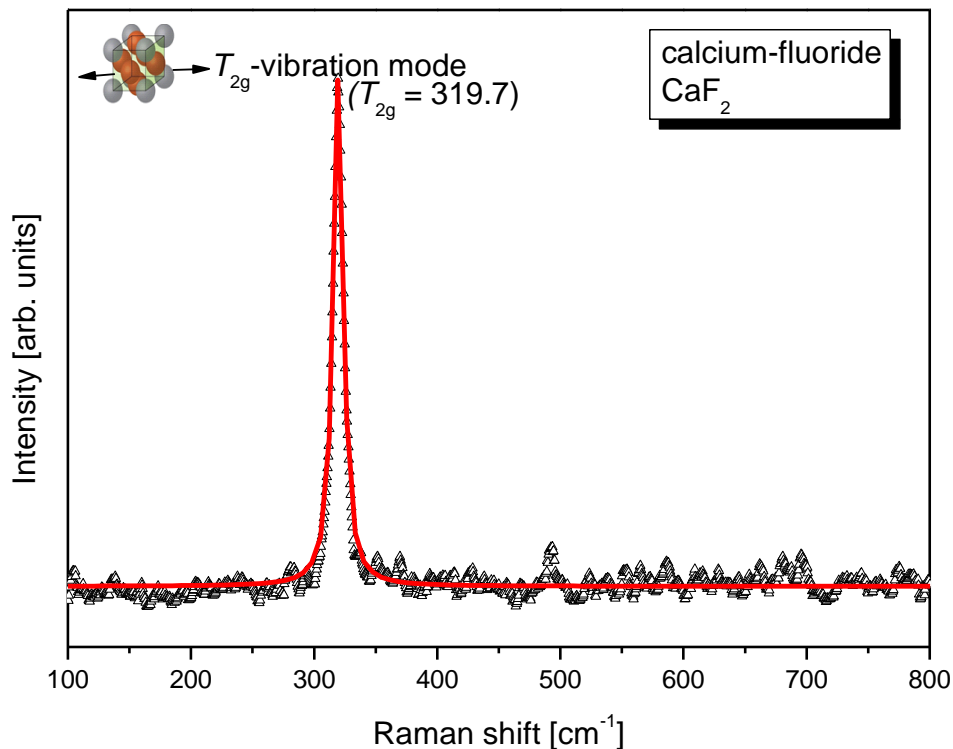
Figure 40. Raman spectra of the CaF_2 single crystal at room temperature.

FTIR transmission was measured in order to check the purity of the obtained CaF_2. As shown in Figure 41, the sharp peaks of the absorption at 2854 cm^{-1} and 2936 cm^{-1} are assigned to the symmetric and antisymmetric stretching vibration of -CH_2 groups [171]. Also, the spectra shows two broad IR absorption peaks at ~3432 cm^{-1} and 1628 cm^{-1} are assigned to the symmetrically stretching vibration and antisymmetric stretching vibration of hydroxyl groups -OH, implying the presence of H_2O molecules [172]. The peak at 671 cm^{-1} in the FTIR spectra was assigned to the Ca-F stretching vibration of CaF_2 [173]. The band at ~2357 cm^{-1} is due to KBr pellets used for recording FTIR spectrum [174].
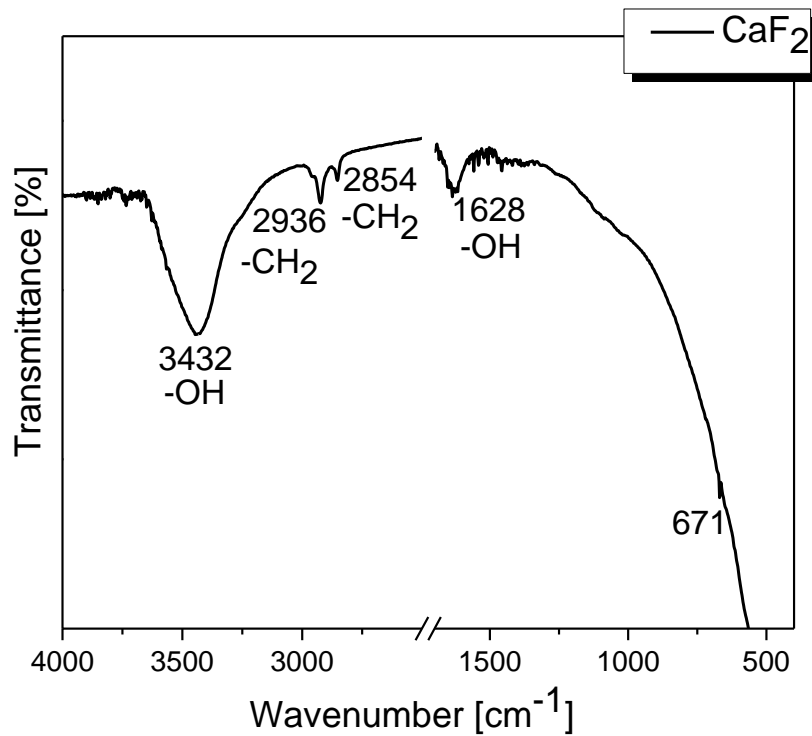
Figure 41. FTIR spectra of CaF$_2$.

The far-infrared reflectivity spectrum of the CaF_2 substrate is shown in Figure 42(a). The experimental data are presented with circles. The solid line in Figure 42(a) was obtained using the dielectric function in the factorized form given by Eq.(34) [175-177]:

$$\varepsilon(\omega) = \varepsilon_\infty \prod_{j=1}^{n} \frac{\omega_{jLO}^2 - \omega^2 + i\omega\gamma_{jLo}}{\omega_{jTO}^2 - \omega^2 + i\omega\gamma_{jTO}} \tag{34}$$

The number of modes is n, ω_{jLO} and ω_{jTO} are the longitudinal and transverse optical frequencies, γ_{jLO} and γ_{jTO} denote longitudinal and transverse damping constants, respectively, and $\varepsilon\infty$ is the dielectric constant (permittivity) at high frequency.

As a result of the best fit we obtained the $\omega_{TO} = 272$ cm^{-1} and $\omega_{LO} = 475$ cm^{-1}, some what higher than in Ref.[178] (TO/LO = 257/463). In pure CaF$_2$, only two infrared active modes are allowed by the crystal symmetry (splitted TO-LO mode), but we see that the main reflectivity band of CaF$_2$ exhibits a feature centred about 360 cm^{-1} as a result of a two-phonon combination. This feature has been observed in all stoichiometric fluorite-structured crystals [179]. There are two additional weak modes with relatively high dampings in the range of low energies. We suppose that mode about 130 cm^{-1} could be caused by impurities and about 200 cm^{-1} is a TO-mode from the X point <100>. Kramers-Kröning analysis of far-IR reflectance data gives $\omega_{TO} = 272$ cm^{-1} and $\omega_{LO} = 475$ cm^{-1}, in the accordance with fitting procedure (Figure 42(b)).

$\varepsilon_\infty = 1.5$			
ω_{TO}	γ_{TO}	ω_{LO}	γ_{LO}
272	31	319	46
323	67	399	67
414	66	**475**	52
129	65	139	65
197	73	203	53

$\omega_{TO} = 272$ cm^{-1}

$\omega_{LO} = 475$ cm^{-1}

ε_2

σ

Wave number [cm^{-1}]
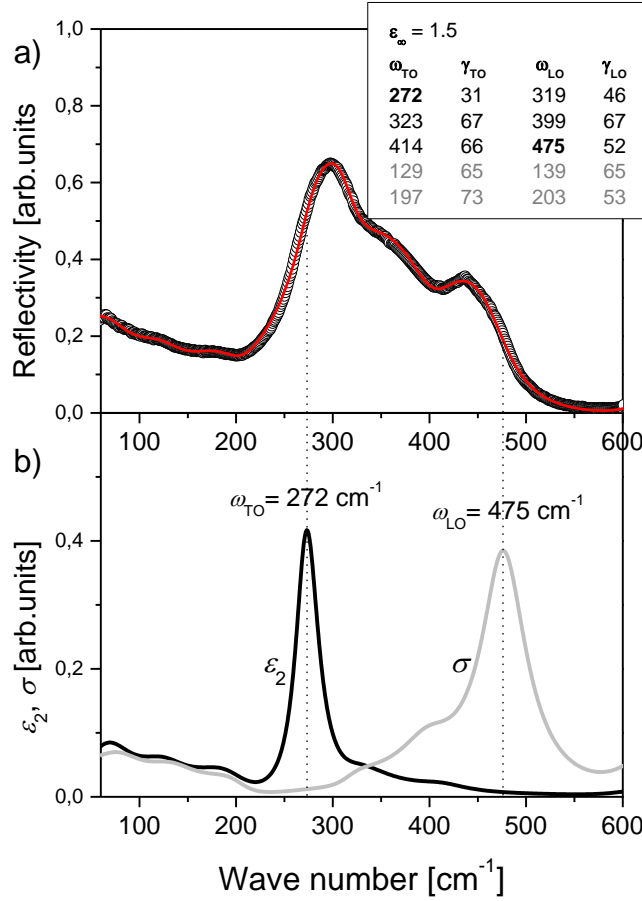
Figure 42. IR spectra of CaF$_2$ single crystals, recorded at room temperature.

We have measured the photoluminescence response of the CaF$_2$ crystal sample for various excitation wavelengths and different angles of excitation beam. The streak image of the fluorescence emission spectrum of CaF$_2$ is presented in Figure 43a). The photoluminescence response was very small, see Figure 36a) where typical optical response of sample is presented. Although the streak images were acquired in photon counting mode using very large number of expositions (20000), very small number of photons were counted. The vertical axis in Figure 43a) corresponds to the fluorescence development in time domain of 200 ns. The beginning of the vertical axis is cut off in order to avoid undesirable part of the spectra (excitation at 320 nm and second harmonic of Nd:YAG laser at 532 nm).
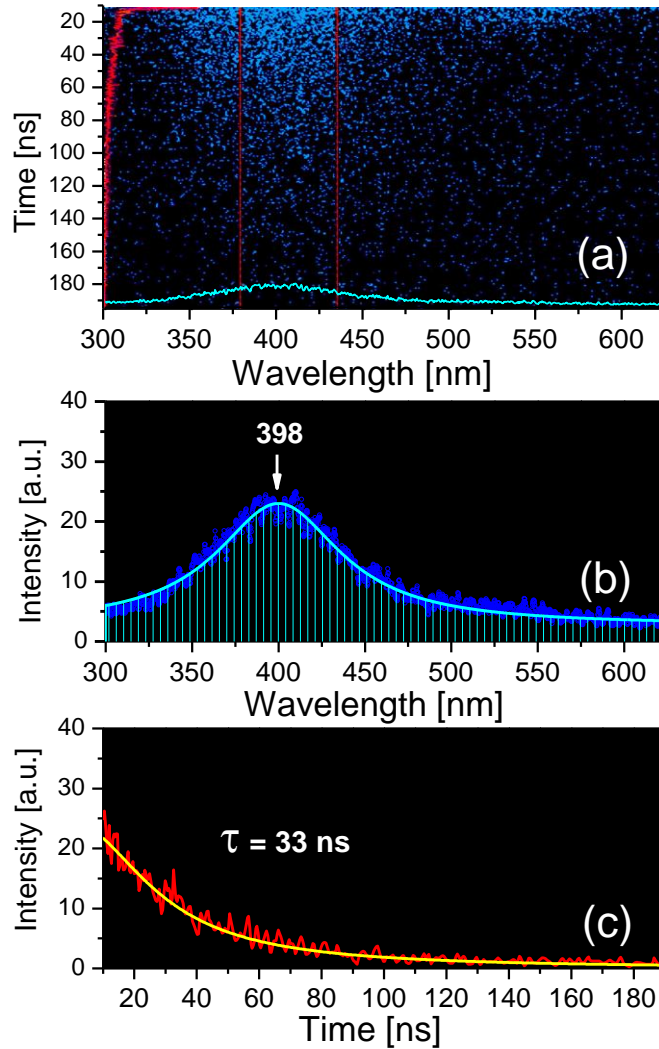
Figure 43. a) Streak image of the fluorescence spectra of CaF$_2$ crystal. b) Fluorescence spectra of CaF$_2$ crystal as a function of wavelength (integrated profile). c) Fluorescence spectra of CaF$_2$ crystal as a function of time (integrated profile) and fitted curve.

The photoluminescence response was very small, see Figure 43a) where typical optical response of sample is presented. Although the streak images were acquired in photon counting mode using very large number of expositions (20000), very small number of photons were counted. The vertical axis in Figure 43a) corresponds to the fluorescence development in time domain of 200 ns. The beginning of the vertical axis is cut off in order

to avoid undesirable part of the spectra (excitation at 320 nm and second harmonic of Nd:YAG laser at 532 nm).

Enlarged integrated profile of the fluorescence of CaF_2 is presented in Figure 43b). Our pure sample of CaF_2 crystal shows a broad band in 300-500 nm range. As pointed out in [180] this band might be induced due to the formation of color centers. These centers perhaps could be created by oxygen defects within the host of CaF_2. The luminescence of our sample is very weak compared to the luminescence of structure described in [180]. To obtain good luminescence response, the samples of CaF_2 are doped with Ag, Eu, Tb, Cu or Dy [180, 181]. However, CaF_2 crystal is usually used in applications where high optical transmission is needed and photoluminescence is not welcomed characteristics [182].

Fluorescence line profile (fluorescence decay) from image Figure 43a) is selected using the integration process in region from 340 nm to 460 nm. That profile is fitted using High Performance Digital Temporal Analyzer (HPD-TA) software, provided by Hamamatsu. Fluorescence decay and fitted curve are shown together in Figure 43c). The obtained lifetime is 33 ns ($\chi^2 = 1.07$).

The properties of the crystal, such as density of dislocations, cystallinity, and impurities concentrations, determine the optical quality.

The frequency dependence of the *AC* electrical conductivity i.e. conductivity spectrum for studied CaF_2 single crystal at various temperatures is shown in Figure 44. These plots indicate the existence of two contributions inside our sample. Namely, DC conductivity contribution is predominant at low frequencies and high temperatures, whereas the frequency-dependent term dominates at high frequencies. Moreover, the observed dispersion in the conductivity spectrum is shifted toward the higher frequency side with the increase of temperature. This variation of *AC* conductivity with frequency at different temperatures obeys the power law given by the empirical formula (Eq.(35)) proposed by Jonscher [183]:

$$\sigma_{AC}(\omega) = A\omega^s \tag{35}$$

where ω is the angular frequency of *AC* field. *A* and *s* ($0 \leq s \leq 1$) are the characteristic parameters which are temperature dependent. The Jonscher's coefficient s represents the degree of interaction between mobile ions with the lattices around them, and the prefactor parameter *A* determines the strength of polarizability [184]. In general, the nature of the

temperature dependence of frequency exponent s determines the AC conduction mechanism in the material [154].
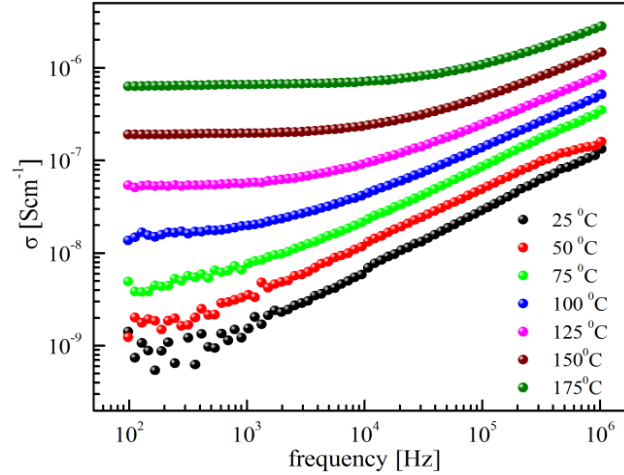
Figure 44. Frequency dependence of *AC* conductivity for

CaF$_2$ single crystal at different temperatures.

Changes in the real and imaginary part of complex impedance with frequency at different temperatures for CaF$_2$ single crystal are shown in Figure 45. It can be noticed that the magnitude of part of complex impedance (Z') decreases with an increase in both applied frequency and temperature, indicating an increase in AC electrical conductivity of the CaF$_2$ sample with increasing frequency and temperature. In addition, the temperature-dependent Z' shows a plateau on the low frequency side followed by a nearly negative slope on the high frequency side, indicating a crossover from low frequency relaxation behavior to high frequency dispersion phenomenon. This segment of nearly constant real impedance becomes dominant with increasing temperature, suggesting strengthened relaxation behavior [185].
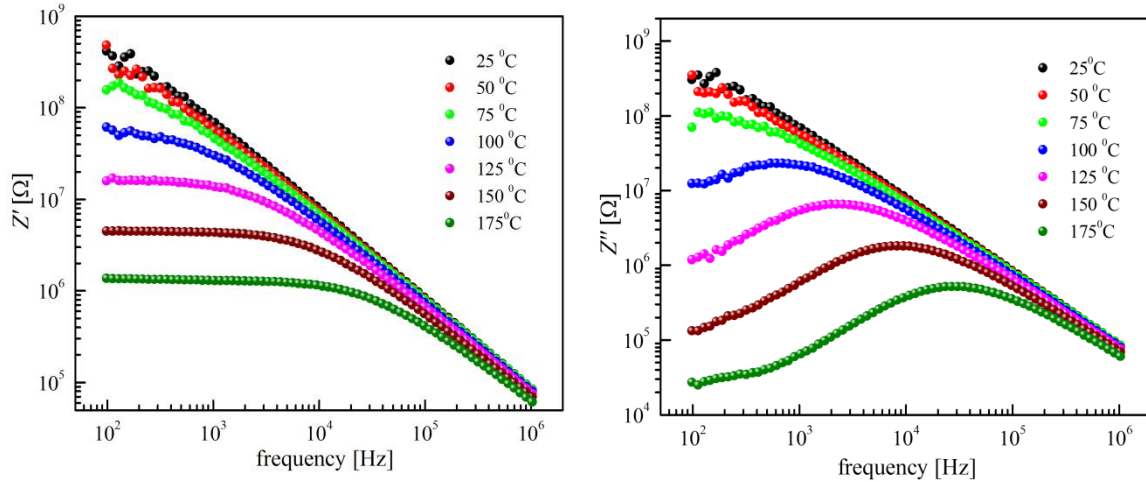
Figure 45. The variation of real part (left) and imaginary part (right) of the complex impedance with frequency at measured temperatures for CaF$_2$ single crystal.

The imaginary part of complex impedance (Z'') initially increases, reaches a peak and then decreases continuously with increasing frequency at all temperatures. It is evident that the Z'' spectrum of CaF$_2$ is characterized by the appearance of only one peak at a certain frequency that is called relaxation frequency. This suggests that a single relaxation process dominates over the conduction mechanism in synthesized CaF$_2$. As the temperature rises the magnitude of observed peak in Z'' spectrum decreases considerably with the peak shift towards higher frequency side. Such behavior indicates the presence of temperature dependent electrical relaxation phenomenon and that the relaxation time decreases with increasing temperature.

The representation of complex impedance data for CaF$_2$ single crystal in Nyquist/Cole-Cole plot at different temperatures is illustrated in Figure 46. All these plots are characterized by the presence of a single semicircle which corresponds to the bulk effects and indicates that the material is homogeneous. No residual semicircle at low frequencies attributed to the electrode effects has been noticed. Further, impedance spectra show depressed semicircles with their center below the real axis which points to the non-Debye type of relaxation [186].
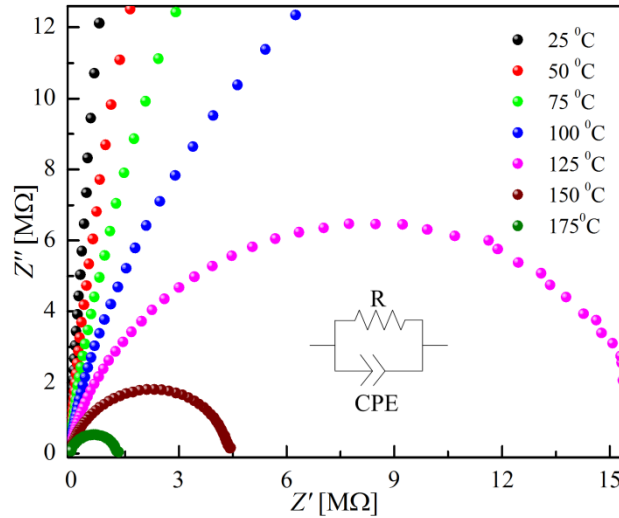
Figure 46. Impedance spectra of CaF$_2$ single crystal at selected temperatures. *Inset* **shows the proposed equivalent circuit model for analysis of the impedance data.**

In addition, the radius of the semicircles, which corresponds to the resistance of the material, decreases as temperature increases indicating a thermally activated conduction mechanism in studied CaF$_2$. It is well known that in single crystal materials this kind of impedance response can be interpreted by means of an equivalent electrical circuit model consisting of one parallel *RC* element [187]. But taking into account the observed non-ideal Debye type behavior of sample, it is usual that the constant phase element (CPE) is used instead of ordinary capacitor as shown in the insert of Figure 46.

The effect of applied electric field frequency on the dielectric constant of CaF$_2$ single crystal at different temperatures is represented in Figure 47. It is clear from the analysis of the graph that dielectric constant decreases continuously with increasing frequency, exhibiting a normal dielectric behavior [188].
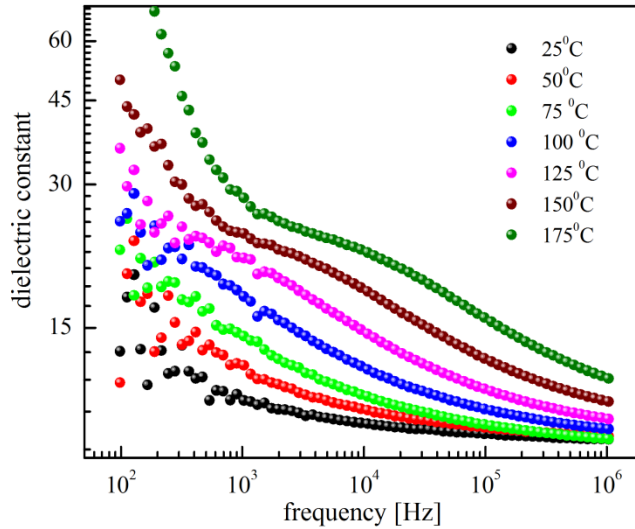
Figure 47. Frequency dependence of dielectric constant for CaF$_2$ single crystal at different temperatures.

A more significant dispersion in low frequency region can be explained based on the fact that the dielectric constant, in general, is directly related to the dielectric polarization. It can be observed that the variation of dielectric constant with temperature at low frequencies is much more pronounced than at higher frequencies. This relatively insignificant variation of dielectric constant with temperature at higher frequencies can be ascribed to the atomic and electronic polarizations which are temperature independent.

The nanoindentation test vas performed with the aim of obtained mechanical properties of CaF$_2$. Figure 48 shows typical force-depth curve obtained in the nanoindentation tests for CaF$_2$ single crystal. The curve appear sto be with continuity and without pop in or pop out in both loading and unloading phases. The results of reduced elastic modulus and hardness for CaF$_2$ single crystal are presented in Figure 48, and they are in according literature data.
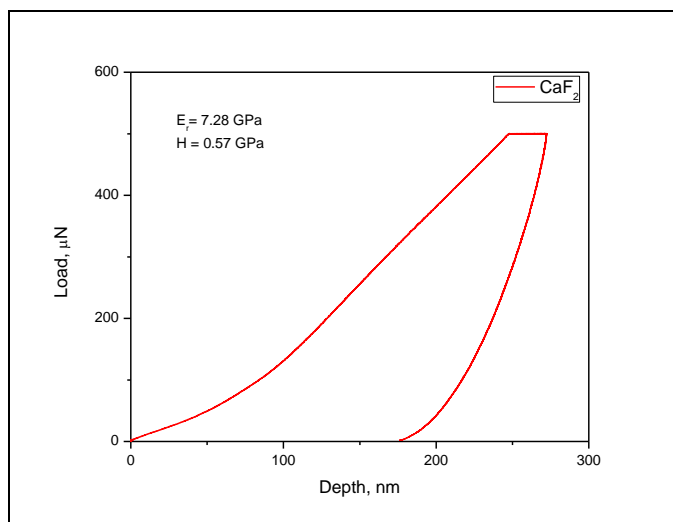
Figure 48. Load-depth nanindentation curve for CaF$_2$.

Composite PMMA-CaF$_2$

Results od DSC analysis for omposite films PMMA-CaF$_2$ are presented on Figure 49. Theese rasults revealed that the thermal propertis od polyner was improved by embedinf inorganic particles. T_g for composit was higher the for pure polymer.
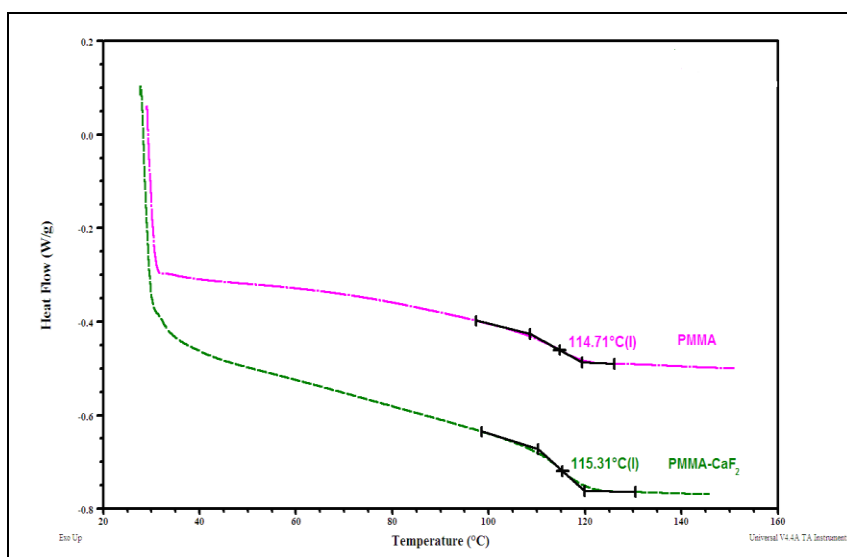
Figure 49. DSC analysis.

Figure 50 a) shows the FTIR spectrum of as prepared CaF$_2$ single crystal. The spectrum shows two strong IR absorption bands at ~3432 and 1628 cm^{-1}. They are characteristic of H-O-H bending of the H$_2$O molecules. This reveals the presence hydroxyl groups in the as prepared sample. The fundamental frequency at ~364 cm^{-1} arises due to hindered rotations of the hydroxyl ions. The band at ~2357 cm-1 is due to KBr pellets used for recording FTIR spectrum.
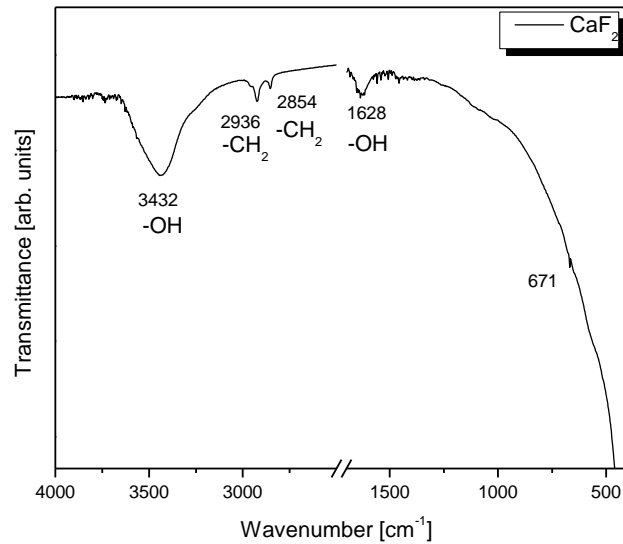
a)
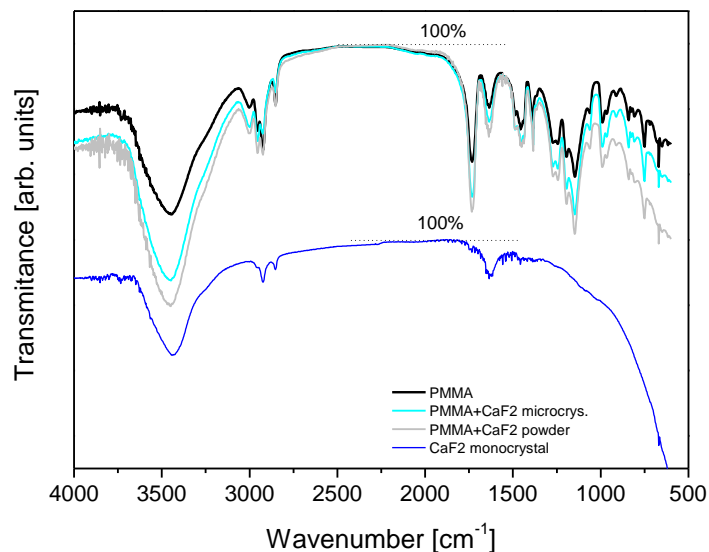
b)

Figure 50. FTIR spectrum of a) CaF$_2$ and b) PMMA and composite.

The transmission spectra (Figure 50 b)) of PMMA, PMMA with the addition of 1% of the microcrystals CaF_2, or 2% CaF_2 powder, are shown together with the spectrum of a single crystal CaF_2 in the range of wave number 4000 cm^{-1} and 500 cm^{-1}. It is notable that the transmittance spectra of PMMA with the addition of CaF_2 lower than the transmittance of pure PMMA in parts of the spectrum which correspond to a lower value of the transmittance of the single crystal CaF_2, i.e. for a wave number more than about 3000 cm^{-1} and below 1500 cm^{-1}. The reduction of transmittance is higher when the CaF_2 particles dispersed in the PMMA matrix finer (powder). In the area of wave number than 600 cm^-, CaF_2 has a reflectance equal to zero in practice, and in the same area have the transmittance which differs from 100% in the parts of the spectrum that correspond to the absorbed water vapor or gases from the atmosphere. Visible minima in the spectra of PMMA corresponding to literature values [189-191]. Spectrum for PMMA (Figure 50 b)) exhibits typical vibrational bands, *i.e.*, vibrational bands at 987 and 1453 cm^{-1} that belong to O-CH$_3$ bending and stretching deformation of PMMA, respectively, bands at 1730 and 1250 cm^{-1} that are assigned to stretching of C=O groups, a band at 1065 cm^{-1} that could be ascribed to the C-O stretching vibration and a band at 1197 cm^{-1} that belongs to the skeletal chain vibration. The other bands appearing in the 3000-2800 cm^{-1}, 1490-1275 cm^{-1} and 900-750 cm^{-1} spectral regions correspond to different CH$_3$– and CH$_2$– vibrational modes [189, 190]. FTIR spectrum of composites there are well defined peaks for PMMA and some of the vibration modes of Ca–F bond at 671 cm^{-1}. This means that CaF_2 crystals in the composite have been identified and that no other bounds with PMMA were created during the processing.

The Raman spectra of CaF_2 single crystal, PMMA and the composites 1% and 2% CaF_2 with PMMA in spectral range from 200 to 1000 cm^{-1} at room temperature are shown in Figure 51. The Raman spectra shows of a composite that makes the PMMA matrix with addition of 1% and 2% CaF_2 crystallites - microcrystals the average size of 50 nm, i.e, a finer powder with a grain size of 10-20 nm. Also, in addition to the composite spectrum are shown in both spectra, i.e. spectra of pure PMMA and CaF_2 single crystal, for ease of comparison. In the composite spectra of PMMA with CaF_2 powder, the peak intensity of the nanocrystal CaF_2 is very bad. In the composite spectra of PMMA and microcrystals of CaF_2 can be clearly seen CaF_2 peak whose intensity increases with increasing concentration of

microcrystals. In Figure 51b) is the result of the deconvolution of a part of Raman spectrum peak in the vicinity of CaF_2 in the case of composites with a 2% of nanocrystallites or 2% CaF_2 powder. The peaks were fit with the Lorentzian function, and the positions of the PMMA peaks practically coincide in both cases is selected. However, the peak of CaF_2 nanopowder is 0.4 cm^{-1} less than peak CaF_2 microcrystals. This is the expected effect of lowering energy Raman peaks with decreasing dimensions of nanoparticles. Lowering energy peaks should be particularly pronounced in relation to balk. Unfortunately, our crystal sample was measured second Raman spectrometer with a higher excitation energy, and is due to heating of the sample was a shift towards lower peak energies. Peaks in the Raman spectrum of PMMA can assign to the Ref.-s Willis and Bensaid [191].

a)   b)
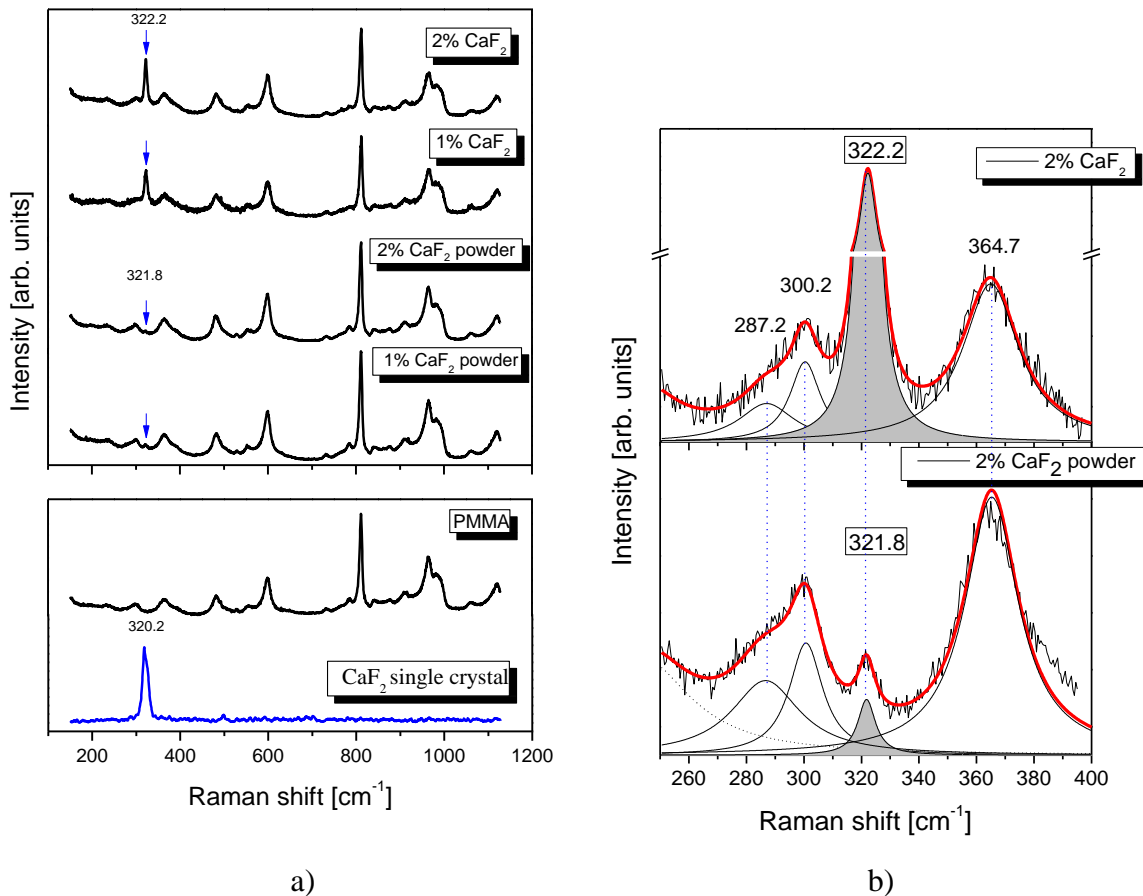
Figure 51. a) Raman shift of CaF_2 single crystal, PMMA and PMMA-CaF_2 composites. b) Details from the Raman spectrum of 2% CaF_2 single crystal and 2% CaF_2 powder in the range 250-400 cm^{-1}.

Nanocomposite film PMMA-CdSe

The PMMA film and nanocomposite have been further characterized with FTIR (Figure 52) to determine if any changes in functionality occurred in the composite film due to chemical interactions between the PMMA and the quantum dots. Spectrum of PMMA exhibits typical vibrational bands, *i.e.*, vibrational bands at 986 and 1453 cm^{-1} that belong to O–CH$_3$ bending and the stretching deformation of PMMA, respectively, bands at 1732 and 1250 cm^{-1} that are assigned to the stretching of C=O groups, a band at 1065 cm^{-1} that could be ascribed to the C–O stretching vibration and a band at 1197 cm^{-1} that belongs to the skeletal chain vibration. The other bands appearing in 3000-2800 cm^{-1}, 1490-1275 cm^{-1} and 900-750 cm^{-1} spectral regions correspond to different CH$_3$– and CH$_2$– vibrational modes [189, 193].

The spectra of pure PMMA and of CdSe/PMMA nanocomposite are almost identical. All of the stretching vibrations observed in the PMMA appeared in the nanocomposite with a higher intensity. A band at 624 cm^{-1} is due to the stretching frequency of Cd–Se bond [194].
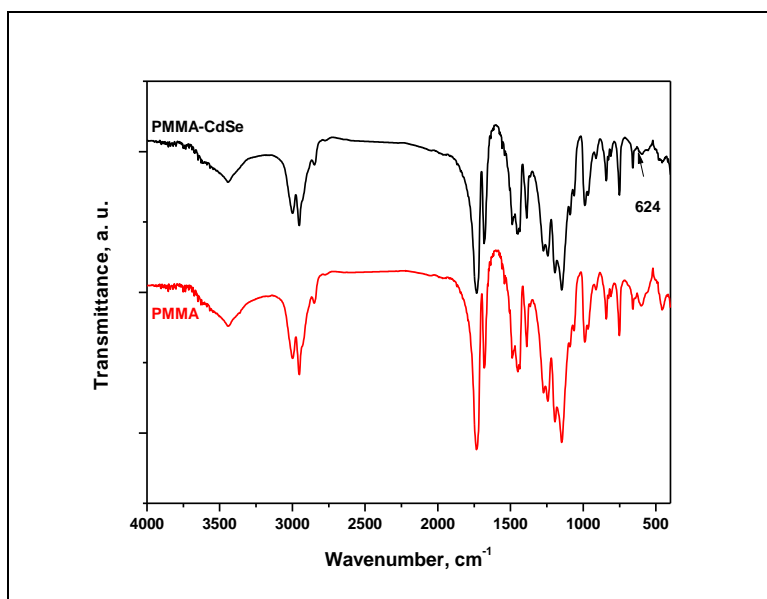
Figure 52. FTIR spectrum of pure PMMA film and PMMA/CdSe film.

FESEM photos of the fracture surfaces of composite films with QD particles are presented in Figure 53. As could be seen, some level of the agglomeration of QD is presented.
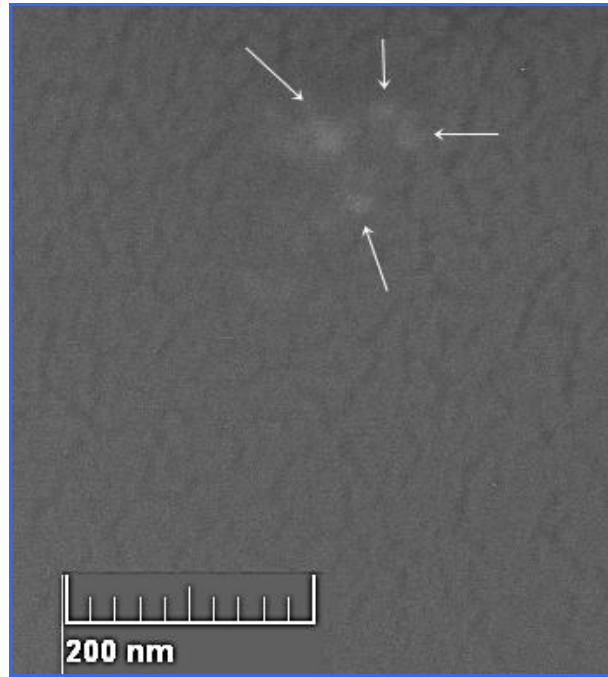
Figure 25. FESEM of composite film surface (the arrows marked QD).

Results of DSC for pure PMMA and composite are presented in Figure 54. The phase behavior of the polymer nanocomposite affected by an inclusion of a small fraction of QDs was exploited in a DSC by checking the glass transition temperature T_g change. Thermal analysis presented on Figure 54 shows that there is around 1% increase in T_g value for PMMA-CdSe nanocomposite, compared to the pure PMMA film. This finding has revealed that the agglomerates of QDs did not disrupt mechanical properties of the polymer. A small increase in T_g suggested that QDs behave as a functional physical crosslink, which would confirm the absence of a covalent bond between the polymer and the particles assumed by the FTIR analysis.
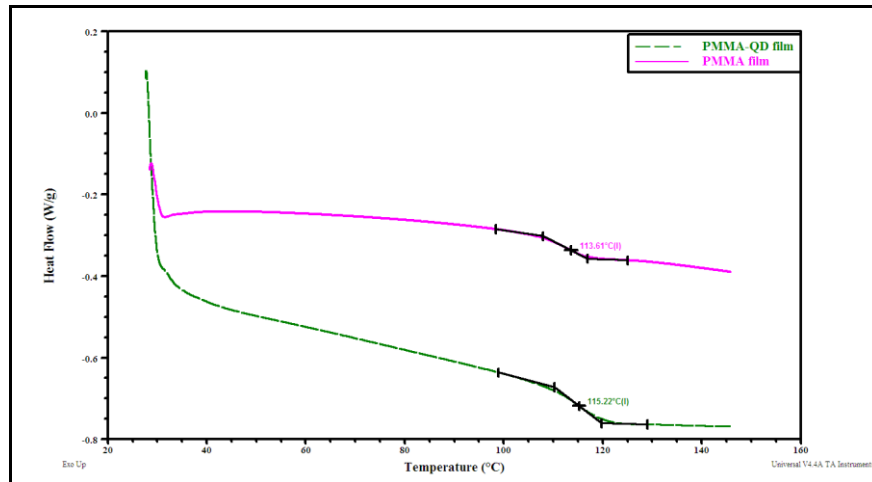
Figure 54. DSC of pure PMMA and the composite.

In order to obtain an overview of the possible inhomogenity in the sample, nanoindentation measurements were performed on nine positions for every sample. Figure 55a) shows typical force-depth curves obtained in the nanoindentation tests for neat PMMA film and a composite with CdSe. The curves appear to be with continuity and without pop-in or pop-out in both loading and unloading phases. Figure 55b) displays the plastic imprint of the indent for the sample with QD particles. In-situ imaging mode used for scanning the surface trace reveals the absence of cracks and fractures around the indent. The relative increase of reduced elastic modulus and hardness compared to the neat PMMA was 3.8 % and 15.9 % respectively (Table 1). The hardness (*H*) of a material is a measure of its resistance to shear stresses under local volume compression. The increased resistance to surface deformation of the PMMA nanocomposite may be due to a decrease in the free volume of the matrix associated with the formation of apparent physical crosslinking and the entanglements. This increase of the hardness is in the agreement with the increase of T_g because both of them are closely related to the cohesive energy density of the polymer [195-197].

102

Table 1. Results of nanoindentation test.

Sample	Er, GPa	St Dev, GPa	H, GPa	St Dev, GPa
PMMA	5.528861	0.320653	0.327145	0.022659
PMMA CdSe film	5.742875	0.282497	0.379106	0.023848
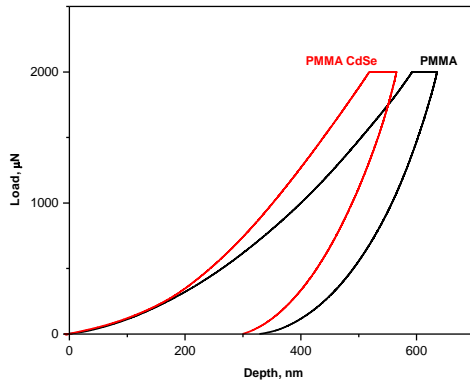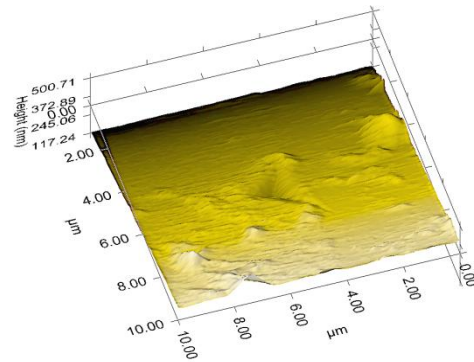
a)   b)

Figure 55. a) Force-depth curves obtained by nanoindentation, for pure PMMA and composite films. b) The plastic imprint of the indent for the sample with QD particles.

Streak images of fluorescence spectra of CdSe QDs liquid solution (as received) and CdSe QD/PMMA film are shown in Figure 56. The images, recorded as a 2D matrix, enable both lifetime and fluorescence spectral characteristics analysis of the samples. Fluorescence emission peak of CdSe QDs liquid solution (Figure 56a)) is at 610 nm, as expected, because quantum dots with such fluorescence characteristics were obtained and used in this study. The typical nanosized CdSe is a cluster of several smaller nanocrystals. Due to extremely small dimension and high surface energy, these nanocrystallites agglomerate to give a

103

resultant average size [198, 199]. For CdSe QD/PMMA film (Figure 56b)), there is a slight blue shift (peak is at 606 nm) due to a deagglomeration of some of the quantum dots during the process of the fabrication of the film.

The fluorescence lifetime of CdSe QD liquid solution and CdSe QD/PMMA film was calculated, obtaining the values of 1.8 ns and 2.1 ns respectively. The fluorescence lifetime of analyzed CdSe QD material is slightly increased when quantum dots are hosted in PMMA.

(a)   (b)
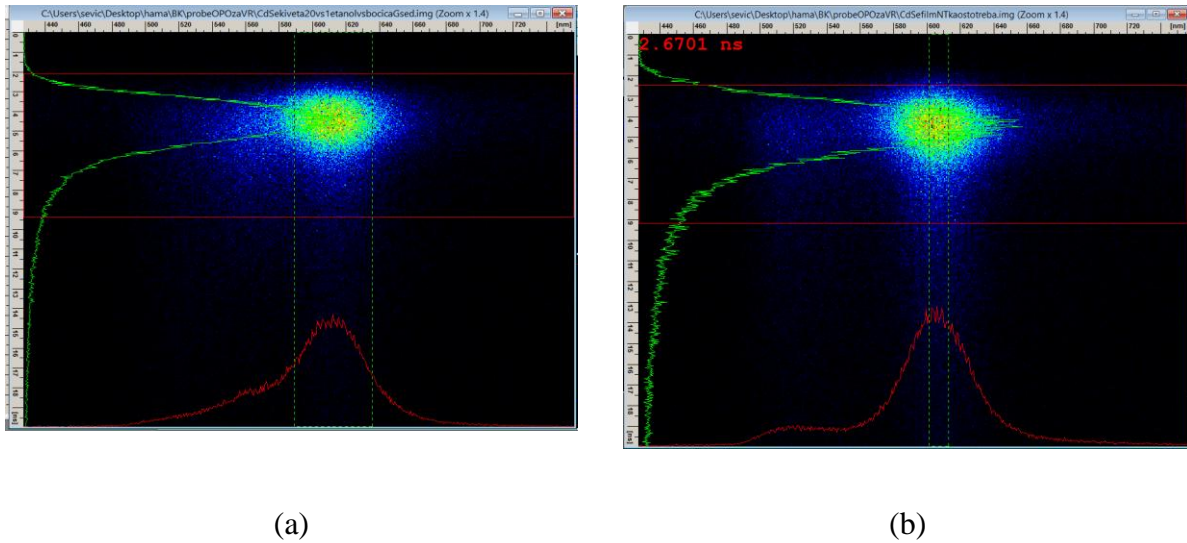
Figure 56. Streak images of fluorescence spectra of a) CdSe QD liquid solution and b) CdSe QD/PMMA film [200].

CONCLUSIONS

Conclusion

In this dissertation the posibility of synthesis of optical active composites with improoved mechanical, thermal properties and functionality was investigated. Synthesis and characterisation of nano to mikro modified polymer composites on the basis of single crystal are performed. The plymer matrix was poly (methyl methacrylate) – PMMA. One approach was the embedding of materials with similar values of the refractive index. Within this selection of this materials fell on the poly (methyl methacrylate) with an index of refraction $n_{600} = 1.49$, and calcium fluoride with $n_{600} = 1.43$. Another approach was use of the inorganic particle size smaller than the wavelength of electromagnetic radiation to avoid scattering. The single crystal one dimension (1D) quantum dots CdSe was embedded in PMMA.

Experimental part was performed in two directions: synthesis of single-crystal CaF_2 as a functional carrier and embedding in the polymer matrix; and synthesis and characterization of polymer matrix composites incorporating CdSe quantum dots. All materials, started and obtained composites, were characterized with aim to investigate influence of processing parameters and components on the quality of obtained optical active composite materials.

Firstly, XRD analysis was used for the crystalline phase detection and orientation of CaF_2 single crystal obtained by modified method the vertical Bridgman in vacuum. Method of photoluminescence was used to determined whether there are defects due to the presence of oxygen. Testing of the optical properties was conducted using the Raman spectroscopy, infrared spectroscopy, and the emission spectrum of the method of time-resolved laser-induced fluorescence. Established chemical bonding in the composite, and the modified polymer were tested using FTIR spectroscopy. The thermal properties were examined using DSC analysis. Morphology as well as composites of structure and distribution of particles in the composite was examined by scanning electron microscopy (SEM). Mechanical properties were tested by method of nanoindentation, Vickers microhardness and tensile tests.

CaF_2 single crystals in diameter of 20 mm are obtained by the vertical Bridgman method in vacuum. The crystal growth rate was 6.0 mm h^{-1}. In order to eliminate stresses in the crystal, a crystal annealing is carried out on the plate and bulk CaF_2. Number of dislocations is of the order of 5×10^4 - 2×10^5 per cm^2. During the annealing process is

concluded that there is a movement of dislocations. The leads to the formation of sub-boundaries, and as a result, the internal stress in the crystal partially disappear. During the movement of dislocations their stress fields are partially reversed, but the dislocation density is practically not changed.

As a result of the best fit we obtained the $\omega_{TO} = 272$ cm^{-1} and $\omega_{LO} = 475$ cm^{-1}, some what higher than in literture data (TO/LO = 257/463). In pure CaF$_2$, only two infrared active modes are allowed by the crystal symmetry (splitted TO-LO mode), but we see that the main reflectivity band of CaF$_2$ exhibits a feature centred about 360 cm^{-1} as a result of a two-phonon combination. This feature has been observed in all stoichiometric fluorite-structured crystals . There are two additional weak modes with relatively high dampings in the range of low energies. We suppose that mode about 130 cm^{-1} could be caused by impurities and about 200 cm^{-1} is a TO-mode from the X point <100>. Kramers-Kröning analysis of far-IR reflectance data gives $\omega_{TO} = 272$ cm^{-1} and $\omega_{LO} = 475$ cm^{-1}, in the accordance with fitting procedure. The FTIR transmission spectra indicate that there are some amounts of -CH$_2$, -OH or water molecules and organic groups adhering to the surfaces. Photoluminescence intensity of the obtained crystal is very low, what is an advantage for applications where high optical transmission is needed. Based on our work and observations during the experiment, it could be concluded that the obtained transparent single crystal CaF$_2$ is of good optical quality, which was the goal of our work. The variation of dielectric constant with temperature at higher frequencies can be ascribed to the atomic and electronic polarizations which are temperature independent.

Composite films PMMA-CaF$_2$ was obtained with preserved optical properties of single crystals, whereas the thermal and mechanical properties improved. Results od DSC analysis for omposite films PMMA-CaF$_2$ revealed that the thermal propertis od polyner was improved by embedinf inorganic particles. T_g for composit was higher the for pure polymer. FTIR spectrum of composites there are well defined peaks for PMMA and some of the vibration modes of Ca–F bond at 671 cm^{-1}. This means that CaF$_2$ crystals in the composite have been identified and that no other bounds with PMMA were created during the processing. The Raman spectra of CaF$_2$ single crystal, PMMA and the composites revelaed all modes found are well matched with literatures. By addition of 1% and 2% CaF$_2$ crystals

can be seen the peaks are the same as in the spectrum of PMMA. The intensity of these peaks in the composite are about 364, 481, 600, 812 and 964 cm^{-1}. It was also noted a sharp peak at 323 cm^{-1} which is characteristic of CaF$_2$. A weak band near 400 cm^{-1} in possibly be δ(C—O—C) in spectrum of the PMMA and the composites 1% and 2% CaF$_2$ with PMMA.

The preparation of composites PMMA doped with CdSe QDs was performed utilizing the solution casting technique. The results obtained from the DSC showed that on the addition of QDs, T_g value of the PMMA slightly increased, suggesting that the nanoparticles formed aggregates which have not disrupted mechanical performance of the polymer. The time resolved analysis of the nanocomposites revealed that the fluorescence of the powder was preserved in the composite. The fluorescence lifetime of PMMA doped with QDs has also slightly increased. As shown by the nanoindentation tests, incorporation of 3 wt % of QDs increased the reduced modulus and the hardness of PMMA composite for 3.8 % and 15.9 %, respectively. The presented results suggested that PMMA/QD nanocomposites have good potential for the use in light sensitivity elements and optoelectronic devices.

REFERENCES

References

1. B. S. Mitchell, An Introduction to Materials Engineering and Science: for Chemical and Materials Engineers, John Wiley&Sons, New Jersy, 2004.

2. P. K. Mallick, Fiber-Reinforced Composites, Materials, Manufacturing, and Design, 3rd edition, Taylor&Francis Group, Boca Raton, 2007.

3. B. D. Agarwal, L. J. Broutman, Analysis and Performance of Fiber Composites, 2nd edition, Wiley, New York, 1990.

4. K. H. Ashbee, Fundamental Principles of Fiber Reinforced Composites, 2nd edition, Technomic Publishing Company, Lancaster, PA, 1993.

5. ASM Handbook, vol. 21, Composites, ASM International, Materials Park, OH, 2001.

6. K. K. Chawla, Composite Materials Science and Engineering, 2nd edition, Springer-Verlag, New York, 1998.

5. T. W. Chou, R. L. McCullough, R. B. Pipes, Composites, Scientific American, vol. 255, no. 4, 1986, pp. 192-203.

7. L. Hollaway, Handbook of Polymer Composites for Engineers, Technomic Publishing Company, Lancaster, PA, 1994.

8. D. Hull, T. W. Clyne, An Introduction to Composite Materials, 2nd edition, Cambridge University Press, New York, 1996.

9. S. T. Peters, Handbook of Composites, 2nd edition, Springer-Verlag, New York, 1998.

10. V. L. Pushparaj, M. M. Shaijumon, A. Kumar, S. Murugesan, L. Ci, R. Vajtai, R. J. Linhardt, O. Nalamasu, P. M. Ajayan, Proc. Natl. Acad. Sci. USA 2007, 104, 13574.

11. E. Sunden, J. K. Moon, C. P. Wong, W. P. King, S. Graham, J. Vac. Sci. Technol. B, 2006, 24, 1947.

12. Y. J. Jung, S. Kar, S. Talapatra, C. Soldano, G. Viswanathan, X. S. Li, Z. L. Yao, F. S. Ou, A. Avadhanula, R. Vajtai, S. Curran, O. Nalamasu, P. M. Ajayan, Nano Lett., 2006, 6, 413.

13. N. R. Raravikar, A. S. Vijayaraghavan, P. Keblinski, L. S. Schadler, P. M. Ajayan, Small., 2005, 1, 317.

14. E. B. Sansom, D. Rinderknecht, M. Gharib, Nanotechnology, 2008, 19, 035302.

15. D. Meissner, R. Memming, B. Kastening, Chem. Phys. Lett., 1983, 96, 34.

16. M. P. Zach, K. Inazu, K. H. Ng, J. C. Hemminger, R. M. Penner, Chem. Mater., 2002, 14, 3206.

17. S. A. Morin, F. F. Amos, S. Jin, J. Am. Chem. Soc., 2007, 129, 13776.

18. K. E. Plass, M. A. Filler, J. M. Spurgeon, B. M. Kayes, S. Maldonado, B. S. Brunschwig, H. A. Atwater, N. S. Lewis, Adv. Mater., 2009, 21, 325.

19. R. G. Newton, Scattering Theory of Waves and Particles, second edition, Dover Publications, Inc., Mineola, New York, 2002.

20. S. Komarneni, J. Mater. Chem., 1992, 2, 1219.

21. P. N. Prasad, Nanophotonics , John Weiley&Sons, New Jersey, 2004, p.277.

22. S. Coe, W.K. Woo, M . Bawendi, V. Bulovic, Nature (2002), 420, 800

23. A. A. Mamedov, A. Belov, M. Giersig, N. N. Mamedova, N. Kotov, J. Am. Chem. Soc., 2001, 123, 7738.

24. M. Bruchez, M. Moronne, P. Gin, S. Weiss, A. P. Alivisatos, Science, 1998, 281, 2013.

25. N. Charve, P. Reiss, A. Roget, A. Dupuis, D. Grundwald, S. Crayon, F. Chandezon, T. Livache, J. Mater. Chem., 2004, 14, 2638.

26. Y. Xuan, D. Pan, N. Zhao, X. Ji, D. Ma, Nanotechnology, 2006, 17, 4966.

27. V. V. Ginzburg, F. Qiu, M. Paniconi, G. Peng, D. Jasnow, A. C. Balazs, Phys. Rev. Lett., 1999, 82, 4026.

28. Y. Tang, T. J. Ma, Chem. Phys., 2002, 116, 7719.

29. M. Laradji, G. J. MacNevin, Chem. Phys., 2003, 119, 2275.

30. C. Minelli, I. Geissbuehler, R. Eckert, H. Vogel, H. Heinzelmann, M. Liley, Colloid Polym. Sci., 2004, 282, 1274.

31. H. R. Allcock, J. D. Bender, Y. Chang, Chem. Mater., 2003, 15, 473.

32. C. Lu, B. Yang, J. Mater. Chem., 2009, 19, 2884.

33. S. A. Soper, S. M. Ford, S. Qi, R. L. McCarley, K. Kelly, M. C. Murphy, Anal. Chem., 2000, 72, 642.

34. R. L. McCarley, B. Vaidya, S. Wei, A. F. Smith, A. B. Patel, J. Feng, M. C. Murphy, S. A. Soper, J. Am. Chem. Soc., 2005, 127, 842.

35. Y. Dongzhi, C. Qifan, X. Shukun, J. Lumin., 2007, 126, 853.

36. X. G. Peng, J. Wickham, A. P. Alivisatos, J. Am. Chem. Soc., 1998, 120, 5343.

37. M. Green, P. O'Brien, Chem. Commun., 1999, 22, 2235.

38. Y. Xie, W. Z. Wang, Y. T. Qian, X. M. Liu, J. Solid State Chem., 1999, 147, 82.

39. J. J. Zhu, O. Palchik, S. Chen, A. Gedanken, *J. Phys. Chem. B* (2000), 104, 7344.

40. L. Liu, Q. Peng, Y. Li, Inorg. Chem., 2008, 47, 5022.

41. C. B. Murray, C. R. Kagan, M. G. Bawendi, Science, 1995, 270, 1335.

42. K. Tai, W. Lu, I. Umezu, A. Sugimura, Appl. Phys. Express,2010, 3, 035202.

43. H. C. Kim, H. G. Hong, C. Yoon, H. Choi, I. S. Ahn, D. C. Lee, Y. J. Kim, K. Lee, J. Colloid Interf. Sci., 2013, 393, 74.

44. D. Qi, M. Fischbein, M. Drndic, S. Selmic, Appl. Phys. Lett., 2005, 86, 093103.

45. O. O. Akinwunmi, G. O. Egharevba, E. O. B. Ajayi, J. Mod. Phys., 2014, 5, 257.

46. I Suarez, H Gordillo, R Abargues, S Albert, J. Mart, I. Pastor, Nanotechnology, 2011, 22, 435202 (8pp) doi:10.1088/0957-4484/22/43/435202.

47. R. N. Panda, A. Pradhan, Mater. Chem. Phys., 2002, 78, 313.

48. C. F. Bohren, D. R. Huffman, Absorption and Scattering of Light by Small Particles, John Wiley&Sons, New York, 1983, p.92.

49. H. C. van de Hulst, Light Scattering by Small Particles, Dover, Toronto, 1981, p.121.

50. M. Fukui, M. Otsu, Hikari Nanotechnology, Optical Nanotechnology, Ohmsha, Tokyo, 2003, p.85.

51. A. J. Cox, A. J. DeWeerd, J. Linden, Am. J. Phys., 2002, 70, 620.

52. J. C. Maxwell Garnett, Philos. Trans. R. Soc. A, 1904, 203, 385.

53. T. C. Choy, Effective Medium Theory - Principles and Applications, Oxford University Press, Oxford, 1999, p.1.

54. J. E. Sipe, R. W. Boyd, Nanocomposite Materials for Nonlinear Optics Based on Local Field Effects in Optical Properties of Nanostructured Random Media, V. M. Shalaev, ed., Springer, Berlin, 2002, p.1.

55. G. M. Kim, D. H. Lee, B. Hoffman, J. Kressler, G. Stoppelmann, Polymer, 2001, 42, 1095.

56. T. P. Mthethwa, M. J. Moloto, A. De Vries , K. P. Matabola, Mater. Res. Bull., 2011, 46, 569.

57. V. Radojevic, S. Nikolic, A. Golubovic, Crystal Growth from the melt, Monography, TMF, Belgrade, 2005.

58. D. T. Hurle, B. Cockayne, Handbook of Crystal Growth, vol. 2b, edited by D. T. Hurle, North-Holand, Amsterdam, 1994, 46.

59. Nucleation, edited by A. C. Zettlemoyer, Marcel Dekker. Inc. New York, 1969, 23.

60. M. C. Flemings, Solidification processing, McGraw-Hill, New York, 1974, 58.

61. F. Rosenberger, Fundamentals of Crystal Growth, Springer, Berlin, 1979, 86.

62. K. A. Jackson, Proceedings of the Third International Summer School on Crystal Growth, North- Holand Publ. Comp., 1979, 139.

63. K. A. Jackson, Liquid Metals and Solidification, ASM Clevland, 1958, 174.

64. A. Ohno, The Solidification of metals, Chijin Shokan Co.Ltd., Tokyo, 1976, 24.

65. A. Ohno, The Solidification of Metals, Chijin Shokan Co. Ltd., Tokyo, 1976, 36.

66. H. A. Palacio, M. Solari, H. Biloni, J. Cryst. Growth, 1985, 73, 369.

67. L. H. Ungar, M. J. Bennet, R. A. Brown, Phis. Rev. B, 1985, 31, 5923.

68. L. H. Ungar, R. A. Brown, Phis. Rev. B, 1985, 31, 5931.

69. B. Gao, S. Nakano, H. Harada, K. Kakimoto, Crystal Growth&Design, 2012, 12, 5708.

70. J. W. Ruter, B. Chalmers, Can. J. Phys., 1953, 31, 15.

71. W. A. Tiller, K. A. Jackson, J. W. Ruter, B. Chalmers, Acta Metall., 1953, 1, 428.

72. J. A. Burton, R. C. Prim, W. P. Slichter, J. Chem. Phys., 1953, 21, 1987.

73. J. A. Burton, E. D. Kolb, W. P. Slichter, J. D. Struthers, J. Chem. Phys., 1953, 21, 1991.

74. A. Valčić, S. Nikolić, T. Valčić, J. Serb. Chem. Soc., 1993, 58, 439.

75. A. Valčić, V. Radojević , S. Nikolić, J. Serb. Chem.Soc., 1995, 60, 35.

76. J. B. Mullin, in Crystal Growth and Characterization, eds. R. Ueda and J.B. Mullin, North-Holland, Amsterdam, 1975, p. 75.

77. H. C. Gatos, in Crystal Growth: A Tutorial Approach, eds. by W. Bardsley and D. T. J. Hurle, North- Holland, Amsterdam, 1979, p.1.

78. D. T. J. Hurle, in Crystal Growth: A Tutorial Approach, eds. by W. Bardsley and D. T. J. Hurle, North-Holland, Amsterdam, 1979, p. 91.

79. K-W. Benz, E. Bauser, in Crystals: Growth, Properties and applications, vol. 3, III-V

Semiconductors, Springer-Verlag, Berlin, 1980, p. 1.

80. J. B. Mullin, in Crystal Growth of Electronic Materials, eds. by E. Kaldis, Elsevier Science, Amsterdam, 1985, p. 269.

81. R. Fornari, Mater. Sci. Engineer. B, 1991, 9, 9.

82. M. Isshiki, in Widegap II-VZ Compounds for Opto-electronic Applications, ed. H.E. Ruda, Chapman&Hall, 1992, p. 3.

83. Handbook of Crystal Growth, vol. 2, Bulk Crystal Growth, ed. D. T. J. Hurle, Elsevier Sci. Amsterdam, 1996.

84. G. Miiller, Mater. Sci. Forum,1998, 276-277, 87.

85. Book on Crystal Growth Technology, ed. H.J. Scheel, John Wiley&Sons, New York, 2004.

86. J. B. Mullin, J. Appl. Phys., 2004, 264, 578.

87. P. W. Bridgman, Certain physical properties of single crystals of tungsten, antimony, bismuth, tellurium, cadmium, zinc, and tin, Proceedings of the American Academy of Arts and Sciences, 1925, 60, 305.

88. D. C. Stockbarger, The production of large single crystals of lithium fluoride, Review of Science Instruments, 1936, 7, 133.

89. D. C. Stockbarger, The production of large artificial fluorite crystals, Discussions of the Faraday Society, 1949, 5, 294.

90. W.D. Lawson, S. Nielsen, Preparation of Single Crystals, Butterworths Scientific Publications, London, 1958.

91. D. J. Hurle, Proceedings of the Third International Summer School on Crystal Growth, North- Holand Publ. Comp., 1979, 3.

92. J. C. Brice, Crystal growth processess, John Wiley&Sons, New York, 1986.

93. G. Dhanaraj, K. Byrappa, V. Prasad, M. Dudley, Handbook of crystal growth, Springer-Verlag, Berlin Haidelberg, 2010.

94. J. Czochralski, Z. Physik. Chem., 1918, 92, 219.

95. J. Czochralski, Modern Metallkunde in Theorie und Praxis, Springer,Berlin, 1924

96. J. J. Favier, J. Cryst. Growth, 1990, 99, 18.

97. W. A. Gault, E. M. Mornberg, J. E. Clmans, J. Cryst. Growth, 1986, 74, 491.

98. P. W. Bridgman, Proc. Am. Art.Sci., 1925, 60, 303.

99. G. Li, X. Zhang, H. Hua, W. Jie, J. Electronic Materials, 2005, 34, 1215.

100. E. Scheil, Z. Metallk, 1942, 34, 70.

101. R. Y. Tsai, S. C. Shiau, D. Lin, F. C. Ho, M. Y. Hua, Appl. Opt., 38, 1999, 5452.

102. H. Wang, R. Liu, K. Chen, X. Shi, Z. Xu, Thin Solid Films, 519, 2011, 6438.

103. S. Fujihara, Y. Kadota, T. J. Kimura, Sol-Gel Sci. Technol., 2002, 24, 147.

104. A.W. Hull, Phys. Rev., 1921, 17, 42.

105. M. Y. Sharonov, Z. I. Zhmurova, E. A. Krivandina, A. A. Bystrova, I. I. Buchinskaya, B. P. Sobolev, Opt. Commun., 1996, 124, 558.

106. V. Petit, J. L. Doualan, P. Camy, V. Menard, R. Moncorge, Appl. Phys. B, 2004, 78, 681.

107. A. Lucca, G. Debourg, M. Jacquemet, F. Druon, F. Balembois, P. Georges, P. Camy, J. L. Doualn, R. Moncorge, Opt. Lett., 2004, 29, 2767.

108. J. W. Stouwdam, M. Raudsepp, F. C. J. M. van Veggel, Langmuir, 2005, 21, 7003.

109. X. Michalet, F. Pinaud, L. Bentolila, J. Tsay, S. Doose, J. Li, G. Sundaresan, A. Wu, S. Gambhir, S. Weiss, Science, 2005, 307, 538.

110. S. Sivakumar, C. Frank, J. M. van Veggel, P. S. May, J. Am. Chem. Soc., 2007, 129, 620.

111. X. Xu, L. Ling, R. Wang, J. O. Burgess, Dent. Mater., 2006, 22, 1014.

112. P. Samuel, H. Ishizawa, Y. Ezura, K. I. Ueda, S. Moorthy Babu, Opt. Mater., 2011, 33, 735.

113. A. Molchanova, J. Friedricha, G. Wehrhan, G. Müller, J. Cryst. Growth, 2005, 273, 629.

114. M. Paraschiva, I. Nicoara, M. Stef, O. M. Bunoiu, Acta Phys. Pol. A, 2010, 117, 466.

115. N. Senguttuvan, M. Aoshima, K. Sumiya, H. Ishibashi, J. Cryst. Growth, 2005, 280, 462.

116. A. Ikesue, Y. L. Aung, Nat. Photonics, 2008, 2, 721.

117. S. E. Hatch, W. F. Parsons, R. J. Weagley, Appl. Phys. Lett., 1964, 5, 153.

118. P. A. Popov, K. V. Dykel'skii, I. A. Mironov, A. N. Smirnov, P. L. Smolyanskii, P. P. Fedorov, V. V. Osiko, T. T. Basiev, Doklady Physics, 2007, 52, 7.

119. J. Kotz, P. Treichel, J. Townsend, Enhanced Edition, Kluwer Academic/Plenum

Publishers, New York, vol. 3, 2002.

120. K. C. Cheng, H. L. W. Chan, C. L. Choy, Q. Yin, H. Luo, Z. Yin, IEEE Transactions on Ultrasonics, Ferroelectrics, and Frequency Control, 2003, 50, 1177.

121. E. B. Gibelli, J. Kai, E. E. S. Teotonio, O. L. Malta, M. C. F. C. Felinto, J. Photochem. Photobiology A: Chemistry, 2013, 251, 154.

122. M. Rosemal, H. M. Harisa, S. Kathiresan, S. Mohan, Der Pharma Chemica, 2010, 2, 316.

123. A. Chapiro, Radiation Chemistry of Polymeric Systems, John Wiley&Sons, New York, 1962.

124. R. G. Jagger, J. Prosthet. Dent., 1996, 76, 573.

125. L. Woo, M. T. K. Ling, S.Y. Ding, S. P. Westphal, L. Woo, M. T. K. Ling, S. Y. Ding, S. P. Westphal, Thermochim. Acta, 1998, 324, 179.

126. T. N. Blanton, Debasis Majumdar, Powder Diffraction, 2012, 27, 104.

127. C. He, M. Gu, Scr. Mater., 2006, 55, 481.

128. M. S. Al-Haik, H. Garmestani, D. S. Li, M. Y. Hussaini, S. S. Sablin, R. Tannenbaum, K. Dahmen, J. Polymer Science: Part B: Polymer Physics, 2004, 42, 1586.

129. M. R. VanLandingham, J. S. Villarrubia, W. F. Guthrie, G. F. Meyers, Nanoindentation of Polymers: An Overview, Macromolecules Symposium, 2001, 167, 15.

130. A. C. Fischer-Cripps, Nanoindentation, Mechanical Engineering Series, ed. F.F. Ling, New York, Springer-Verlag, 2002, p.194.

131. W. C. Oliver, G. M. Pharr, J. Mater. Res., 1992, 7, 1564.

132. Materials Evaluation and Engineering, Inc., Handbook of Analytical Methods for Materials, http://www.mee-inc.com/ham.html.

133. H. A. Szymanski, IR: Theory and Practice of Infrared Spectroscopy, New York, Plenum Press, 1964, p.375.

134. J. Koenig, Adv. Mater., 2002;14, 457.

135. T. Ribar, R. Bhargava, J. L. Koenig, Macromolecules, 2000, 33, 8842.

136. T. Ribar, J. L. Koenig, Macromolecules, 2001, 34, 8340.

137. B. A. Miller-Chou, J. L. Koenig, Macromolecules, 2002, 35, 440.

138. J. Gonzales-Benito, J. L. Koenig, Macromolecules, 2002, 35, 7361.

139. M. R. Van Landingham, J. Res. Natl. Inst. Stand. Technol., 2003, 108, 249.

140. U. Ramamurty, Jae-il Jang, Cryst. Eng. Comm., 2014, 16, 12.

141. B. Bhushan, V.N. Koinkar, Appt. Phys. Lett., 1994, 64, 1653.

142. M. F. Doerner, W.D. Nix, J. Mater. Res., 1986, 1, 601.143.

143. D. Dragoman, M. Dragoman, Optical Characterization of Solids, Springer-Verlag, Berlin, 2002.

144. J. Goldstein, D. E. Newbury, D. C. Joy, C. E. Lyman, P. Echlin, E. Lifshin, L. Sawyer, J. R. Michael, Scanning Electron Microscopy and X-ray Microanalysis, Third Edition, Springer, 2003.

145. C. Moulin, I. Laszak, V. Moulin, C.Tondre, Applied Spectroscopy, 1998, 52, 528.

146. M. S. Rabasovic, D. Sevic, M. Terzic, B. P. Marinkovic, Nucl. Instrum. Methods Phys. Res. B, 2012, 279, 16.

147. H. Yanagi, T. Nawata, Y. Inui, Y. Hatanaka, E. Nishijima, T. Fukuda, Proc. SPIE 5377, Optical Microlithography XVII, 1886 (May 28, 2004); doi:10.1117/12.556614.

148. N. Senguttuvan, M. Aoshima, K. Sumiya, H. Ishibashi, J. Crys. Growth, 2005, 280, 462.

149. J. Xu, M. Shi, B. Lu, X. Li, A. Wu, J. Crys. Growth, 2006, 292, 391.

150. G. Scholz, I. Dörfel, D. Heidemann, M. Feist, R. Stösser, J. Solid State Chem., 2006, 179, 1119.

151. I. V. Stepanov, P. P. Feofilov, Artificial fluorite. In Rost kristalov (vol. I), Moscow, Russia: Akademia Nauk SSSR. (in Russian), 1957, p. 229.

152. G. V. Molev, V. E. Bozherolnog, J. Crys. Growth, 1973, 19, 117.

153. K. Recker, R. Leckebusch, J. Crys. Growth, 1971, 9, 274.

154. K. O. Čajko, D. L. Sekulić, S. Lukić-Petrović, M. V. Šiljegović, D. M. Petrović, J. Mater. Sci.- Mater. El., 2017, 28, 120.

155. L. Gerward, J. S. Olsen, S. Steenstrup, M. Malinowski, S. Åsbrink, A. Waskowska, J. Appl. Crystallogr., 1992, 25, 578.

156. B.-C. Hong, K. Kawano, J. Alloys Compd.,2006, 408-412, 838.

157. N. D. Alharbi, J. Nanomaterials, volume 2015, Article ID 136957, 8 pages,

http://dx.doi.org/10.1155/2015/136957.

158. S. Biswas, S. Kar, S. Chaudhuri, J. Cryst. Growth, 2007, 299, 94.

159. G. Scholz, I. Dörfel, D. Heidemann, M. Feist, R. Stösser, J. Solid State Chem., 2006, 179, 1119.

160. Y. Wang, L. A. Zhang, S. Shang, Z. Kui. Liu, L.Q. Chen, Phys. Rev. B, 2013, 88, 024304.

161. K. Schmalzl, D. Strauch, H. Schober, Phys. Rev. B, 2003, 68, 144301.

162. R. K. Chang, B. Lacina, P. S. Pershan, Phys. Rev. Lett., 1966, 17, 755.

163. J. R. Ferraro, H. Horan, A. Quattrochi, J. Chem. Phys., 1971, 55, 664.

164. D. G. Mead, G. R. Wilkison, J. Phys. C, 1977, 10, 1063.

165. D. J. Oostra, H. W. den Hartog, Phys. Rev. B, 1984, 29, 2423.

167. P. C. Ricci, A. Casu, G. de Giudici, P. Scardi, A. Anedda, Chem. Phys. Let., 2007, 444, 145.

168. A. A. Kaminskii, S. N. Bagayev, H. J. Eichler, H. Rhee, K. Ueda, K. Takaichi, K. Oka, H. Shibata, Y. Hatanaka, Y. Matsumoto, Laser Phys. Lett., 2006, 8, 385.

169. L. Su, J. Xu, W. Yang, X. Jiang, Y. Dong, Chinese Optics Letters, 2005, 3, 219.

170. J. P. Russell, Proceedings of the Physical Society, 1965, 85, 194.

171. J. Song, G. Zhi, Y. Zhang, B. Mei, Nano-Micro Lett., 2011, 3, 73.

172. L. Zhou, D. Chen, W. Luo, Y. Wang, Y. Yu, F. Liu, Mater. Lett., 2007, 61, 3988.

173. K. Tahvildari, M. Esmaeili Pour, Sh. Ghammamy, H. Nabipour, Int. J. Nano Dim., 2012, 2, 269.

174. C. Pandurangappa, B. N. Lakshminarasappa, B. M. Nagabhushana, J. Alloys Compd., 2010, 489, 592.

175. J. P. Russell, J. Phys. France, 1965, 26, 620.

176. F. Gervais, Infrared and Millimeter Waves, 8, Academic, New York, 1983, pp. 279.

177. F. Kadlec, P. Simon, N. Raimboux, J. Phy. Chem. Solids, 1999, 60, 861.

178. S. Ganesan, E. Burstein, Journal de Physique, 1965, 26, 645.

179. W. Kaiser, W. G. Spitzer, R. H. Kaiser, L. E. Howarth, Phys. Rev., 11962, 27, 1950.

180. V. S. Singh, C. P. Joshi, S. V. Moharil, P. L. Muthalc, S.M. Dhopte, Luminescence, 2015, 30, 1101.

181. N. Salah, N. D. Alharbi, S. S. Habib, S. P. Lochab, J. Nanomaterials, 2015, vol. 16, 136402, http://dx.doi.org/10.1155/2015/136402.

182. Fairfield Crystal Technology, http://www.fairfieldcrystal.com.

183. A. K. Jonscher, Nature, 1977, 267, 673.

184. R. Ben Said, B. Louati, K. Guidara, Ionics, "AC conduction mechanism of the zinc potassium diphosphate," 2017, in press, doi 10.1007/s11581-017-2070-5

185. W. Chen, W. Zhu, O. K. Tan, X. F. Chen, J. Appl. Phys., 2010, 108, 034101-034101-7.

186. I. Jlassi, N. Sdiri, H. Elhouichet, M. Ferid, J. Alloys Compd., 2015, 645, 125.

187. M. Mirsaneh, E. Furman, J. V. Ryan, M. T. Lanagan, C. G. Pantano, Appl. Phys. Lett., 2010, 96, 112907.

188. J. Wanga, C. C. Wanga, Q. J. Li, Y. Yu, J. Zhang, J. Zheng, C. Cheng, Y. D. Li, H. Wang, S. G. Huang, Materials Science and Engineering B, 2014, 188, 31.

189. I. S. Elashmawi, N. A. Hakeem, Polym. Eng. Sci., 2008, 48, 895.

190. F. Goldibi, G. Asghari, Res. J. Biol. Sci., 2009, 4, 244.

191. H. A Willis, V. J. I. Zichy, P. J. Hendra, Polymer, 1969, 10, 737.

192. Y. Ren, A. Matsushita, K. Matsukawa, H. Inoue, Y. Minami, I. Noda, Y. Ozakia, Vibrational Spectroscopy, 2000, 23, 207.

193. G. Socrates, Infrared and Raman Characteristic Group Frequencies, New York: Wiley (2001).

194. A. Acharya, R. Mishra, G. S. Roy, Lat. Am. J. Phys., 2010, 4, 603.

195. F. J. Baltá-Calleja, A. Flores, F. Ania, in Mechanical properties of polymers based on nanostructure and morphology, G. H. Michler, F. J. Baltá-Calleja, Eds., London:Taylor and Francis, 2005.

196. A.Flores, F. Ania, F. J. Baltá-Calleja, Polymer, 2009, 50, 729.

197. S. S. Musbah, V. Radojević, N. Borna, D. Stojanović, M. Dramićanin, A. Marinković, R. Aleksić, J. Serb. Chem. Soc., 2011, 76, 1153.

198. N. A. Hamizi, M. R. Johan, Mater. Chem. Phys., 2010, 124, 395.

199. J. Yao, G. Zhao, D. Wang, G. Han, Mater. Lett., 2005, 59, 3652.

200. H. El-Swie, I. Radovic, D. B. Stojanovic, D. M. Sevic, M. S. Rabasovic, P. Uskokovic, V. Radojevic, J. Optoelectr. Adv. Mat., 2017, 19, 228.

Прилог 1.

Изјава о ауторству

Потписани-а ___Hana Ibrahim Elswie_____

број индекса _____4062/2012_____

Изјављујем

да је докторска дисертација под насловом

Синтеза и карактеризација оптички активних композита са полимерном матрицом на бази монокристала

Synthesis and characterization of optical polymer composites based on single crystals

- резултат сопственог истраживачког рада,
- да предложена дисертација у целини ни у деловима није била предложена за добијање било које дипломе према студијским програмима других високошколских установа,
- да су резултати коректно наведени и
- да нисам кршио/ла ауторска права и користио интелектуалну својину других лица.

Потпис докторанда

У Београду, ___13.02.2017._____

Прилог 2.

Изјава о истоветности штампане и електронске верзије докторског рада

Име и презиме аутора _____ Hana Ibrahim Elswie _____

Број индекса _____ 4069/2012 _____

Студијски програм _____ Инжењерство Материјала _____

Наслов рада _ Синтеза и карактеризација оптички активних композита са полимерном матрицом на бази монокристала

Synthesis and characterization of optical polymer composites based on single crystals

Ментори _____ Радојевић Весна _____

_____ Зорица Лазаревић _____

Потписани/а _____

_____

Изјављујем да је штампана верзија мог докторског рада истоветна електронској верзији коју сам предао/ла за објављивање на порталу **Дигиталног репозиторијума Универзитета у Београду.**

Дозвољавам да се објаве моји лични подаци везани за добијање академског звања доктора наука, као што су име и презиме, година и место рођења и датум одбране рада.

Ови лични подаци могу се објавити на мрежним страницама дигиталне библиотеке, у електронском каталогу и у публикацијама Универзитета у Београду.

Потпис докторанда

У Београду, ___13. 02. 2017.____

Прилог 3.

Изјава о коришћењу

Овлашћујем Универзитетску библиотеку „Светозар Марковић" да у Дигитални репозиторијум Универзитета у Београду унесе моју докторску дисертацију под насловом:

Синтеза и карактеризација оптички активних композита са полимерном матрицом на бази монокристала

Synthesis and characterization of optical polymer composites based on single crystals
која је моје ауторско дело.

Дисертацију са свим прилозима предао/ла сам у електронском формату погодном за трајно архивирање.

Моју докторску дисертацију похрањену у Дигитални репозиторијум Универзитета у Београду могу да користе сви који поштују одредбе садржане у одабраном типу лиценце Креативне заједнице (Creative Commons) за коју сам се одлучио/ла.

1. Ауторство

2. Ауторство - некомерцијално

3. Ауторство – некомерцијално – без прераде

4. Ауторство – некомерцијално – делити под истим условима

5. Ауторство – без прераде

6. Ауторство – делити под истим условима

(Молимо да заокружите само једну од шест понуђених лиценци, кратак опис лиценци дат је на полеђини листа).

Потпис докторанда

У Београду, ____13.02.2017._____

1. Ауторство - Дозвољавате умножавање, дистрибуцију и јавно саопштавање дела, и прераде, ако се наведе име аутора на начин одређен од стране аутора или даваоца лиценце, чак и у комерцијалне сврхе. Ово је најслободнија од свих лиценци.

2. Ауторство – некомерцијално. Дозвољавате умножавање, дистрибуцију и јавно саопштавање дела, и прераде, ако се наведе име аутора на начин одређен од стране аутора или даваоца лиценце. Ова лиценца не дозвољава комерцијалну употребу дела.

3. Ауторство - некомерцијално – без прераде. Дозвољавате умножавање, дистрибуцију и јавно саопштавање дела, без промена, преобликовања или употребе дела у свом делу, ако се наведе име аутора на начин одређен од стране аутора или даваоца лиценце. Ова лиценца не дозвољава комерцијалну употребу дела. У односу на све остале лиценце, овом лиценцом се ограничава највећи обим права коришћења дела.

4. Ауторство - некомерцијално – делити под истим условима. Дозвољавате умножавање, дистрибуцију и јавно саопштавање дела, и прераде, ако се наведе име аутора на начин одређен од стране аутора или даваоца лиценце и ако се прерада дистрибуира под истом или сличном лиценцом. Ова лиценца не дозвољава комерцијалну употребу дела и прерада.

5. Ауторство – без прераде. Дозвољавате умножавање, дистрибуцију и јавно саопштавање дела, без промена, преобликовања или употребе дела у свом делу, ако се наведе име аутора на начин одређен од стране аутора или даваоца лиценце. Ова лиценца дозвољава комерцијалну употребу дела.

6. Ауторство - делити под истим условима. Дозвољавате умножавање, дистрибуцију и јавно саопштавање дела, и прераде, ако се наведе име аутора на начин одређен од стране аутора или даваоца лиценце и ако се прерада дистрибуира под истом или сличном лиценцом. Ова лиценца дозвољава комерцијалну употребу дела и прерада. Слична је софтверским лиценцама, односно лиценцама отвореног кода.

Biography

Hana Ibrahim El Swie was born on 16. 01. 1985. in Tripoli, Libya. She finished high school in the school Shohada Algomoa in Tripoli in 2001. She graduated in 2005. at the University of Tripoli, Faculty of Science, Department of Physics.

Master study ended 2011. at the University of Belgrade, Faculty of Technology and Metallurgy, Materials Engineering profile.

Doctoral Studies started in 2012 at the University of Belgrade, Faculty of Technology and Metallurgy, Materials Engineering profile.

She has worked since 2005. as an assistant at the University of Tripoli, Faculty of Science, Department of Physics.

Biografija

Hana Ibrahim El Swie rođena je 16. 01. 1985. u Tripoliju, Libija. Srednju školu je završila u školi Shohada Algomoa u Tripoliju 2001. godine. Diplomirala je 2005. na Univerzitetu u Tripoliju, Fakultet prirodnih nauka, Departman za fiziku.

Od 2005. godine zaposlena je kao asistent na Univerzitetu u Tripoliju, Fakultet prirodnih nauka, Departman za fiziku.

Master studije je završila 2011. na Univerzitetu u Beogradu, Tehnološko-metalurški fakultet, profil Inženjerstvo materijala. Doktorske studije upisala je 2012. godine na Univerzitetu u Beogradu, Tehnološko-metalurški fakultet, profil Inženjerstvo materijala.